Université catholique de Louvain
Ecole Polytechnique de Louvain
ICTEAM Institute

Analysis and Design of Wideband Antenna Arrays for Near-Field Imaging

Khaldoun Alkhalifeh

Thesis submitted in partial fulfilment of the requirements for the Ph.D. Degree in Applied Sciences

Thesis Committee

Advisor:	Christophe CRAEYE, UCL, Belgium
Jury:	Piotr SOBIESKI, UCL, Belgium
	Sébastien LAMBOT, UCL, Belgium
	Alexander YAROVOY, TU Delft, the Netherlands
	Enrica MARTINI, University of Siena, Italy
President:	Jean-Pierre Raskin, UCL, Belgium

Louvain-la-Neuve, Belgium.

To my parents, brother, sisters, Nour and wife
for their endless love

Abstract

Ultra-Wide Band (UWB) radar systems are widely used for different applications such as imaging systems and Ground Penetrating Radar (GPR). To realize such UWB antennas, different characteristics in terms of geometry and materials need to be used. Three-dimensional metallic antennas attracted great attention for systems which require the miniaturization of antennas. The objective of this thesis is to add insights into the design and analysis of 3-D antennas and arrays for ground-penetrating, imaging and wireless communication applications. This is done by contributing to the development of fast numerical methods able to analyze large antenna arrays and, in particular, by adding the contribution of the ground on antennas placed close to it. The thesis intends to explain the design of 3-D multiband antennas and circular arrays of UWB antennas, based on both numerical simulations and validation with measurement.

In the analysis of antenna arrays, the mutual coupling phenomenon has to be seriously taken into consideration. The radiation patterns of a single element in an array differs from that of the same element when it is isolated, due to the mutual coupling contribution. One proposed solution to mitigate the mutual coupling effect is to design the array in a connected, possibly circular, shape. This solution avoids the current distributions flowing along the edges of each individual antenna, and allows them to flow through every consecutive element. The radiation patterns of all elements in the circular array will be the same, except for a rotation with a certain phase shift, which allows us to use the Array Scanning Method (ASM) to analyze large arrays. The results for design and fabrication of various single antenna prototypes are presented with good correspondence between simulation and measurement. The validation of applying the ASM on a circular array of Vivaldi antennas is presented through a comparison of the brute-force MoM system of equation with the ASM solution. The fabrication of a novel circular array of Vivaldi elements

is also revealed with very good agreement between simulation and measurement. We named the prototype the ”Wheel-of-Time (WoT)”. The WoT prototype will be used for locating and imaging targets in the area of radiation exposure. An initial near-field image of a metallic tube in the area of radiation exposure is depicted, and the target is localized. The WoT prototype with two different metallic cylinders have been simulated using the ASM applied to the Method of Moments. The resolution between metallic cylinders is investigated experimentally and numerically. Preliminary results are also provided regarding reconstruction of a dielectric cylinder positioned in the area of radiation exposure.

An important component in the development of water leak detection is to design a 3-D UWB antenna, i.e., to detect underground leaking pipes. Low-frequency antenna design is challenging due to the expected large dimensions of the radiator. The bandwidth of interest is set from 0.25 GHz to 2.5 GHz. A UWB Vivaldi antenna design has been proposed with $60 \times 41 \times 1.5$ cm dimensions. We took as an objective to minimize the antenna weight by introducing holes in specific positions related to the current distributions. The proposed antenna was fabricated and measured at UCL. The comparison between measurements and simulations is very satisfactory, with a bandwidth from 250 MHz up to 2 GHz under a -10 dB criterion in terms of reflection coefficient. Preliminarily tests have been carried out to examine the effect of the nearby ground on the measurement. The trials have first been carried out using the CST commercial software with two different permittivities, and it shows the effect of the ground appears at low frequencies in terms of reflection coefficient.

For the GPR application, the antenna is very close to the medium, such as the lossy ground, which will strongly modify the antenna input impedance and radiated near-fields. This modification can be added on antennas by the explicit use (or pre-computation) of the layered-medium Green's function. The newly proposed method gives an alternative efficient solution by introducing the effect of the ground via a reflection coefficient defined in a 2-D spatial-spectrum domain. This allows the evaluation of a matrix that exclusively accounts for the contribution of the ground to the MoM impedance matrix of the antenna. This is then added to the free-space MoM matrix, which can be computed once and for all. Moreover the extra matrix including the ground contribution can make use of precomputed radiation patterns of every basis function on the antenna, which are independent from the ground parameters. We name the method Fast Ground Contribution Matrix (FGCM).

The number of samples in (complex) spectral domain is dramatically reduced by explicitly compensating truncation with aliasing errors in the spectral integration. The FGCM method is able to simulate the antenna response for arbitrary soil parameters (permittivity, conductivity, permeability, etc.), assuming multi-layered media. To demonstrate the accuracy and efficiency of the proposed method, numerical results for a 3-D metallic Vivaldi and typical dipole antennas are presented. A good agreement among the exact Method of Moments (MoM) solutions, the simulation results, and measured data is observed over an ultra-wide bandwidth.

Finally, we gathered the FGCM method with Macro Basis Functions (MBFs) and the Contour-Fast Fourier Transform (C-FFT) methods to analyze large planar antenna arrays placed vertically above a layered substrate. The FGCM method was successfully applied to a regular array of dipole antennas, taking the benefit of accelerated computations of interactions between MBFs using the C-FFT method.

Acknowledgments

First and foremost, I am grateful to my advisor Christophe Craeye. This thesis would not have been possible without his constant supervision and motivation. His unequivocal technical expertise, teaching skills, and the unique ability to motivate proved to be immense help to me, and encouraging ideas place him at the apex of the scientific research community.

I would also like to extend my gratitude to the Dr. Remi Sarkis for his patience and guidance throughout this entire process. His deep technical knowledge was very useful for me and nurtured my ideas. I would like to thank Prof. Sebastien Lambot for his wonderful supervision during the thesis. His vast acknowledgment, especially in GPR domain, helps me expanding my understanding to the problems, it was an immense pleasure to work with him. I would like to thank Prof. Piotre Sobieski for his kind reception and guidance at my first Master days at UCL. I am deeply thankful to the members of my jury, Prof. Alexander Yarovoy and Dr. Enrica Martini for their insightful comments and suggestions. I would also like to thank Sumit Karki for his nice Matlab programming and AutoCAD file transfer, special thanks for the nice moments and trips. I am also thankful to Dr. Donia Oueslati for her discussions and ideas through various subjects, especially S-parameter conversion. Many thanks to Dr. Shambhu Nath JHA for his great collaboration and recommendations in different subjects, especially Matlab coding of antennas in the present of dielectric and applying the C-FFT method. My sincere thanks to Dr. Ha Bui Van, Maxime Drouguet, David Spot and Souley Djadjandi for anechoic chamber measurements collaboration. I would like to thank my fellow lab mates in Louvain-la-Neuve for the stimulating discussions and the nice moments we had, especially: Dr. Christopher Raucy, Inès Adouani, Simon Hubert, Denis Tihon, Quentin Gueuning, Husnain Ali Kayani, Thomas Pairon; and all others.

At last but not the least, the funding sources from the university of Damascus (Syria), and Région Wallonne through SENSPORT, OPTIGRID and B-WARE projects are greatly acknowledged.

Finally, my parents have been a source of encouragement and support throughout my life. I like to thank my parents, brother and sisters, whose unlimited love and support has made this effort possible, especially thank my mother for her unconditional love and strength. I would like to specially thank my wife Aya, her tolerance of my occasional vulgar moods is a testament in itself of her unyielding devotion and love.

Contents

List of Figures

List of Tables

List of symbols and acronyms

Acronyms

ASM — Array Scanning method (p. 3)

AUT — Antenna Under Test (p. 47)

BFs — Basis Functions (p. 81)

C-FFT — Contour-Fast Fourier Transform (p. 5)

DGLM — Dyadic Green's function for Layered Media (p. 78)

DLR — Dynamic Line Rating (p. 117)

FCC — Federal Communications Commission (p. 21)

FDTD — Finite Difference Time Domain (p. 23)

FEM — Finite Element Method (p. 23)

FGCM — Fast Ground Contribution Matrix (p. 4)

GPR — Ground Penetrating Radars (p. 3)

MBFs — Macro Basis Functions (p. 5)

MoM — Method of Moments (p. 31)

PEC — Perfect Electrical Conductor (p. 26)

SDP — Steepest-descent Path (p. 78)

SIE — Surface Integral Equation (p. 78)

TFs — Testing Functions (p. 81)

TUT — Target Under Test (p. 45)

UWB — Ultra-Wide Band (p. 3)

VNA — Vector Network Analyzer (p. 41)

VSIE — Volume-Surface Integral Equation (p. 78)

WoT — Wheel-of-Time (p. 4)

Introduction and Motivation

1

The UWB technique has attracted a great interest for communication systems, Ground Penetrating Radars and Medical Imaging. Antenna arrays for UWB applications need to exhibit wide bandwidths for input impedance and radiation patterns. Recent research in medical applications has shown interesting results to detect breast cancer by UWB imaging technology [1]. The near-field radiation can be used efficiently to illuminate breast tumors. Detection of hidden low-visible targets, as is the case in robotic or security sensors, needs UWB radars which could provide high range resolution [2]. In this thesis, various UWB antenna designs have been realized in the form of prototypes devoted to different applications. We attempt to use simple and efficient techniques in fabrication to obtain robust UWB radar systems. Fast numerical methods have been developed to analyze large circular antennas arrays, taking into account the mutual coupling between elements. Additionally, a novel fast method to add the contribution of the ground on 3-D metal antennas has been developed and extensively tested.

1.1 Background

The Federal Communications Commission (FCC) allocates the 3.1-10.6 GHz spectrum for UWB radio applications [3], which presents a myriad of exciting opportunities and challenges in the field of communications; and entails important efforts in terms of antenna design. Some applications require operating bandwidths up to greater than 100% of the center frequency, where low and high frequencies are needed for essentially different purposes. Security applications also become a high priority in society due to terrorist threats in the last few years. Radar imaging has been used for airport terminal security [4]. For these applications, important efforts have focused on high resolution and on developing fast methods to provide images in real time. In [5], a fast three-dimensional imaging method, the revised range point migration (RRPM), is proposed to image a mannequin with a handgun. The proposed method is able to image a target in unknown motion, and it can produce more than 100 images within the processing time required for the F-K (frequency-wavenumber) migration method. In [6], a design approach is proposed for high resolution near-field imaging for a MIMO array that minimizes the number of antenna elements to achieve the required imaging performance. The 2-D MIMO array has an aperture size of 45 mm and exhibits consistent UWB characteristics in the frequency band from 2.7 to 26 GHz. The suggested topology achieves 1 cm cross-range resolution (-3 dB level) and -25 dB sidelobe level with 12 antenna elements, in contrast to the classical arrays 2 cm cross-range resolution and -20 dB sidelobe level.

In general, narrow-band antennas and propagation are studied in the frequency domain. In the UWB case, it is also desirable to look at the frequency-dependent characteristics of the antennas. From an other point of view, UWB systems often rely on an impulse-based aspect, such that the time-domain effects should be considered. The time-domain responses of course are inferred from frequency-domain characteristics through a Fourier transform [7]. In general, over the whole bandwidth, it is recommended to get antenna radiation patterns, gains and impedance matching as stable as possible. Based on the application, directional or omni-directional radiation properties are required. For mobile and hand-held systems, omni-directional patterns are used. When high gain is needed for radar systems, directional radiation characteristics are preferred. Due to its great performance in the UWB range, the Vivaldi antenna [8] is chosen in this thesis as the main element in the design of 3-D UWB systems. Theoretically, the Vivaldi antenna should radiate electromagnetic waves at a given wavelength when the width of the tapered slot is nearly equal to half the wavelength. The waves appear as bound in the region where the space between conductors is small compared to the free-space wavelength, and begin to damp when going away from the antenna. In practice, the upper operating frequency is limited by the transition from the feeding transmission line to the slot line of the antenna. Also, the physical dimensions of the antenna which rely on the characteristic length play a key role for bandwidth limitation.

Nowadays, phased arrays are used in various applications for the versatility of their radiation pattern. Antenna arrays could be formed in 1-D configuration, which needs the help of mechanical scanning in the direction orthogonal to the array to obtain images, or they are 2-D with the possibility of fully electronic scanning. Circular antenna arrays have several advantages over other types of array antenna configurations; such as the capability of all-azimuth scan, invariant beam pattern in every ϕ-cut, and flexibility in array pattern synthesis. As long as the inter-element spacing almost remains smaller than half of the wavelength, a uniform arrangement of elements can be envisaged [9]. Recent studies showed the use of directional antennas improves the accuracy of radio tomographic imaging (RTI) [10]. Directional antennas can be formed by choosing combing the array elements. RTI is used to estimate the locations of people and objects within the area of interest. All these new antenna configurations need to be efficiently analyzed, in particular to determine the radiation pattern of each element in presence of the other elements. Different computational electromagnetic algorithms have been developed to find the solution for a wide range of electromagnetic problems, each with its own benefits and limitations. The Finite Difference Time Domain method (FDTD) [11]-[13], and the Finite Element Method (FEM) [14]-[15] can be very useful in the case of complex media such as non-uniform materials. These methods use volume meshing, where it is necessary to discretize the whole volume in addition to absorbing boundary conditions. So the number of unknowns increases with the cube of the linear meshing density. The Method-of-Moments (MoM) [16] technique only uses a surface mesh without requiring absorbing boundary conditions, and the number of unknowns increases only with the square of the linear meshing density. In electromagnetic problems, the number of unknowns increases with the number of elements in the array, which costs more complexity and memory in the system. The Array Scanning Method (ASM) technique allows the efficient computation of induced currents in periodic structures. For circularly periodic arrays (or "discrete bodies of revolution") important time saving can be achieved, when all elements are excited with an inter-element phase shift corresponding to an integer fraction of 2π. Then, for excitation at a single element, the ASM can be used. In the case of excitation at one port in an array of N elements, while the remaining elements are passively terminated, the currents can be obtained from infinite-array simulations [17], with the help of the MoM. Ground Penetrating Radars (GPR) are regularly used to investigate layered media [18]-[20]. To include the effect of the very nearby ground, the Green's function for layered media needs to be used [21], which slows down the simulation process. Also, antenna simulations are often carried out with a wide range of ground types (permittivity, number of layers, layer thicknesses etc.). This requires the same antenna to be simulated many times with a large number of prospective soil properties. The previous challenges lead us to a novel method which we called the Fast Ground Coupling Matrix (FGCM). The extra matrix including the ground contribution can make use of precomputed radiation patterns of every basis function on the antenna, which are independent from the ground parameters.

Many types of single-feed wire antennas were suggested to operate for GSM wireless applications. A 3-D multi-branch monopole antenna for cellular hand-set and portable equipments is proposed in [22]. The multi-wideband antenna covers most GSM family standards. Three dimensional antennas attracted great attention for systems which require the miniaturization of antennas. H. Thal [23] has demonstrated that the lowest quality factor Q is achieved by a spherical volume supporting the TM_{10} mode. 3-D electrically small dome antennas originally appeared in [24], where metallic ink is printed onto convex and concave hemispherical surfaces in the form of conductive meander lines. Modifications to meander lines and feed structures had been suggested to obtain a dual-band antenna [25]. The antenna displays its first resonance at 520 MHz with only -6 dB in terms of reflection coefficient. The state-of-art [25] of a 3-D dual-band dome antenna exhibit a poor match with a complex feeding network, which opens the opportunity to improve the work.

1.2 Motivation of this thesis

I have been working on several projects during this thesis with two main objectives, the first is to design 3-D UWB metallic antennas for ground and imaging applications as well as a dual-band antenna for overhead line monitoring systems, and the second is developing fast numerical methods to simulate large circular antennas array while accounting for the contribution of ground on antennas. These projects also allowed me to acquire experience in manufacturing and measurement of metallic and printed antennas. Most research [26] presents antennas as just point sources in simulations, so we first tried to fully simulate the behavior of 3-D antennas and to go further than simulations and provide UWB radar prototypes allowing us to validate theoretical concepts. One wide line in this thesis is to improve the performance of traditional Vivaldi antennas to arrive at compact and efficient prototypes. Dealing with Vivaldi antennas is quite challenging due to their complex geometry. The experience acquired in the field of 3-D metallic antennas could be extended to the analysis and design of multi-band antennas for wireless communication. The other line of research relates to accelerating the simulation process of applying the Green's function for layered media when a nearby medium gets close to a given antenna. It is important to be able to accelerate the simulation process such that, later, numerical analysis can be inserted into an optimization loop, in order to improve the performance of the antenna with respect to sensitivity criteria. In all our developments in this thesis, the Method-of-Moments technique will be used. Fast numerical methods have been developed in this thesis based on the MoM to either solve large circular antennas array or to add the contribution of the ground on the antenna.

1.3 Objectives and novel contributions

The general objective of the thesis is to add deep perceptions into the design and analysis of antennas and arrays for ground-penetrating, imaging, wireless applications, and to contribute to the development of fast numerical methods to analyze large antenna arrays and to add the contribution of ground on antennas. It intends to present the design of 3-D single, dual-band and circular UWB antennas providing numerical simulations and validation with measurements. A special attention will be given to circular arrays of inward-looking antennas, devoted to near-field imaging. Ten connected 3-D elements in a circular configuration allow a sufficient space inside the array to image the object under test. Also, choosing an even number of elements allows one to find pairs of elements exactly in front of each other, which is favorable to radio tomographic imaging. The novelty of the ground contribution on antennas consists of avoiding the explicit use (or pre-computation) of the Green's function by introducing the ground via a reflection coefficient in 2D spatial-spectrum domain. This allows the estimation of a matrix that exclusively computes the contribution of the ground to the MoM impedance matrix of the antenna. This is then added to the free-space MoM matrix, which can be computed once and for all. Moreover the extra matrix including the ground contribution can make use of precomputed radiation patterns for every basis function on the antenna, which are independent from the ground parameters.

The thesis is divided into seven chapters covering the design of 3-D single and circular Vivaldi antenna array for near-field imaging applications, the design 3-D single Vivaldi antennas for water leak detection and the design of a 3-D dual-band bulb antenna for overhead line monitoring systems. The second part focuses on fast numerical methods to account for the contribution of ground on antennas and to simulate large antennas array with the help of ASM, Macro Basis Functions (MBF) and Contour-FFT (C-FFT) approaches.

The outline of the thesis is as follows. Chapter 2 describes the design of 3-D circular antenna arrays for near-field imaging applications. We started from the design of a traditional single Vivaldi antenna, then we improved its bandwidth by adding a new degree of freedom in the Vivaldi design. When the single Vivaldi prototype is validated by measurement, it is employed in a circular array of 10 elements, which we later named as the "Wheel-of-Time" (WoT) prototype. The ASM method applied to the MoM is applied to simulate the full antennas array.

Chapter 3 deals with near-field imaging algorithms while using the Wheel-of-Time (WoT) prototype. The near-field radiation of the WoT in the area of radiation exposure is studied and tested, while discussing the mutual coupling phenomenon between the elements. The WoT prototype is used to image and localize metal targets from time-domain responses. Also, we used the prototype to distinguish between two different metal cylinders. Finally, we deal with a dielectric target in order to image it with the help of the WoT.

Chapter 4 presents the design of a 3-D UWB Vivaldi antenna for water leak detection application. This work relates to the SENSPORT project funded by Région Wallonne. A novel Vivaldi antenna design, with larger dimension and bandwidth than presented in Chapter 2, is detailed in this chapter. The effect of modifying the traditional design of the Vivaldi antenna is discussed. Since the antenna will be very close to the ground, the near-field radiation has to be verified to ensure a sufficiently homogeneous response for near-field imaging. The contribution of ground on the antenna characteristics was evaluated using the CST commercial software, which obliged us to consider a huge cube of medium below the antenna. Such a large antenna combined with a huge cube of soil medium consumes a lot of time and memory during the simulation process. Also, the whole process needs to be repeated when changing any of the ground parameters. These limitations lead us to develop a fast method to include the contribution of the ground in Chapter 5.

Chapter 5 details the mathematical formulations of a novel fast numerical method able to include the contribution of the ground on the antenna response. We named the method as Fast Ground Coupling Matrix (FGCM). The FGCM method is validated with respect to the brute-force MoM approach and commercial software for a metal interface. Experimental validation is realized in the case of Perfect Electrical Conductor (PEC) and lossy media. The performance of the proposed method is discussed by comparing the FGCM computation times against reference solutions.

The previous chapter takes the case of a single radiator placed vertically above ground. Chapter 6 deals with analyzing large antennas arrays placed vertically nearby muli-layered substrates. The FGCM method is combined with MBFs and C-FFT methods. The MBFs method is used to reduce the computational complexity of the brute-force MoM technique. The C-FFT method, developed in the Ph.D thesis of Shambhu Nath Jha, is used to accelerate the evaluation of MBF integrals with $Nlog_2N$ complexity for the interactions involving reflection by the ground. In this case, the method is extended to 3-D antennas placed above the ground. Numerical validation of the proposed method is provided.

Conclusions and perspectives are presented in Chapter 7.

3D Circular Antennas Array for Near-Field Imaging Applications

2

The purpose of this chapter is to present a compact array design devoted to near-field radar imaging applications. In order to observe the target from all aspects angles, the array is composed of inward-looking elements. The efficient numerical analysis of the array becomes possible through the use of the Array Scanning Method (ASM). We first show a 3-D single traditional Vivaldi antenna. Then we develop the traditional design of Vivaldi antenna to fit the circular antenna array configuration. The optimization of main antenna parameters are evaluated with brief literature review on tapered slot profiles. The geometric parameters related to the elliptical curve of the Vivaldi antenna, i.e., major and minor radii and center, are introduced as additional design parameters. Second, a 3-D circular array of 10 electrically connected elements is simulated using the ASM applied to the Method of Moments, where the ASM appears as a computationally efficient approach for simulating large sectoral symmetrical structures. Finally, we show a UWB radar imaging prototype comprising 10 antennas elements with good agreement between measurement and simulation. This prototype will be used in the following chapters for near-field imaging and for the localization of targets in the area of radiation exposure.

This chapter is organized as follows. Section 2.1 presents a brief introduction about Tapered Slot Antennas (TSA) profiles. The design of a compact 3-D Vivaldi antenna is provided in Section 2.2 with main antenna parameters optimization. Section 2.3 presents the 3-D circular Vivaldi antenna array structure, as well as simulation and measurement results. Conclusions are drawn in Section 2.4.

2.1 Introduction

Ultra-wideband radar imaging systems involving arrays have a great interest in various short-range applications, such as medical imaging [27], through-the-wall observation and airport security. Large fractional bandwidth and small dimensions are critical challenges in the design of such arrays. Large bandwidth is very important for well-controlled pulse generation and high resolution. Recent studies devote great interest to lower frequencies, which becomes a challenge for antenna miniaturization. Also, high resolution can be obtained by using high frequencies. The UWB technique is widely exploited in the field of medical imaging, in order to satisfy the constraints of sufficient human body penetration and image resolution [28]. Tapered Slot Antennas (TSA), also named "Vivaldi" antennas by Gibson [8] when he showed the exponentially tapered slot antenna, are known for their ultra-wide bandwidth, light weight, and simplicity in terms of geometrical configuration, making TSA great candidates for the unit cell of antenna array systems. Printed Vivaldi antennas on substrate have been used in several imaging systems [29]. Recent studies turned to metallic antennas to reduce loss in the dielectric material [30]. Tapered slot antennas can be seen in several forms, as shown in Fig. 2.1 [31]. The most popular Vivaldi antenna profile is the exponential type (Fig. 2.1 (a)), and it is known for wide bandwidth with minimal length. T. Wu and R. King have proposed full details of an exponential shaped antenna with lumped resistor loading to suppress any reflections from the end [32]. Further work regarding the improvement of the resistively vee dipole (RVD) is proposed by modifying the exponentially taper of Wu-King profile [33]. Prasad and Mahapatra introduced linear tapered slot antenna (LTSA) [34] (Fig. 2.1 (b)). The LTSA main parameters are the height and flare angle. The elliptical profile is also widely used since this curve is tangential to the slotline and to the aperture, allowing the flare to avoid angular points (Fig. 2.1 (e)). This feature allows one to minimize the discontinuities in the radiating structure [35]. R. Lee et al. [36] investigated the effects of the tapered profile and of the curvature of the mounting structure on tapered slot antennas, and it is found that both exponential and elliptical profiles have significant effects on the gain, beamwidth, bandwidth and cross-pol level of the tapered slot an-

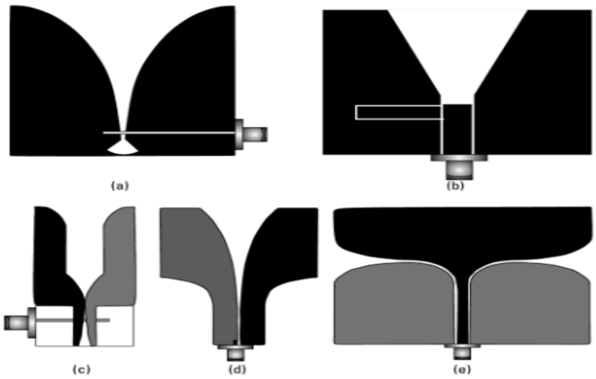

Figure 2.1: Various taper profiles for planar UWB antenna: (a) exponential; (b) linear; (c) constant width ; (d) dual exponential; (e) elliptical.

tennas. A similar study is evaluated by P.H. van der Merwe et al. [37] using a quad-ridged horn antenna, where the Vivaldi profile could be used in forming the horn antenna profiles. The four investigated profiles were an exponential profile with a linear taper, an elliptical profile, a cubic Bézier profile and an exponential profile with a circular segment near the aperture. The exponential and elliptical profiles yielded similar acceptable performance in the high-frequency region, but high VSWR results in the lower portion of the frequency band.

A uniform circular array (Fig. 2.2) can provide 360° azimuthal coverage and estimate source elevation angle (outside the plane of the array). In view of the cyclical symmetry of the array, the embedded element patterns are identical [38]. Circular arrays configurations are reported for many applications such as medical imaging [39] and direction finding [40]. In the current work, 10-connected metallic elements were arranged in a circular array to form the UWB imaging system, which we called the "Wheel-of-Time" (name proposed by Eloy de Lera Acedo from University of Cambridge). The "Wheel" is inspired from the circular array topology and the "Time" due to using time domain responses for near-field imaging. New design solutions for Vivaldi antennas were applied to improve the antenna efficiency over the bandwidth of interest. The new method is based on the formulation of the tapered slot shape, which is the main element of the antenna characteristics.

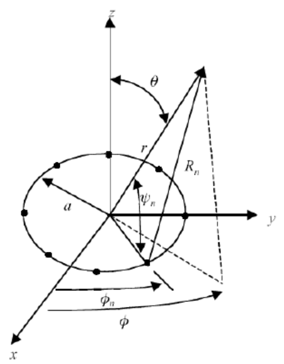

Figure 2.2: Circular array configuration.

2.2 Design and fabrication of a 3-D single Vivaldi antenna

In the first steps of this research, we started the design of the circular antenna array by the design of a single traditional Vivaldi antenna. Then we modified the design to fit the circular antenna array, with new design solutions to improve the antenna bandwidth.

2.2.1 Traditional Vivaldi antenna design

The proposed design has the following dimensions (Fig. 2.3):

- Width a=10 cm, length b=7 cm.
- Circular cavity of diameter D_{ca}=2.8 cm.
- Feed region: $W_{sl} = 0.25 cm.Thickness of 0.5 cm.$
- Type of taper profile: elliptical.

The antenna is designed and meshed using the GMSH [41] freely-available software. A software developed at UCL based on the Method of Moments (MoM) code is used to simulate the different structures.

2.2.2 Modified Vivaldi antenna design

The previous antenna geometry has been changed to fit the design of the circular array as shown in Fig. 2.4. The effect of modifying the traditional Vivaldi

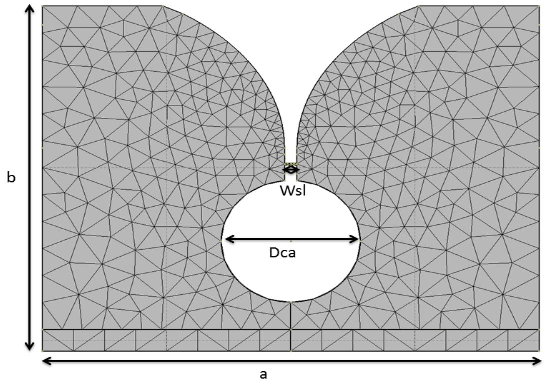

Figure 2.3: Layout of the 3-D traditional Vivaldi antenna.

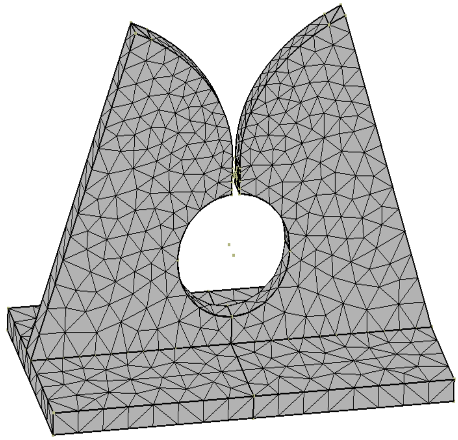

Figure 2.4: Mesh view of the 3-D modified Vivaldi antenna.

antenna to fit the circular array configuration is presented in Fig.2.5, where a better cut-off frequency is obtained in the traditional Vivaldi antenna due to the larger width at the end of the taper profile compared to the modified one.

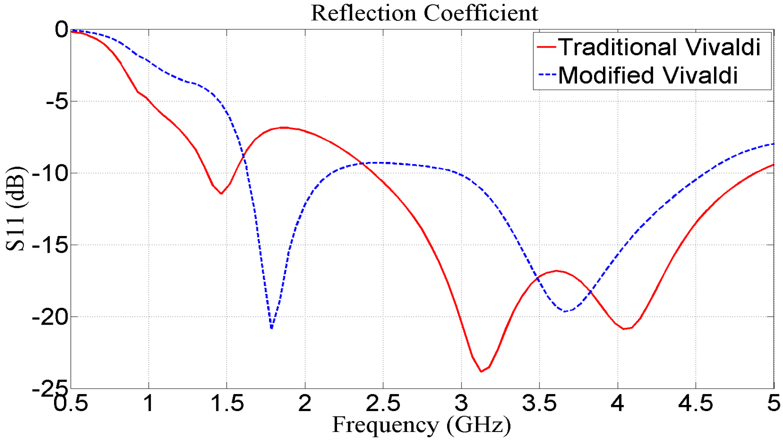

Figure 2.5: The influence of modifying the traditional Vivaldi antenna.

The simulation result exhibits a bandwidth from 1.6 GHz to 4.6 GHz with respect to a -10 dB matching criterion, except for the slightly inconvenient peak between 2 and 3 GHz.

2.2.3 Vivaldi antenna optimization

The parameter study is carried out versus three main dimensions to be optimized: antenna thickness, circular cavity diameter and antenna feed width. Only one parameter is varied at a time, while all other parameters are fixed to the values defined in Section 2.2.1.

2.2.3.1 Antenna thickness influence

Three different antenna thicknesses are chosen in this optimization 5, 10 and 15 mm to find the maximum antenna bandwidth. The results are shown in terms of real and imaginary parts of input impedance, and reflection coefficient with reference to 50 Ω. The effect of antenna thickness appears significantly on the antenna bandwidth, where by increasing the antenna thickness a reduction in the antenna bandwidth is obtained (Fig. 2.6). Another observation is that there is virtually no influence of the thickness on the lower frequency which is mainly affected by the antenna width.

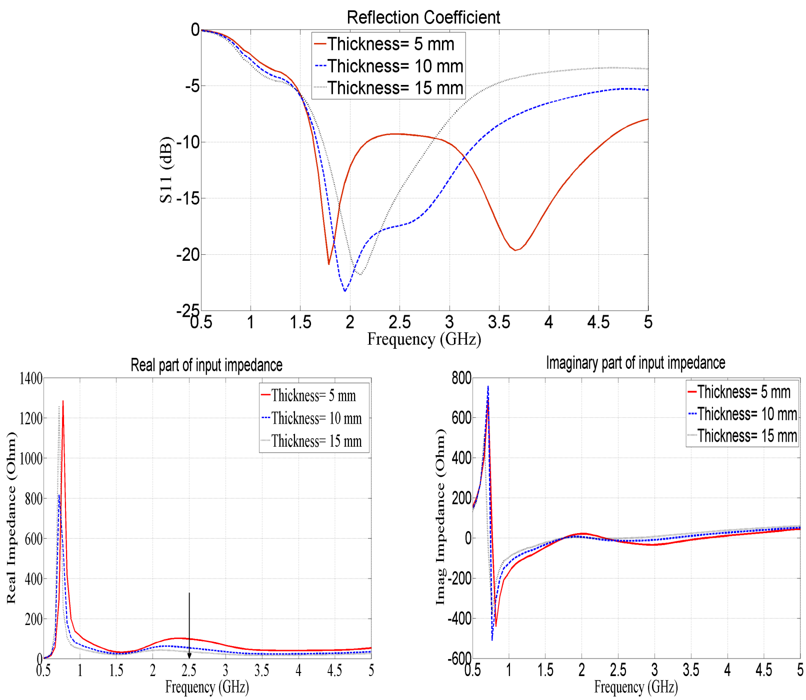

Figure 2.6: Effect of thickness on antenna impedance

2.2.3.2 Circular cavity diameter influence

We varied the circular cavity diameter from 16 to 28 mm. The direct connection between the circular cavity diameter and the reflection coefficient is clearly observed in Fig. 2.7. Increasing the cavity diameter value decrease the antenna reflection coefficient, which produces a wider bandwidth below the -10 dB criterion. On the other hand, it is shown that the circular cavity has practically no effect in defining the lower frequency. The higher frequency limit improves with decreasing the circular cavity diameter. The value of circular cavity diameter chosen in this optimization represents a trade-off between having the highest high frequency limit and remaining as far as possible below the -10 dB criterion, where the problem of slightly inconvenient peak between 2 and 3 GHz is solved in Section 2.2.4.

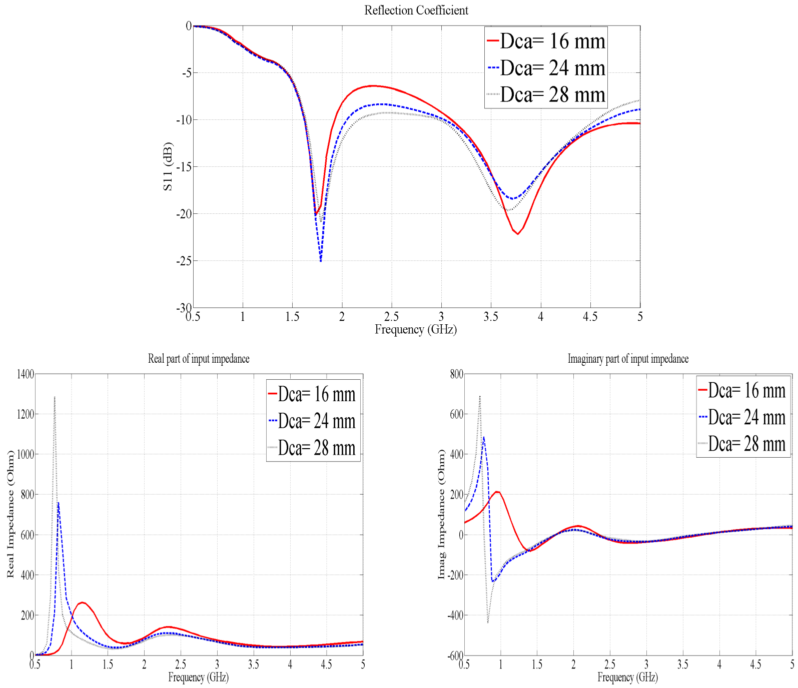

Figure 2.7: Effect of thickness on antenna impedance

2.2.3.3 Feed width influence

The variation of the feed width is taken from 2.5 to 4 mm. The length of the feed is fixed at 2.5 mm. Several insights are observed in this parameter. increasing the slot width has an inductive effect on the antenna impedance through increasing the imaginary part of the impedance. Decreasing the slot width slightly improves the lower frequency limit, where a significant improvement appears in the high frequency limit. Overall, decreasing the slot width increases the antenna bandwidth.

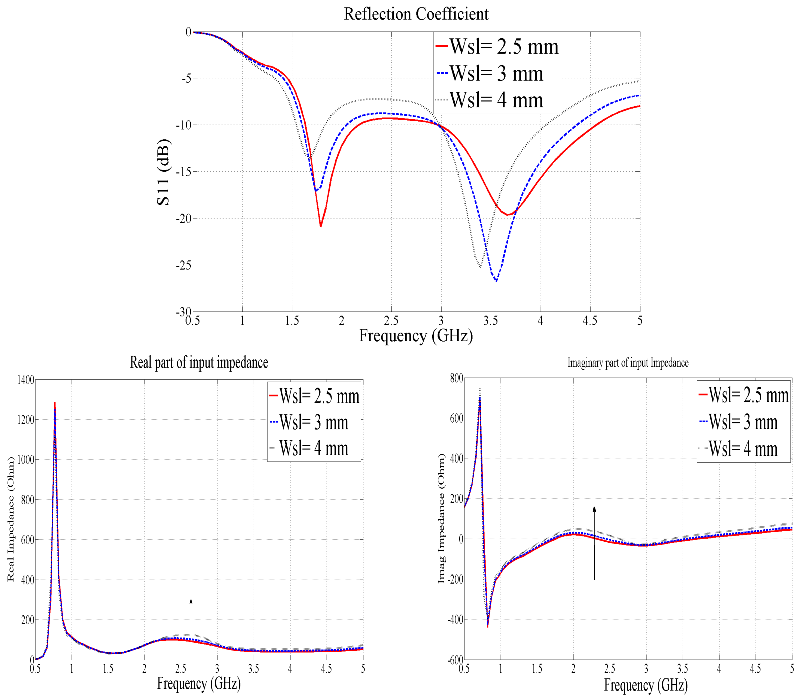

Figure 2.8: Effect of feed width on antenna impedance

It is recommended to affix a ground plane beneath the antenna to hold the antenna properly, and to improve the isolation between the feeding port and the antenna body. The width of the ground plane is chosen to 10 cm, and the thickness to 5 mm for the optimized behavior. The effect of adding the ground plane mainly appears at lower frequencies (Fig. 2.9). The effect of the ground plane dimensions is shown in Fig. 2.10, where a larger ground plane produces a lower cut-off frequency. A larger ground plane contributes in increasing the antenna width, which may helps improving the cut-off frequency. To solve the problem of the inconvenient peak between 2 and 3 GHz, and to optimize the antenna for the entire required frequency band of 1.6 GHz to 4.6 GHz more parameters should be played with.

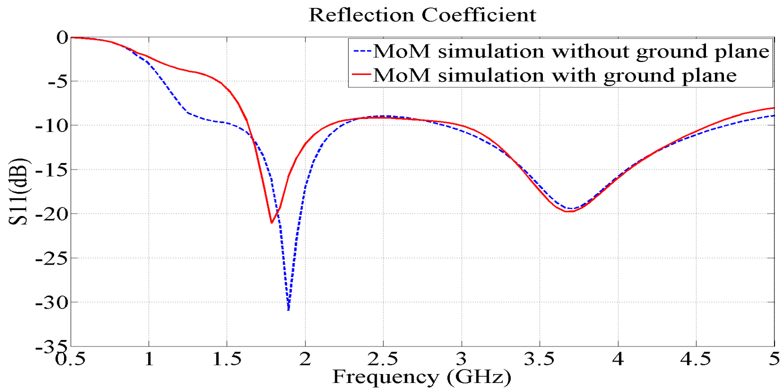

Figure 2.9: The effect of adding the ground plane on the reflection coefficient.

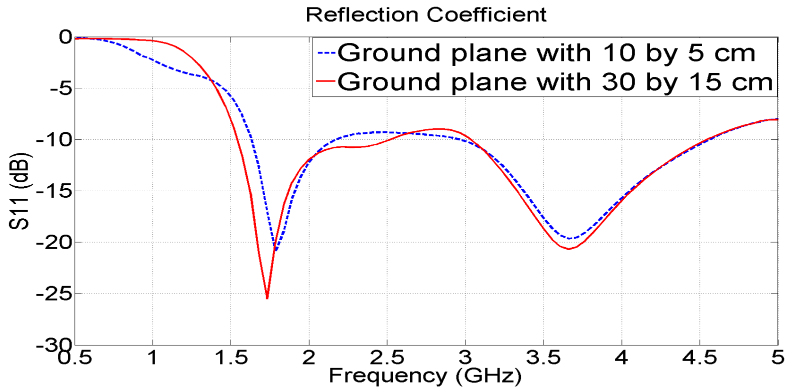

Figure 2.10: The effect of ground plane dimensions on the reflection coefficient.

2.2.4 The improved 3-D Vivaldi antenna

The taper profile is the most important part of the Vivaldi antenna. Also, it is possible to consider this radiator as operating a good matching between the transmission line and free space. The distance between the positive and negative charges identifies the frequency of radiation for two wires [42]. Vivaldi antennas are often designed with an elliptical taper profile. The taper profile of a Vivaldi antenna represents the two wires in this case, where it provides all possible distances between them from the higher frequencies (minimum distance) to lower frequencies (maximum distance). As a result, the shape of the taper profile is crucial for the antenna performance. The geometric design

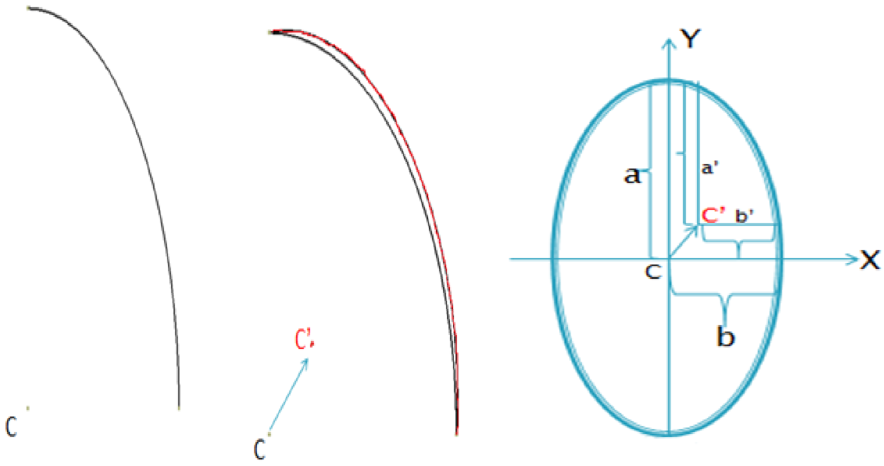

Figure 2.11: If one wants to move the ellipse center from $C(x_c, y_c)$ to $C'(x'_c, y'_c)$ while keeping the start and end points of the elliptical arc at specific positions, it is necessary to recalculate the major and minor radii, a' and b' respectively.

of a Vivaldi antenna includes an elliptical arc, which can provide an additional degree of freedom in the antenna design to improve its performance. By keeping the start and end points of the arc at pre-determined positions, one can obtain a set of center positions and corresponding major and minor radii for optimization, as illustrated in Fig. 2.11.

The elliptic profile is parameterized as:

$$\frac{(x - x_c)^2}{b^2} + \frac{(y - y_c)^2}{a^2} = 1 \tag{2.1}$$

where $C(x_c, y_c)$ is the ellipse center. Let us consider the known points $S(x_1, y1)$ as the start point of the arc, and $E(x_2, y_2)$ as the end point.

$$(x_1 - x_c)^2.a'^2 + (y_1 - y_c)^2.b'^2 = a'^2.b'^2 \tag{2.2}$$

$$(x_2 - x_c)^2.a'^2 + (y_1 - y_c)^2.b'^2 = a'^2.b'^2 \tag{2.3}$$

By subtracting (2.2) from (2.3), we get

$$\frac{a'}{b'} = X = \sqrt{\frac{(y_2 - y_c)^2 - (y_1 - y_c)^2}{(x_1 - x_c)^2 - (x_2 - x_c)^2}} \tag{2.4}$$

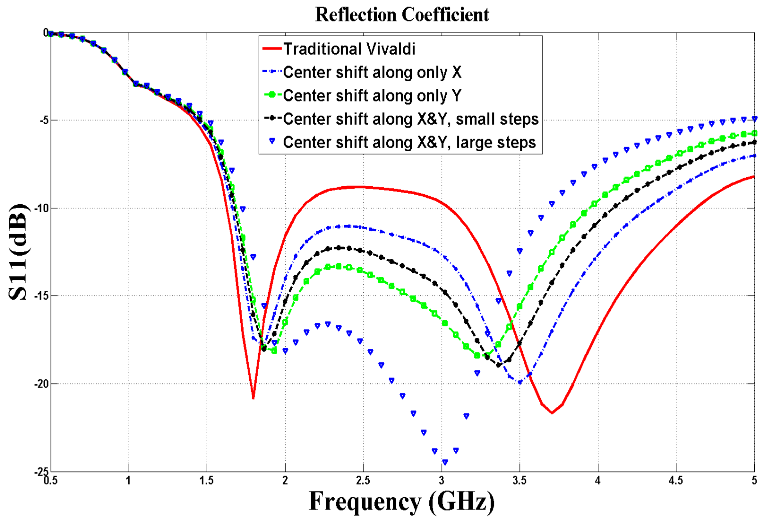

Figure 2.12: Reflection coefficients obtained by changing the ellipse center along X and Y axes.

then

$$
\begin{aligned}
b' &= \sqrt{\frac{(x_1 - x_c)^2.X^2 + (y_1 - y_c)^2}{X}} \\
a' &= \sqrt{(x_1 - x_c)^2.X^2 + (y_1 - y_c)^2}
\end{aligned}
\tag{2.5}
$$

The last two parameters can be easily calculated from the start and end points of the elliptical arc, and the position of the new ellipse center.

This technique has been applied to the 3-D single Vivaldi antenna. The simulation results confirm the importance of optimizing the elliptical curve in the Vivaldi antenna, as seen in Fig. 2.12. The ellipse center has been shifted for many positions along only X, only Y and X&Y axes. 0.4 cm center shift is used along the X axis only. The same value is used along the Y axis only. In the same way, giving small steps along X and Y together (0.2 cm, 0.17 cm) slightly affects the reflection coefficient, where large shifts (0.25 cm, 0.25 cm) contribute significantly to changing the reflection coefficient over the band of interest. Lowering the low frequency radiation cut-off without increasing the antenna size is one of the challenges for the design of Vivaldi antennas. From simulation results, obtained for varying positions of the ellipse, promising solutions are achieved.

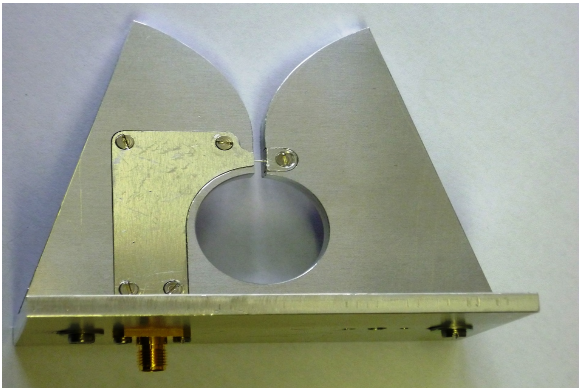

Figure 2.13: 3-D single Vivaldi prototype.

2.2.5 Fabrication of a 3-D single Vivaldi prototype

Notch-antenna feeds are usually comprised of a stripline-to-slotline or microstrip transitions [43]. This complex feeding adds significant losses, and affects the sensitivity of the receiving arrays. One of the best solutions to overcome this problem consists of considering the feed as one of the built-in 3-D metal antenna component such as the 3-D Vivaldi circular array [48]. A 3-D thick Vivaldi antenna has many advantages such that it can be made hollow, so it is possible to include the low-noise amplifier, protected from the external fields and close enough to the antenna feeding point. The 3-D compact metal Vivaldi antenna has a light weight of 200 g. A direct coax feeding technique is used (Fig. 2.13). The antenna is designed and simulated using the CST Microwave Studio commercial software for one more validation against the Finite Integration Technique (FIT). Fig. 2.14 compares simulations versus measurement in terms of the reflection coefficient, and it indicates a relatively strong correspondence. The small differences between the simulations is due to using two different mesh lengths. For MoM simulation, we discretized the antenna using different mesh lengths; the region near the feeding point and the elliptical taper profile needs a smooth meshing, while the mesh of the edge part of the antenna can support a coarse meshing. The single prototype covers a bandwidth from 1.6 GHz to 4.6 GHz with respect to a -10 dB matching criterion in terms of reflection coefficient.

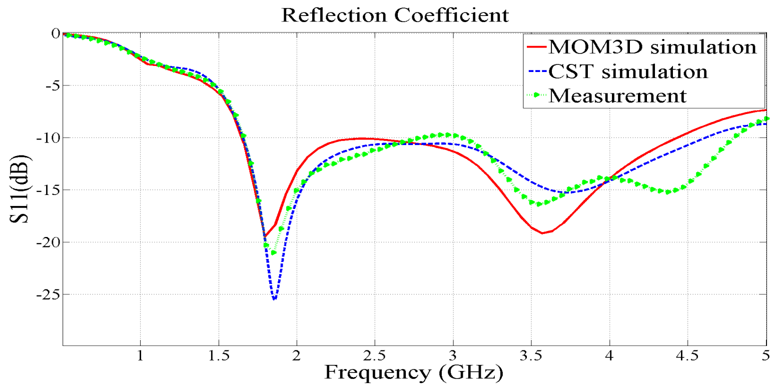

Figure 2.14: Comparison between reflection coefficients obtained from simulations MoM3D, and CST and measurement.

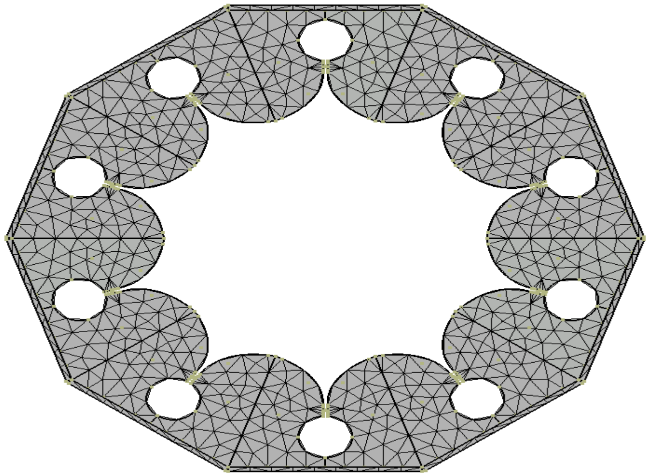

Figure 2.15: Mesh of 3-D circular Vivaldi array.

2.3 Design and fabrication of 3-D circular Vivaldi antennas array

Ten Vivaldi antennas are arranged in a circular array with length of 32.4 cm and width of 30.7 cm and an inner diameter of 15.2 cm (Fig. 2.15). One reason for choosing 10 elements is to obtain a sufficient space (diameter of 15.2 cm) to image the object under test. Another one is to dispose of sufficient ports, providing enough information through the scattering process. We consider the case of excitation at one port in the circular array, while the remaining antennas are passively terminated.

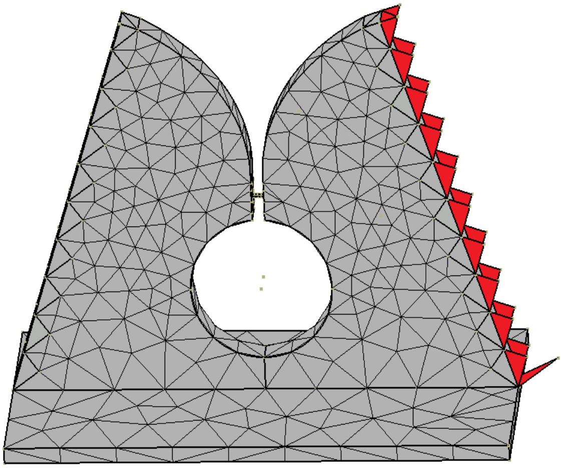

Figure 2.16: Meshed single Vivaldi antenna with connecting basis functions (highlighted in red).

2.3.1 Simulation of large circular Vivaldi array by the array Scanning Method (ASM)

The array Scanning Method (ASM) [44] was applied in [45], for the accurate solution of finite-by-infinite arrays excited at a single port. In the case of a circular array of N elements excited at one port, while the remaining antennas are passively terminated, the currents can be obtained by using the phase mode excitations [46], with the help of the ASM [47] [48]. The current excited at antenna m for antenna 0 active appears as:

$$I(m) = \frac{1}{N} \sum_{p=0}^{N-1} I^{\infty}(\Psi_p) e^{-jm\Psi_p} \tag{2.6}$$

where $I^{\infty}(\Psi_p)$ is the current distribution when all the N elements are excited. Ψ_p is the phase shift between elements, and it is equal to $\Psi = p\,\frac{2\pi}{N}(0 > p > N-1)$.

Overlapping basis functions (highlighted in red color) are used to ensure the flow of current between successive elements (Fig. 2.16), and to get the exact results (within limits implied by discretization).

We observe in Fig. 2.17 that the results obtained by applying the ASM-MoM and brute force methods are practically identical. The ASM method helps us to reduce the computation time without affecting the accuracy of the input impedance. Computation times for 80 frequency points are given in Table 2.1 .

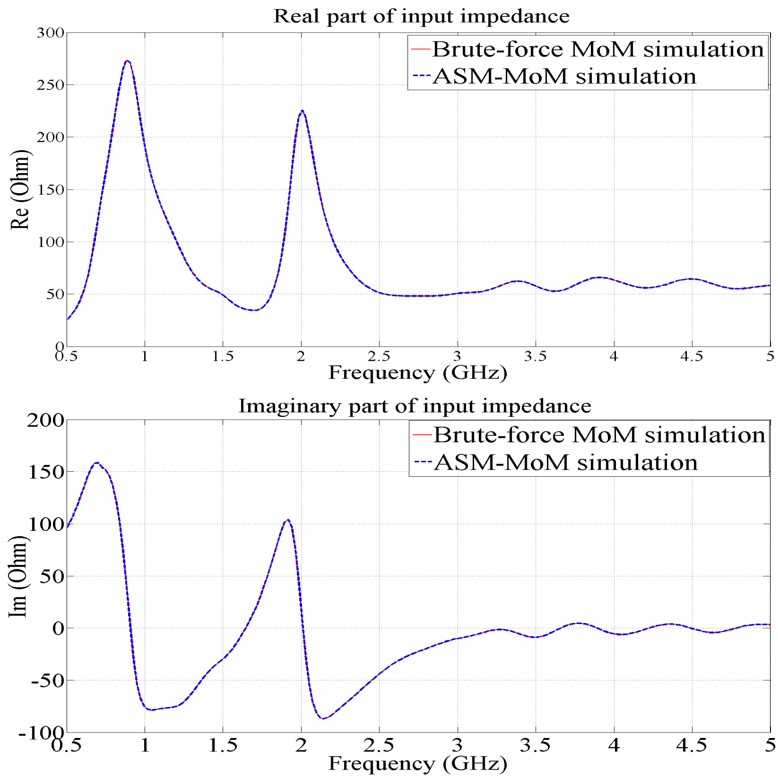

Figure 2.17: Real and imaginary parts of the antenna input impedance.

Table 2.1: SIMULATION TIMES.

Brute force-MoM elapsed simulation time	16 hours
ASM-MoM elapsed simulation time	1 hour 36 min

2.3.2 Wheel-of-Time array prototype

The configuration of the proposed UWB microwave imaging system is illustrated in Fig. 2.18. Plexiglas and copper frames are added to the prototype's body to properly arrange the cables coming out from the array elements. The effect of adding the frames on the array had been tested, and no influence has been found on reflection coefficient.

The configuration of the proposed imaging system has a complex geometry, where in the case of activating two elements (transmitter and receiver), the receiver will not just catch the signal sent from the transmitter, but also the reflected signals coming from other elements. Despite this complexity,

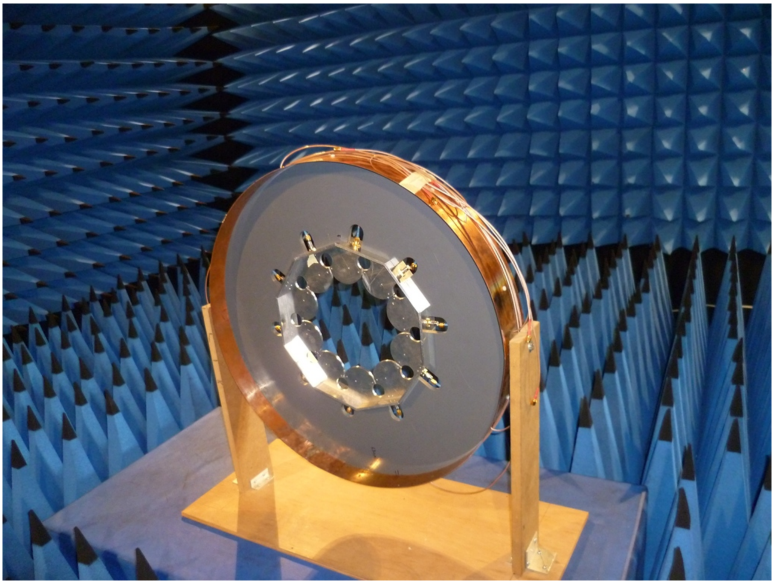

Figure 2.18: Wheel-of-Time prototype.

Fig. 2.19 shows a very strong agreement between the simulations obtained by ASM method applied to MoM and the measurement. The measurement has been made at the WELCOME facility of UCL using a 4-ports Vector Network Analyzer (VNA).

The measurement results validate the ASM method as an efficient method to simulate large circular antennas array.

2.4 Conclusion

In this chapter, the design, simulation and fabrication of a 3-D circular array of Vivaldi antennas were presented for UWB near-field imaging. First, the 3-D single Vivaldi antenna was designed and fabricated. Very good agreement has been obtained at impedance level between simulations obtained with MoM, CST Microwave software and measurement, with a bandwidth between 1.6 GHz and 4.6 GHz. An additional degree of freedom in the Vivaldi antenna design is added by modifying the major and minor radii of the ellipse curve, as well as the position of the center with respect to the feeding point. Second, a 3-D UWB circular imaging prototype consisting of 10 Vivaldi elements has been manufactured. We named the prototype as "Wheel-of-Time". A fast calculation method has been proposed based on the ASM method applied to the MoM to simulate large circular arrays. Excellent agreement has been obtained between the ASM-MoM simulation and measurement in terms of reflection and transmission coefficients. This good correspondence validates the ASM-MoM as the best solution to analyze large circular antennas array. A calibration algorithm will be very useful to remove the very small discrepancies between simulation and measurement, probably due to imperfect modeling of the feed points. It is expected that the corresponding corrections will also hold in the presence of a target.

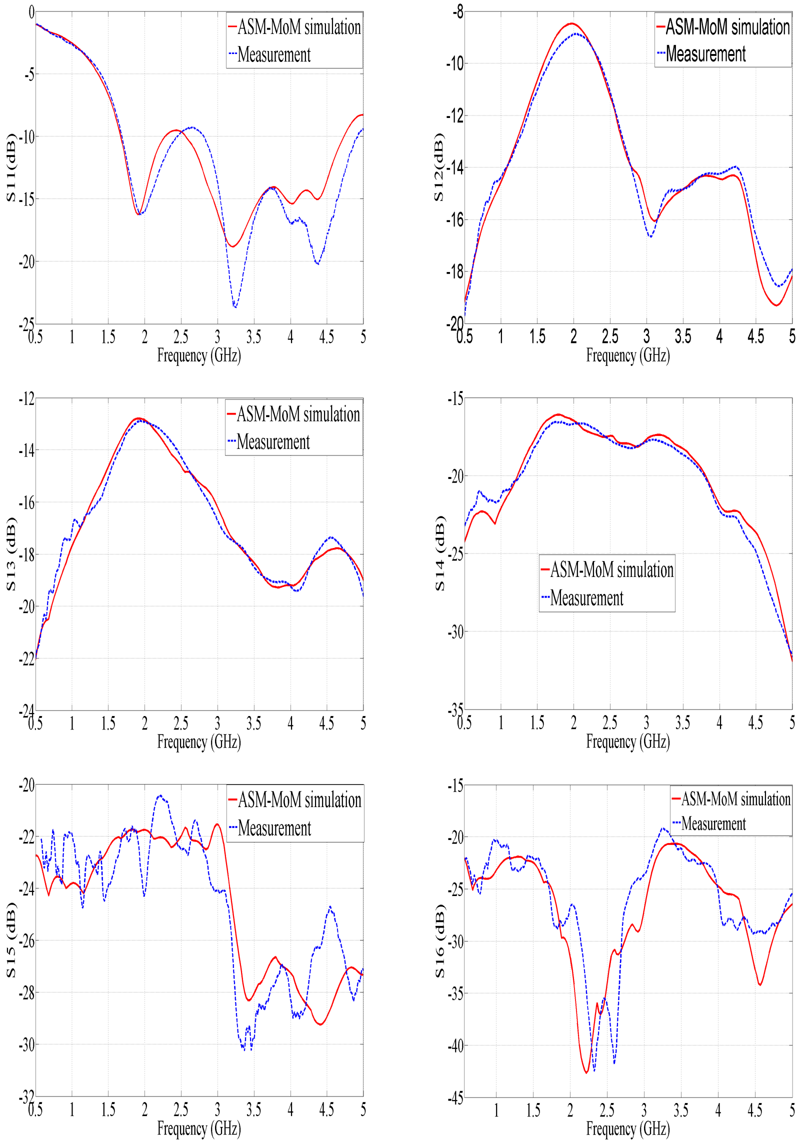

Figure 2.19: The reflection and transmission coefficients of WoT.

Microwave Imaging with the Wheel-of-Time

3

In this chapter, we will use the 3-D UWB imaging prototype, which we named "Wheel-of-Time" (WoT), to image and localize targets in the area of radiation exposure. First, we study by simulations the near-fields in E and H directions in the area of radiation exposure. Second, time-domain responses of a target under test (TUT) are processed. An initial near-field image of the target under test in the area of radiation exposure is depicted, and the target is localized. An initial near-field image of a Dirac source in the area of radiation exposure is depicted, and the target is localized. Finally, the UWB circular array with two different metallic cylinders had been simulated using the ASM applied to the Method of Moments. The resolution between metallic cylinders is investigated experimentally and numerically. Preliminary results are also provided regarding reconstruction of a dielectric cylinder positioned in the area of radiation exposure.

3.1 Introduction

Ultra wide band radars have a great potential for use in near-field imaging applications such as medical imaging [66], ground penetrating radars and industrial quality control. Such applications require the use of a large bandwidth to enable high resolution imaging of the target, in order to properly identify the object shape and composition. The high frequencies of the UWB pulses provide the high resolution, whereas the low frequencies enable better material penetration, especially for biological materials.

One approach to image a target is radar-based. A short-time pulse is sent toward the target under test using one or more antennas. In the presence of a target, reflections can be measured and inform us about the composition of the object.

It is often desirable to have multiple pairs of elements, such that is possible to gather more information about the object under test. Ultra-wideband time domain systems have been used for microwave imaging [67]. The work in [67] focuses on medical applications of microwave imaging, and the study has concentrated on the effects of random errors. The model is able to detect two tumors with radius of 5 mm at 10 cm wavelength. Craddock et al. [68] uses an array of 31 hemispherical elements for breast cancer detection. The reconstructed images shows clearly a 7-mm-diameter spherical phantom tumor at 10 cm wavelength. Short-range applications, such as free-space surveillance, airport security and concealed weapon detection have used 3-D imaging systems which provides high resolution images. In [69], a new class of MIMO array configurations with lower shadowing is proposed. The proposed 2-D MIMO array achieves about 2-5 dB side-lobe level higher for the reference arrays (by 150% fractional bandwidth 2 degree angular resolution and overall -22 dB grating/side-lobe level with only 25 antenna elements). L. Monte et al. used RF tomography technique for below-ground imaging [70]. The reconstructed image using homogeneous Green's function showed the two hollow cylinders (radius 1 m) emulating two tunnels, located at a depth z = -5 m, having $\epsilon_D = 9$ and $\sigma_D = 5 \times 10^{-4}$ S/m. G. Gennarelli et al. used RF/microwave imaging to localize sparse targets in urban areas [71]. The imaging technique, in the framework of 2-D linear inverse scattering, tried to localize electrically small PEC scatterers, arbitrarily located in the investigation region. The achievable imaging capabilities are validated against full-wave synthetic data provided by the truncated singular value decomposition (TSVD) inversion scheme, providing high-resolution images. The main obstacle of using stepped-frequency continuous-wave (SFCW) radars for GPR imaging is the data acquisition speed. A. Suksmono et al. [72] proposed a novel SFCW-GPR system based on compressive sampling/compressed sensing. The main advantage of this system is the reduction of the required number of samples to achieve exact reconstruction. 66 random samples are selected, giving a compression ratio of around eight times. It is shown that only 4.3 s are required using the proposed system, compared to 36.15 s are needed to obtain 512 samples in the conventional sampling scheme.

This chapter is organized as follows. In Section 3.2, we start by testing the WoT in terms of near-field radiation over the area of radiation exposure. Also, we show the mutual coupling phenomenon between the array elements. In

Section 3.3, we process frequency domain measurement data obtained from the WoT into time domain responses by performing an Inverse Fourier Transform. An imaging algorithm is implemented to give an initial localization of targets. Section 3.4 deals with Dirac source, where an algorithm is developed to localize the targets. Section 3.5 shows measurement results for two metallic cylinders, where the WoT has been used to distinguish between them. A preliminary image of a dielectric cylinder is shown in Section 3.6. Conclusions are drawn is Section 3.7.

3.2 Near-field radiation of the Wheel-of-Time

A microwave holography method [61] is applied to study the signal interference between the fields radiated by an antenna under test (AUT) and those scattered by a near-field target. Measurement of the amplitude and the phase of the near field radiated by the AUT is a common way to evaluate the potential sensitivity of the system. A brief introduction to the mutual coupling phenomenon will be presented. Then, the current distribution over all the antenna elements with a study of the near-field in the middle of WoT will be depicted.

3.2.1 Mutual coupling study

Mutual coupling is a common phenomenon in various antenna arrays, as it impacts all types of antenna array parameters, such as the input impedance and the radiation pattern. In other words, the input impedance of a single element in an array differs from that of the same element when it is isolated, due to the mutual coupling effect [73]. The near and far fields radiated by the antenna also differ in isolated and coupled configurations. Different methods have been suggested to decouple the array signals because the mutual coupling is not taken into account due to the assumption of simplified patterns. Based on the types of antenna arrays being considered and the applications in which the antenna arrays were used, different solutions are proposed [74]. Increasing the distance between the resonators [75], adding slits to the ground plane [76] and changing both resonator position and distance [77] are proposed methods to reduce the mutual coupling between elements. In small arrays, the main effect of mutual coupling appears at the antenna patterns caused by the different surrounding for each element in the array. The mutual coupling study in this section is investigated by showing the current distributions, antenna impedance and radiation patterns, with a comparison between the isolated element and the same element in the array. A comparison is made between the current distributions obtained with the isolated Vivaldi antenna (Fig. 3.1.a) and those appearing in the array (Fig. 3.1.b).

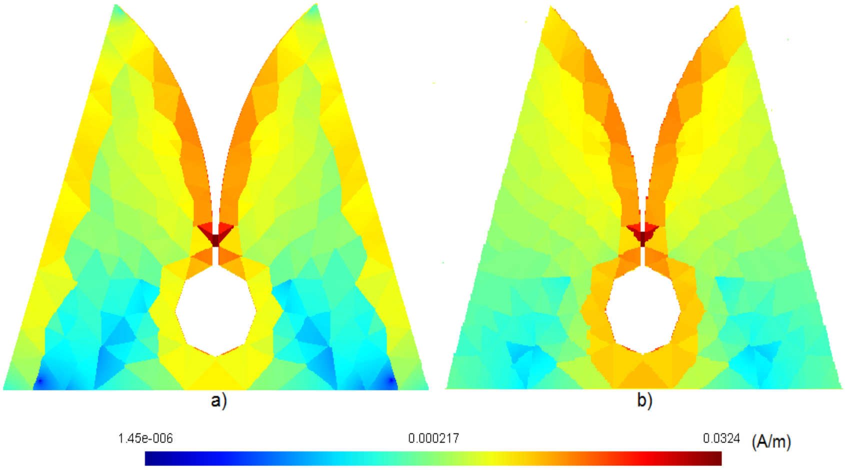

Figure 3.1: Current distribution comparison for the case of a) isolated element b) the element in the array at 5 GHz.

Fig. 3.1.b shows the appearance of higher current distribution regions compared with that of Fig. 3.1.a on the antenna body and near the circular cavity, which reflects an exchange of the current between the original radiator and its neighbors. Fig. 3.1 shows that the highest radiation of the antennas comes from a small section along the curve of the flare. Also, edge currents disappear in the connected structure. To ensure a smooth flow of the current from one element to another, overlapping basis functions (Fig. 2.15 in the previous chapter) are added to the single element. Fig. 3.2 shows the slightly positive impact of the mutual coupling on the reflection coefficient, where the cut-off frequency does not change and the higher frequency limit is shifted upward. In terms of radiation patterns, the antenna embedded element patterns will be just rotated copies of the embedded pattern of the reference antenna. However, the radiation patterns on both sides of a given antenna is no longer symmetric when the mutual coupling is taken into account. The observations from Fig. 3.3 indicate the slight asymmetries in the E and H-planes at 2 GHz.

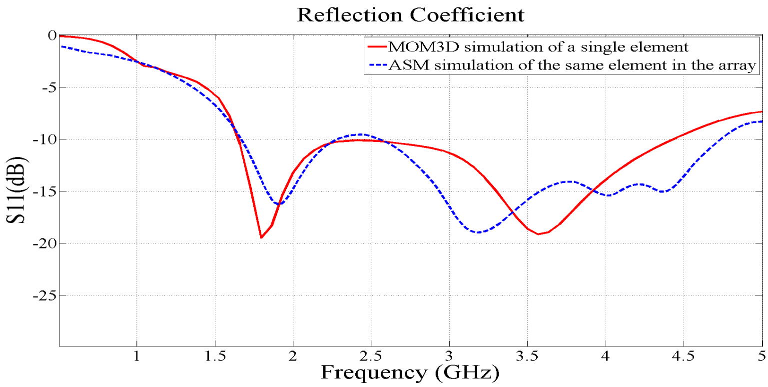

Figure 3.2: Reflection coefficient comparison between one element and the same element in the array.

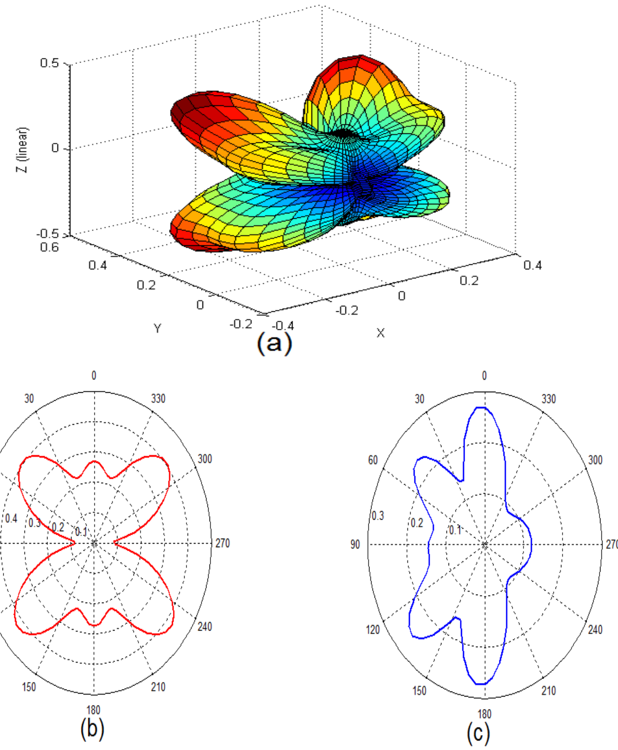

Figure 3.3: The radiation patterns in (a) 3D form (b) E-plane (c) H-plane at 2 GHz.

3.2.2 UWB Near-field radiation study

Fig. 3.4 shows that the current flows from the basic source to the other elements, where the source's neighbors are the most affected. The third and seventh elements (we count the source as the antenna 0) are less affected, probably through a combination of distance and polarization mismatch.

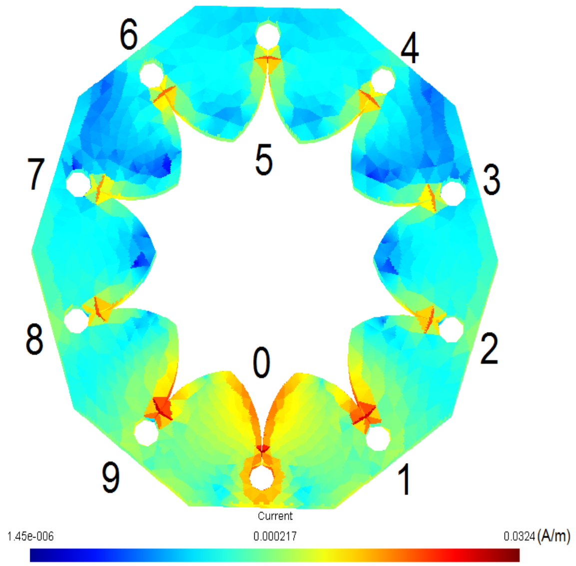

Figure 3.4: Current distribution on the 3-D circular antennas array at 5 GHz.

To know more about the near-field sensitivity, a 2D rectangular screen of testing functions is created in the UWB near-field exposure region. A function has been developed to generate the testing functions and to draw the geometrical position of the 2D screen and the antennas array (Fig. 3.5). The dimensions of the 2D screen are 6.8 $\times$ 6.2 cm, and the distance between the testing functions are 0.2 cm.

The radiated field can be obtained from the following equation, while taking into account the mutual coupling between the antennas in the array:

$$\bar{E} = \bar{\bar{Z}}_{AR} \cdot * \bar{I} \tag{3.1}$$

This tested field describes to the near-field sensitivity, where the field is multiplied by a rooftop testing functions and integrated. $\bar{\bar{Z}}_{AR}$ is the MoM impedance matrix obtained between the WoT and the 2D screen. $\bar{I}$ is the current distribution on the antenna when it is excited in the array. The testing

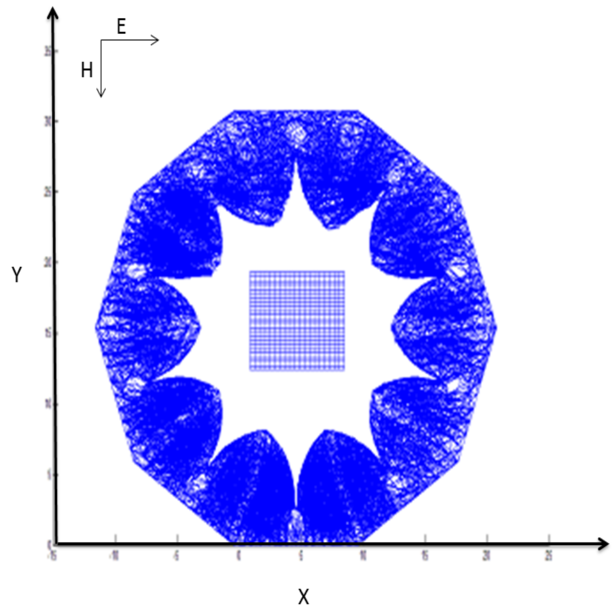

Figure 3.5: The geometrical position of the antennas array and the 2D screen.

functions are oriented according to the polarization of the antennas in the E-direction (Fig. 3.6.a), and then in the H-direction (Fig. 3.6.b).

Fig. 3.6 depicts the near-field radiation for a circular UWB array made of 10 elements, excited at one element in E and H directions. The "E" direction is perpendicular to the antenna axis. X and Y indices (a grid of 18×22 lines) refer to the 2D screen of testing function points. Fig. 3.6.a shows a larger field of view along the X axis than along the Y axis. The lower near-field radiation is located in the two furthest corners of the 2D screen from the source; this is consistent with a lower excitation of antennas 3 and 7 (Fig. 3.4). A smooth near field behavior in the middle of the antenna array is observed at 2 GHz. In Fig. 3.6.b, a line can be seen exactly in the middle of the X axis, where the cross-pol level is low. This line corresponds to the plane of symmetry of the structure that crosses the feed points. Also, despite the mutual coupling, the near-field radiation of a given antenna remains perfectly symmetrical, given the symmetry of the global structure.

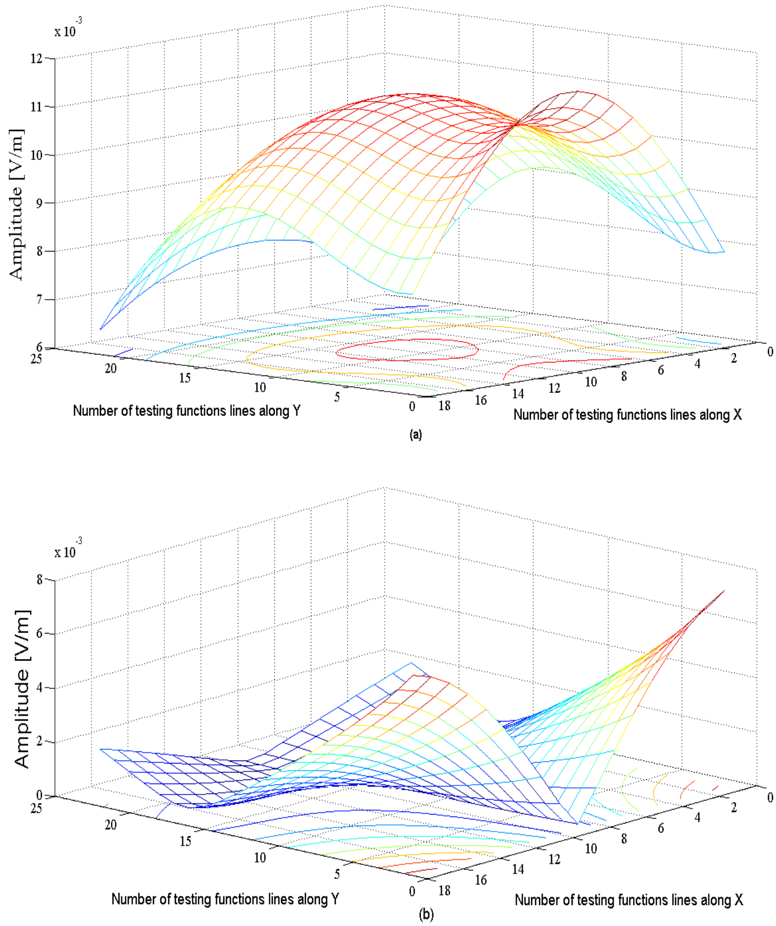

Figure 3.6: Amplitude (V/m) of the equivalent field distributions of the WoT in (a) E-direction and (b) H-direction, for one antenna excited.

3.3 Imaging and localizing targets from time domain responses

The configuration of the WoT with a reference target is illustrated in Fig. 3.7. A reference target (hollow metallic tube with a diameter of 2.25 cm and a thickness 0.3 cm) is located at the position of [-3.5 cm, -3 cm] (Fig. 3.7).

An imaging algorithm, inspired from positioning procedures described in [78] is implemented for imaging a target. The method uses the time-difference of arrival at each receiver with respect to a reference target [79]. The imaging algorithm relies on correlations $C_{r,i}$ between signals received at a given an-

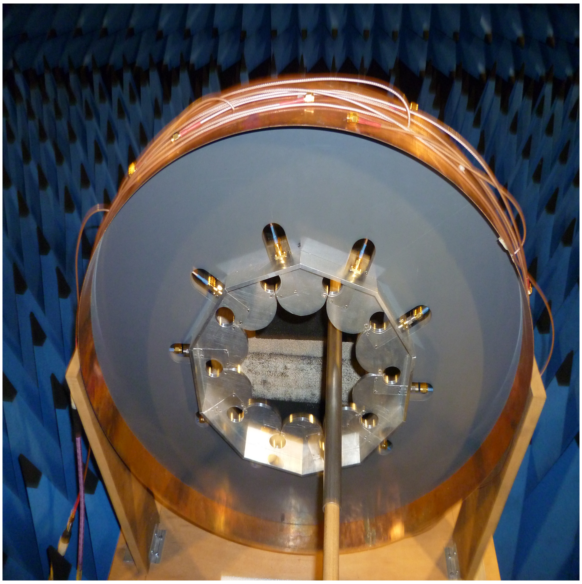

Figure 3.7: Illustration of the experimental setup of the WoT prototype with the reference target.

tenna and those predicted from a reference target with the same transmitting antenna. It is worth noting that the following measurements have been taken without fine array calibration of the WoT prototype. Time domain responses are shown in Fig. 3.8 for two cases: free space response and the response in presence of the reference target, when antenna 1 is transmitting and antenna 2 is receiving (next to each other).

The obtained impulse duration is 0.4 nanosecond. This duration indicates that the antennas present very little dispersion and are favorable to accurate localization and positioning. The same metallic tube is used as a target under test at a different position. The size of the observation field is set to 12 by 12 cm, as shown in Fig. 3.9. It is to be noted that multiple reflections between the target and the array are not accounted for by this algorithm. Fig. 3.10.b shows how difficult it is to distinguish the TUT response among signals scattered from other antennas, where more than one time domain response can be seen. For every pixel on the image map, the following time difference is calculated a priori and is tabulated:

$$\Delta t(x;y) = \frac{(TRR - TTR)}{c} \tag{3.2}$$

where $\Delta t(x;y)$ is the time difference for the round trip TRR (transmitter-

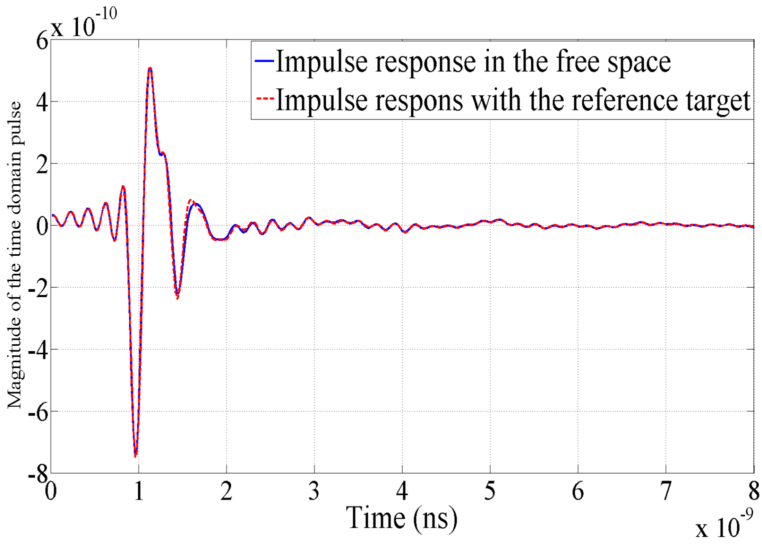

Figure 3.8: Impulse responses obtained from measurements in the anechoic chamber and VNA.

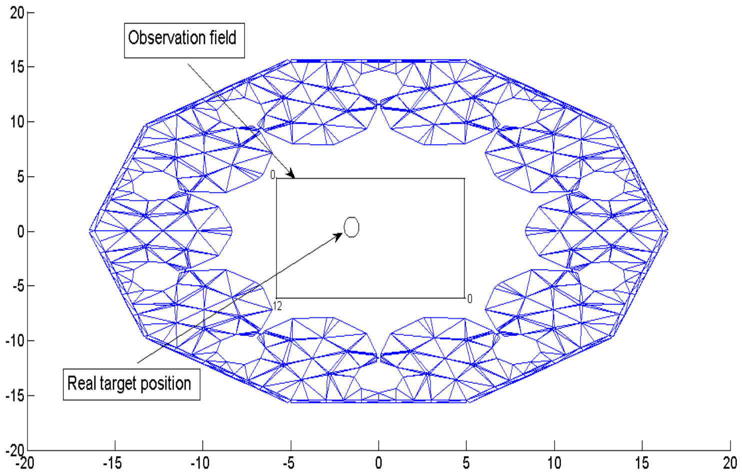

Figure 3.9: The observation field and the real target position setup.

reference-receiver) and TTR (transmitter-target-receiver) for the pixel at (x; y) as indicated in the image map, and c is the speed of light. The initial image is obtained after production of the correlation function at Δt for every pixel corresponding to all possible positions of the target in the area of radiation exposure.

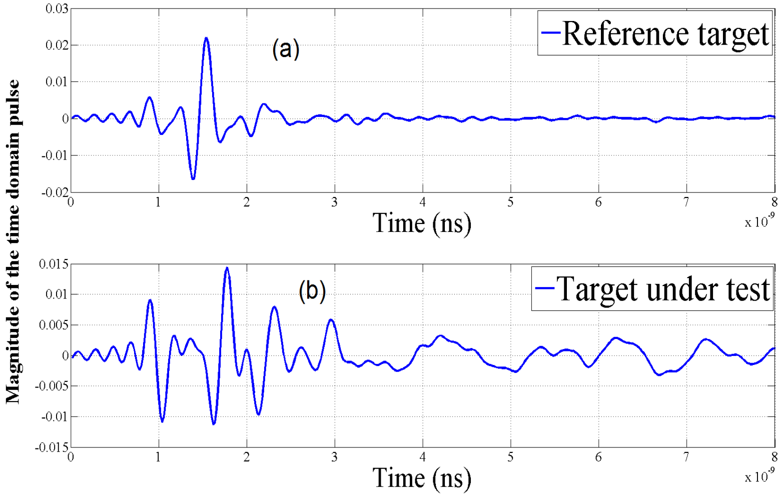

Figure 3.10: The difference in time between time domain responses: a) free space and the RT b) free-space and TUT.

The correlation function $C_{r,i}$ considered here is the correlation between the response $V_{t;i(t)}$ at receiving antenna i and the reference response $V_{t;r(t+\Delta t)}$ at the same receiving antenna, where Δt corresponds to the time difference in the arrival for the round trip TRR and TTR. The image map demonstrates a good recognition of the target dimensions and position, as shown in Fig. 3.11.

3.4 Near-field image of a Dirac source

In a first instance, we will consider a set of points in the field of view as Dirac pulse sources. The received voltages for all Dirac sources for the 10 antennas are calculated from near fields by reciprocity. A Dirac source is placed at a known position near the middle of the WoT, as shown in Figure 3.12.

Imaging algorithm

The imaging algorithm inspired from positioning procedures [78] relies on correlations between the field calculated from the target and the fields from Dirac source pulses located all over the domain after adding a white noise. The target will be located where the correlation values are maximum.

Figure 3.13 shows the time-domain response of the target. The received pulse is computed from the response after an inverse Fourier transform. The

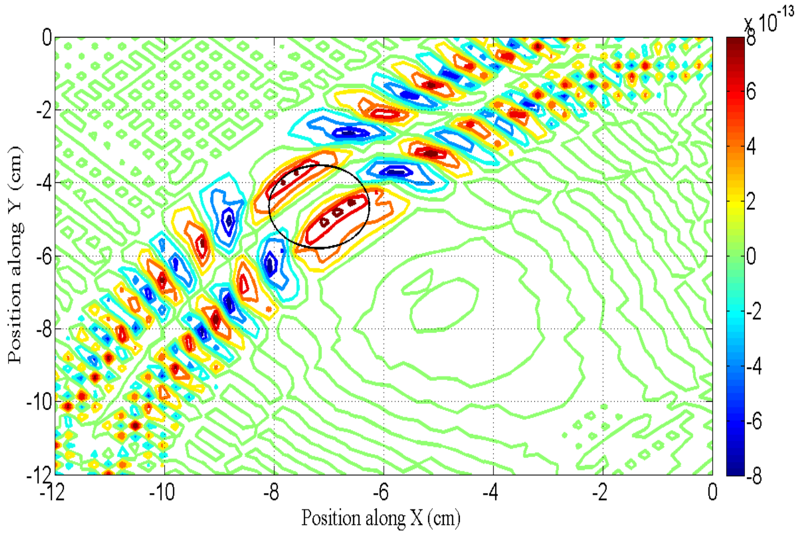

Figure 3.11: Image map obtained from measured responses.

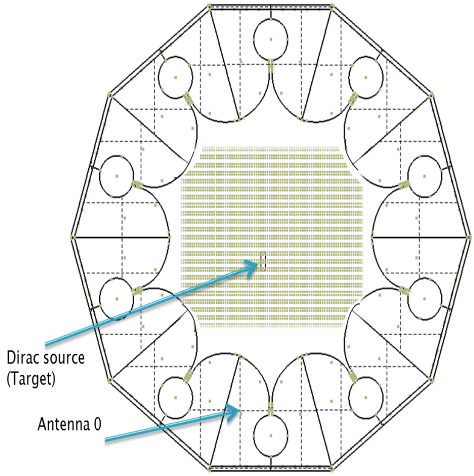

Figure 3.12: The geometrical position of the 2D screen and the target

obtained impulse duration is 0.4 nanosecond. This short duration is favorable to accurate localization and imaging. The function $c(n)$, expressed as

$$c(n) = T \otimes S = \sum_{m=0}^{N} T(m)S(m-n) \tag{3.3}$$

is the correlation between the time-domain response of the target $T(m)$ and a given calculated response $S(m)$ from a source in the field of view, to which

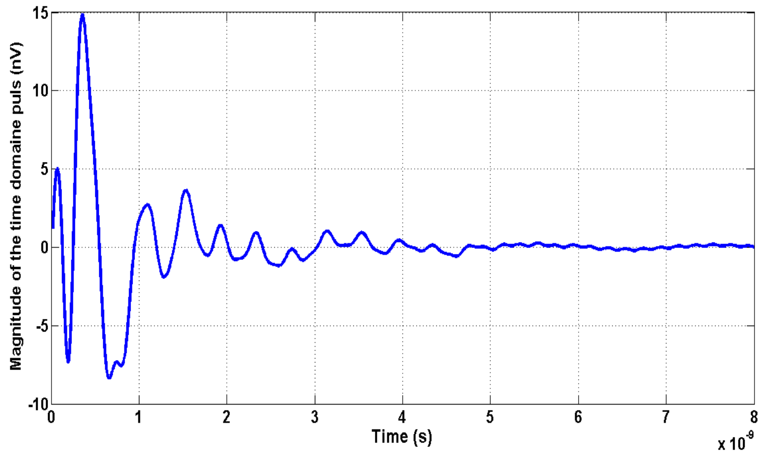

Figure 3.13: Impulse response obtained from inverse Fourier transform of the calculated near field. Transmit at antenna 0 and receive at antenna 1.

a random white noise has been added.

Figure 3.14 shows the initial map obtained after production of every possible position of the source in the area of radiation exposure. The initial map shows a good reconstruction of the target position, where the real target position is shown as a dark rectangle.

3.5 Distinguishing between metal cylinders

Two metallic cylinders with different diameters (5 and 10 cm) were used in the trials. Three ports (antennas 1, 2, 3) have been used in the measurements. Figure 3.15 shows the measurement setup.

First, each cylinder imaged with the WoT has been simulated using the Array Scanning Method (ASM) [48]. Figure 3.16 shows the reflection coefficients S11, S12 and S13 in the scenario where 3 ports are used, and presents the comparison between simulation and measurement. It is worth noting that the measurements have been taken without fine array calibration. It can be seen that the difference between each pair of curves (simulation versus measurement) for the metallic cylinder of 5 cm and the metallic cylinder of 10 cm is clearly noticeable. This difference enables us to distinguish between two different targets in the area of radiation exposure. To get an idea of the resolution versus diameter, another metallic cylinder, with 8 cm diameter, is considered in the simulation. Figure 3.17 shows the evolution of scattering parameters

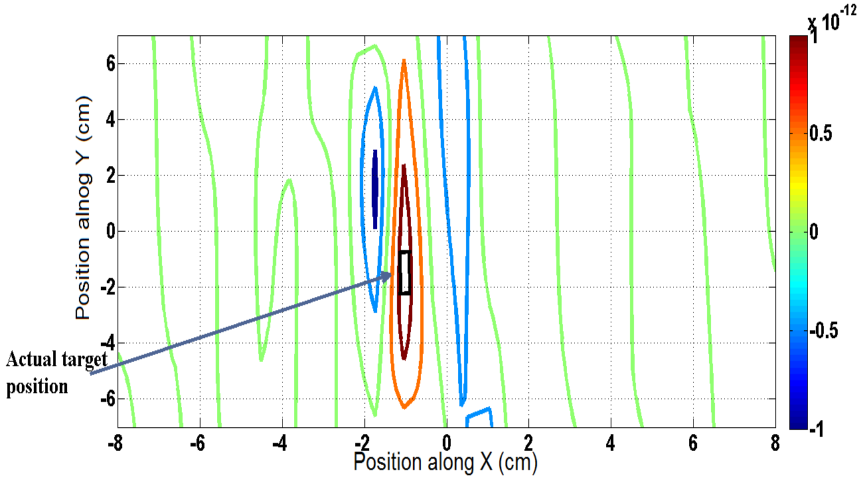

Figure 3.14: Map obtained from simulations when antenna 0 is excited for the frequency band 0.5-5 GHz.

versus cylinder diameter. The resolution in terms of cylinder diameter detection has been defined through a standard deviation criterion. The standard deviation has been calculated as:

$$\sigma = \sqrt{\frac{1}{N-1}\sum_{i=1}^{N}(x_i - \overline{x})^2}.$$

where N is the number of samples, $x_i = S_{measurement}/S_{simulation}$ and $\overline{x}$ is the average. The calculated values for $\sigma_{m5s5} = \sigma_{measurement-simulation}$ regarding S11, S12 and S13 for the cylinder of 5 cm diameter are 0.38, 0.2 and 0.31, respectively. The calculated values for $\sigma_{s5s8} = \sigma_{simulation5cm-simulation8cm}$ regarding S11, S12 and S13 are 0.91, 0.67 and 0.75, respectively. The standard deviation shows that the measurement results are much closer to simulation results for the case of cylinder 5 cm, than they are to simulation of cylinder 8 cm diameter. Since the diameter difference between cylinders is 3 cm, and the standard deviation $\sigma_{s5s8} \approx 3 * \sigma_{m5s5}$, 1 cm resolution in terms of diameter is estimated.

3.6 Imaging dielectric targets

This work has been done in collaboration with Dr. Augustin Cosse and Prof. Benoit Macq who developed the imaging algorithm. To move one step further towards future applications, we are interested in studying the signals obtained

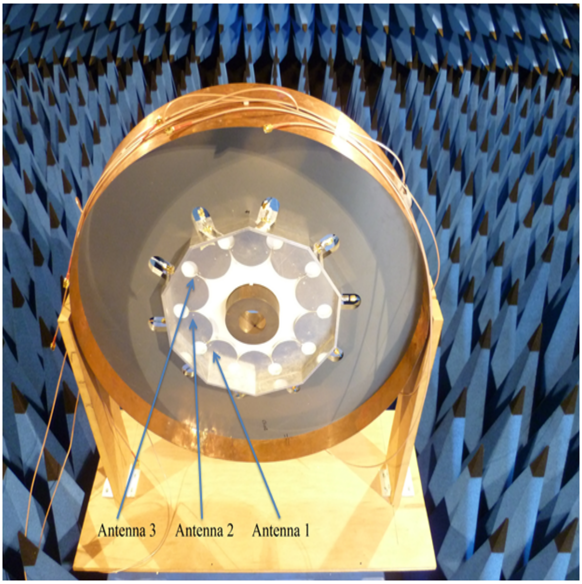

Figure 3.15: The measurement setup

when placing a dielectric material of relative permittivity $\varepsilon_r = 4$ at the center of the WoT. The configuration as well as an example of the obtained reflection coefficients for pairs of antennas are given in Fig. 3.18 and 3.19 (Top).

The dielectric cylinder is placed in the middle of the Wheel of Time, surrounded by vacuum. The sources of radiation are represented by small rectangles on top of each metallic plate's empty space (see green crosses in Fig. 3.18). Those rectangles are also used to set the positions of the simplified point sources used in the reconstruction.

By roughly following the guidelines of the reconstruction methods introduced in [80] (frequency domain) and [81] (time domain), we can already obtain the signals

$$T_{\varepsilon}(x,\ y) = \sum_m \sum_n \Gamma(\phi_n, f_m) \exp(2j\gamma_m \|\boldsymbol{x} - \boldsymbol{x}_n\|)$$

$$T_{\varepsilon_0}(x,\ y) = \sum_m \sum_n \Gamma_0(\phi_n, f_m) \exp(2j\gamma_m \|\boldsymbol{x} - \boldsymbol{x}_n\|)$$

where

$$\Gamma(\phi_n, f_m) = 20\log(|Z(\phi, f)|) / \max_f |20\log(|Z(\phi, f)|)|$$

$$\Gamma_0(\phi_n, f_m) = 20\log(|Z_0(\phi, f)|) / \max_f |20\log(|Z_0(\phi, f)|)|$$

are respectively the normalized reflection coefficients obtained from the interaction impedances $Z(\phi_n, f) = Z_{\phi_n,\phi_{n+1}}(f)$ between two adjacent antennas, for 9 antennas (angular positions $\phi_1, \ldots, \phi_N$) with and without the dielectric cylinder. We only use 9 angles to allow for the possibility to use adjacent antennas, the first one being used as transmitter, the second as receiver. $\gamma = \gamma(f_m) = 2\pi f_m \sqrt{\varepsilon_r}/c$ are the assumed propagation constants inside the Wheel of Time. Assuming no object at all we set the relative permittivity to $\varepsilon_r = 1$. This rough approximation will most likely constitute a source of error in the reconstructed cylinder (see Fig. 3.19). Finally, $\boldsymbol{x}$ is used to denote the pair (x, y), where $\boldsymbol{x}_n$ is the spatial position of the antenna associated with angular position ϕ_n. We consider 30 frequencies ranging from 1.8 to 2.1 GHz around the resonant frequency (2 GHz). According to [80], the two signals T_ε and T_{ε_0} can be considered as a representation of a probability distribution for the position of the target. Hence, by subtracting T_{ε_0} from T_ε we should be able to get a first estimation of the target position. The result obtained is given in Fig. 3.19. The image center corresponds to the dielectric center. We clearly recover a higher intensity in the middle of the Wheel of Time. As explained in Fig. 3.18, the point sources used in the reconstruction are denoted by green crosses and have been placed mid-angle between the transmitter and the receiver. The dielectric boundary is represented as a black line.

3.7 Conclusion

In this chapter, we used the WoT prototype, which has been designed and fabricated in previous chapters, to obtain preliminary images of metallic and dielectric targets. Various reconstruction algorithms are used to provide those images and localize the targets. The mutual coupling phenomenon between the WoT elements is briefly discussed. The near-field homogeneity with a 12 dB variation has been tested over the area of exposure, which is a necessary condition for near-field imaging based on delay-and-sum or interferometric methods. Time-domain responses have been processed in order to provide an initial image and locate small targets. The image map indicates that the algorithm successfully finds the target under test. A precise calibration procedure and a more advanced imaging algorithm will be developed to allow the study of more complex targets. Dirac pulse sources have been positioned in the middle of the field of view. In order to localize small sources, correlation products have been processed. An initial near-field image of a Dirac source has been obtained with a basic target recognition. Good comparisons are obtained between Method-of-Moments simulations and measurements in the presence of metallic targets. The detection of various metallic cylinders is discussed experimentally and numerically. In order to get closer to possible future applications, preliminary imaging results have been obtained for a simple dielectric cylinder of relative permittivity $\varepsilon_r = 4$. Future work will consist of developing more advanced algorithms that include a deeper analysis of scattering by the antennas, as well as an extension to more complicated geometries and central positions of the target.

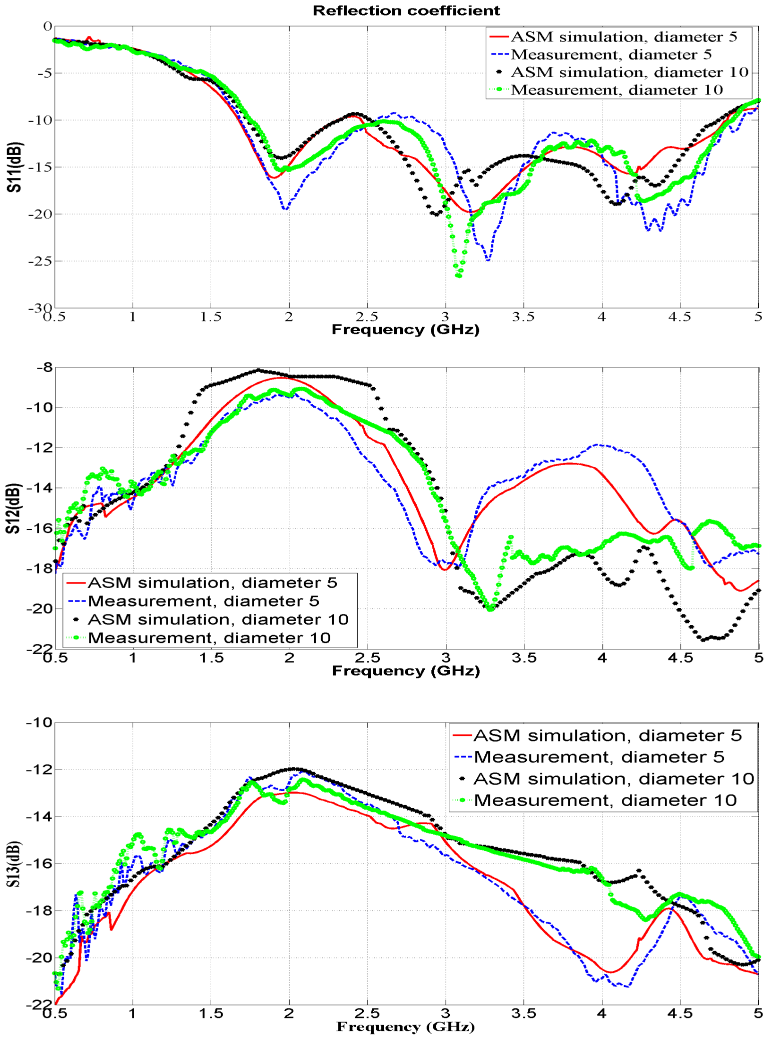

Figure 3.16: S11, S12 and S13 comparisons between ASM simulation and measurements respectively

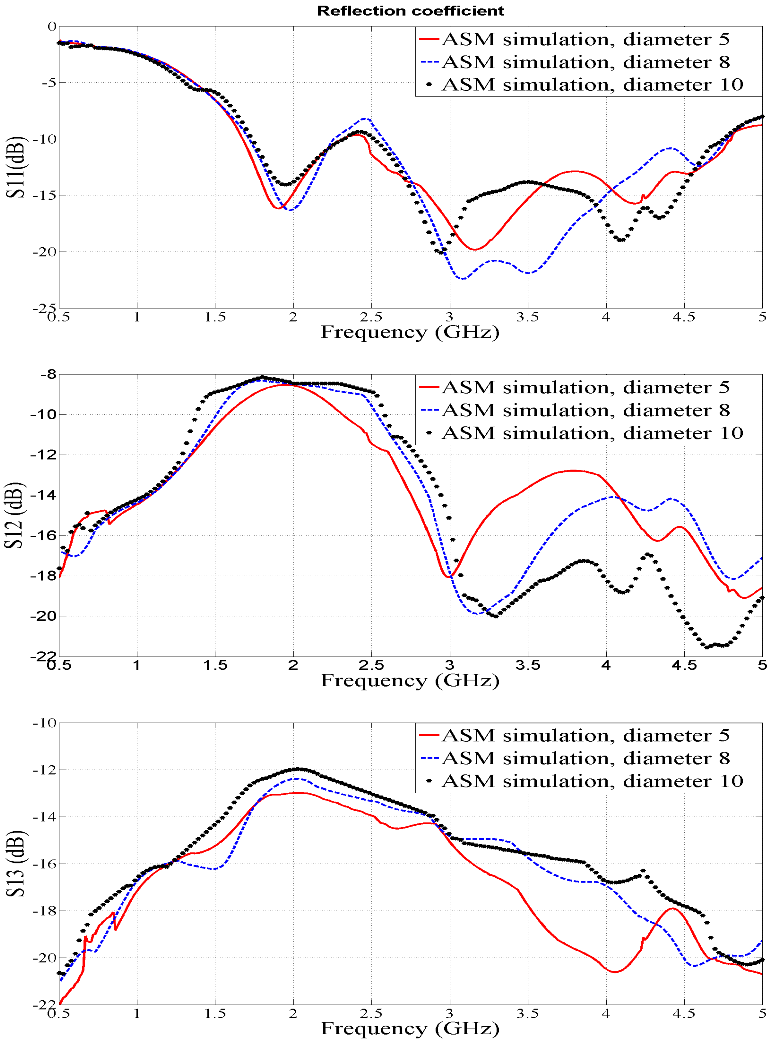

Figure 3.17: S11, S12 and S13 ASM simulation for various metallic cylinders

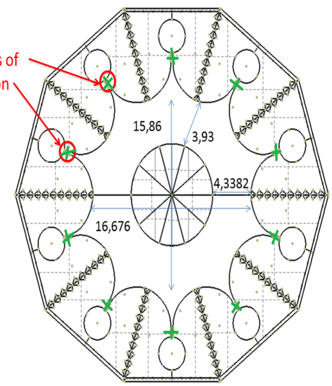

Figure 3.18: Setup geometry for imaging of the dielectric.

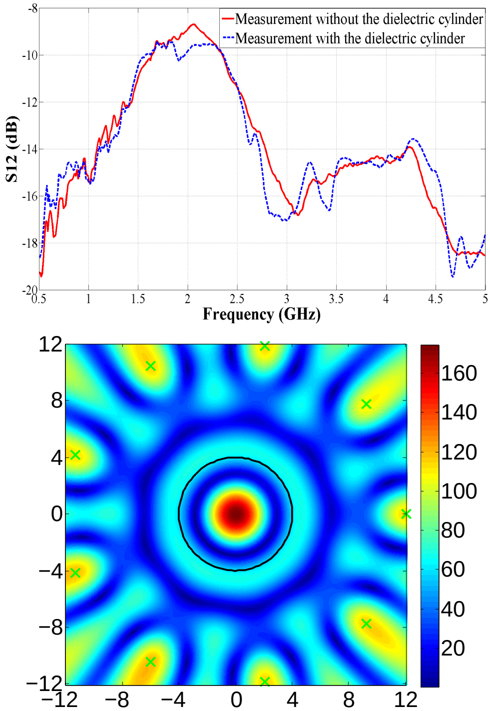

Figure 3.19: (Top), S12 Reflection coefficient obtained for 401 frequencies ranging from 0.5 to 5 GHz. Note that the discrepancy between the measurements with and without dielectric is the highest around the resonant frequency (2GHz). (Bottom), Result obtained by substracting the two intensity signals T_ε and T_{ε_0} induced by the reflection coefficients measured with or without the cylindrical dielectric material.

UWB Vivaldi Antenna for Water Leak Detection

4

This chapter deals with the design of Vivaldi antennas with modified shape for water leak detection applications. For this type of applications, the antenna needs to cover the UWB bandwidth, where the low frequencies penetrate deeper into the ground and high frequencies provide high resolution for image reconstruction. Low frequency antenna design is challenging due to the expected large dimensions of the radiator. A 3-D metallic Vivaldi antenna is proposed to cover the bandwidth between 200 and 2500 MHz. We took as an objective to minimize the antenna weight by introducing holes at specific positions related to the current distributions. Near-fields in E and H planes in the front of the antenna are depicted and display smooth spreading over a sufficiently narrow area of radiation exposure. The impact of the ground on the antenna is briefly analyzed, while in Chapter 5 a fast numerical method is developed to include the effect of the ground. The complete design of a linear array of 4 elements is presented, and the mutual coupling between elements is illustrated. A single 3-D Vivaldi antenna has been manufactured and measured at the WELCOME facility of UCL, with very good agreement between measurement and simulation.

4.1 Introduction

Leaks happen to be a major source of wasted water, with important financial impact. The European Environment Agency (EEA) estimates that for the domestic sector only 80% of water consumption is actually used; whereas the other 20% is returned to the aquatic environment through leaks in the distribution network and through wastewater [49]. Currently, one of the major challenges is detection of fluid loss due to leakage from underground distribution pipes [50]. Such detection can be carried out with the help of ground penetrating radar. This was the subject of a project led by Prof. Sebastien Lambot from the UCL's Earth and Life Institute, Georadar Research Center (GPR Louvain).

The large bandwidth of GPR antennas is very important for this type of applications. The trade-off between investigating at greater depth by lower frequency waves and achieving good spatial resolution using the high-frequency part of spectrum leads to an optimal frequency band, from a few hundreds of MHz to a few GHz [51]. Hence, the choice of the appropriate antenna depends on the precise project goals. For water leak detection applications, two double-ridged horn [52] and bowtie [53] antennas are mostly used. Antipodal Vivaldi antennas are reported for water pipe sensor and telemetry [54].

In general, an antenna is best defined in free space. The presence of an object like ground near the antenna will modify its performance. The antenna impedance is considerably affected by the lossy earth, especially at lower and medium frequencies [**?**]. The Vivaldi antenna [8][55], which is a special type of Tapered-Slot Antenna (TSA), is widely used for wideband applications due to its ultra-wide bandwidth, simple structure and easy fabrication. The design goal of this chapter it to design a Vivaldi antenna devoted to water leak detection. The major challenge is the low-frequency limit, where it is required to provide a compact and minimum size for the Vivaldi antenna with a low frequency cut-off at 200 MHz. The main objective of the project is to detect the underground water leak, so the UWB antenna is exposed to face nearby medium. The holographic technique, invented in 1947 by Gabor [60] while working to improve the resolution of an electron microscope, has other applications at microwave frequencies. The microwave holography [61], in the context of antennas, is an effective method of recording and reproduction the wave reflected from a nearby object [62].

This chapter is organized as follows. The design of an isolated 3-D Vivaldi antenna is provided in Section 4.2, as well as simulation results. Section 4.3 presents the study of UWB near-field radiation. Section 4.5 presents the UWB Vivaldi prototype. Section 4.4 discusses the effect of the ground on the reflection coefficient of the antenna. Section 4.6 presents the full design of a 3-D linear Vivaldi antennas array. The array data can provide more information about the medium, where in some cases the information collected from a single element is insufficient to reconstruct multiple layers [56]. Conclusions are drawn in Section 4.7.

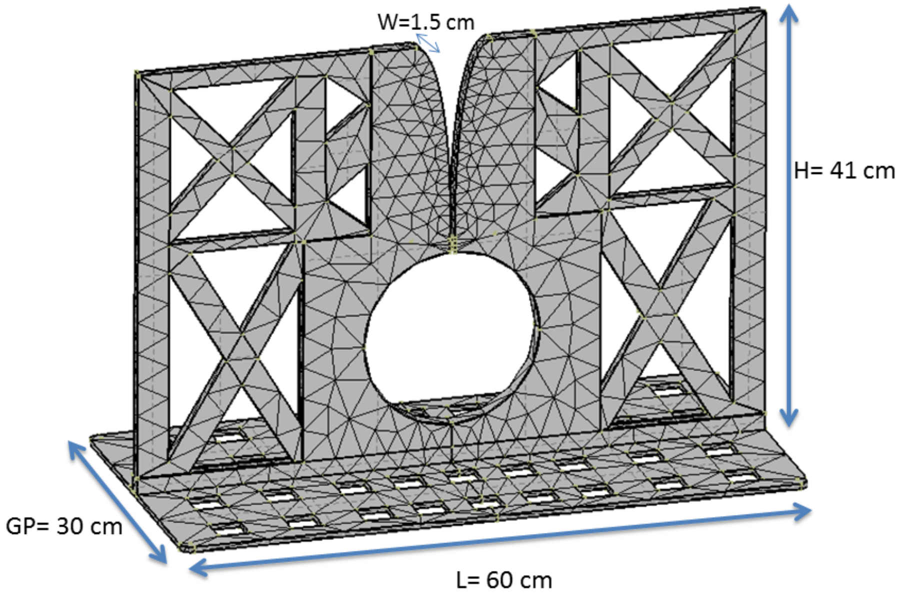

Figure 4.1: Layout of the 3-D Vivaldi antenna.

4.2 Design of an isolated 3-D Vivaldi antenna

An electromagnetic simulation software (MOM3D) developed at UCL and based on the Method of Moments is used to simulate the different structures. This antenna is designed and meshed using the freely available GMSH software [41]. Following the optimization carried out in Section 2.2.3, a proposed design of 3-D Vivaldi antenna is presented in Fig. 4.1. The antenna dimensions are $60\times41\times1.5$ cm, and the type of taper profile is elliptical [57]. Triangular and rectangular holes are made in the antenna body to make it lighter. These holes are chosen in specific positions, where the current distribution flows in low density. Fig. 4.2 presents the current distribution over the Vivaldi antenna, where the low current density is represented in blue color. The taper profile is the main responsible of antenna radiation, that the reason no holes are added nearby the elliptical taper profile and the circular cavity. The effect of adding these holes is presented in Fig. 4.3.

It is recommended to affix a ground plane beneath the antenna to hold the antenna properly, and to improve the isolation between the feeding port and the antenna body. The thickness of the antenna is chosen to 5 mm for the optimized behavior [58]. The effect of adding the ground plane mainly appears

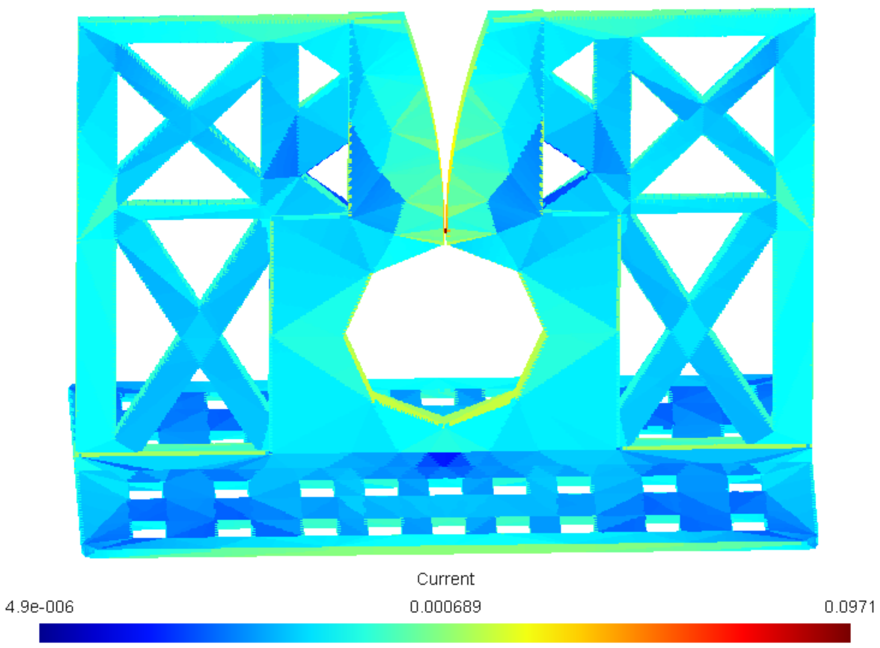

Figure 4.2: Current distribution at 2 GHz.

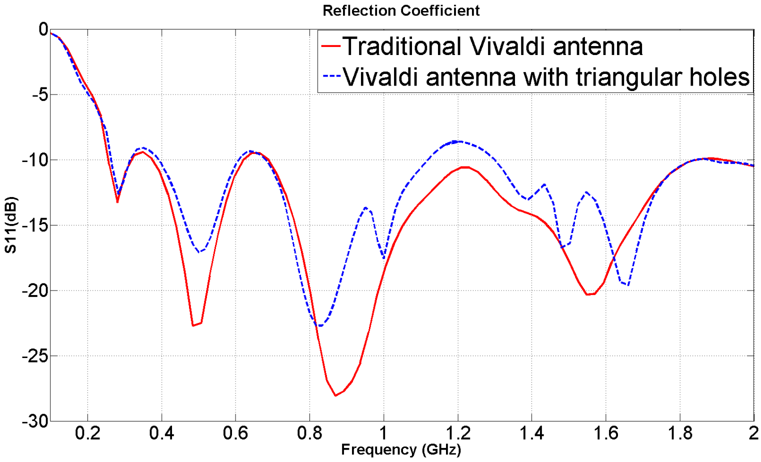

Figure 4.3: The effect of adding the triangular holes.

at lower frequencies, as shown in Fig. 4.4. To make the ground plane lighter, square holes are created. This prototype was fabricated from Aluminum. The antenna model has been also analyzed using the CST Microwave Studio software [59]. Fig. 4.5 compares simulation results for the magnitude of the reflec-

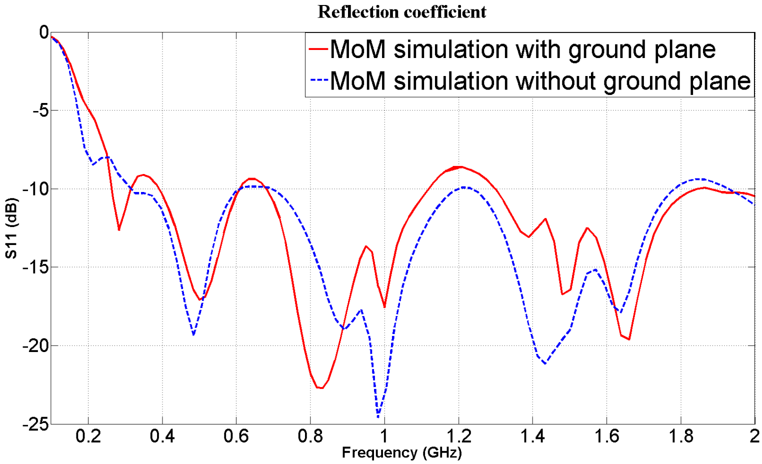

Figure 4.4: Effect of adding the ground plane on the reflection coefficient.

tion coefficient between MOM3D and CST Microwave Studio, with reference to 50 Ω. Fig. 4.5 shows a very good agreement between those obtained from MoM3D and CST simulations. The small differences between the simulations is due to using two different mesh lengths. In MoM3D a coarse mesh has been used to be able to simulate the structure in brute-force solution, while in CST simulation it has been used an average mesh.

For the presented antenna, the simulation results exhibit a bandwidth from 0.25 GHz to 2 GHz with respect to a -10 dB criterion, and from 0.2 GHz with respect to a -5 dB criterion for the antenna reflection coefficient. It is worth checking the directivity by plotting the radiation patterns in the E-plane. Fig. 4.6 shows that the directivity increases with frequency.

4.3 UWB near-field radiation study

To know more about the near-field sensitivity, a 2D rectangular screen of testing functions is created in the front of the antenna, as shown in Fig. 4.7. The dimension of the 2D screen is 84 cm by 42 cm.

Fig. 4.8 shows an example of near-field radiation in the E and H-planes at 200 MHz. X and Y indices (a grid of 54×41 lines) refer to the 2D screen testing function points. A relatively homogeneous response ($<$ 25 dB variation) has been obtained over the whole field of view, which is a satisfactory condition for near-field imaging. A smooth near-field shape in the area of radiation exposure is depicted at 200 MHz.

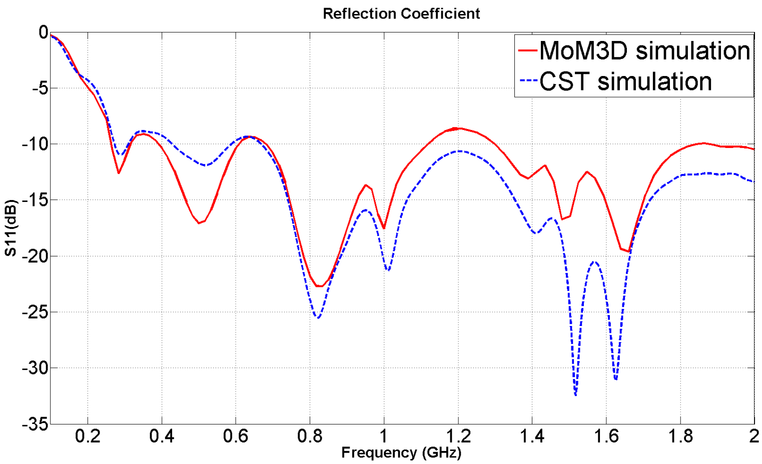

Figure 4.5: Comparison between the reflection coefficient obtained from simulations with MoM3D and CST.

4.4 The contribution of the ground on the antenna

As an approximation, we assume a large cube of ground as a semi-infinite ground, as shown in the configuration simulated with the CST Microwave Studio software (Fig. 4.9). Dry and wet sandy soils are chosen as materials with relative permittivities $\varepsilon_r = 2.53$, tanδ = 0.0036 and $\varepsilon_r = 13$, tanδ = 0.29 respectively [59]. The distance between the antenna and ground is set to 5 cm.

The effect of ground appears mainly at the low frequencies as shown in Fig. 4.10. At low frequencies (long wavelength), the presence of very nearby ground as a lossy medium increases the losses through a stong antenna-ground coupling. An increase in dB is observed around 200 MHz, whereas a decrease in dB is noticed around 350 MHz for the antenna's reflection coefficient. One can observe more ripples and higher loss in the case of wet sandy soil at lower frequencies, which give us a warning to avoid doing the measurement on a rainy day. This oscillatory behavior of reflection coefficient versus frequency makes so difficult to conclude about possible improvement or degradation in presence of ground.

4.5 3-D Vivaldi antenna prototype

The 3-D Vivaldi antenna was manufactured and measured at WELCOME facility at UCL university. The antenna is made from Aluminum, as shown in

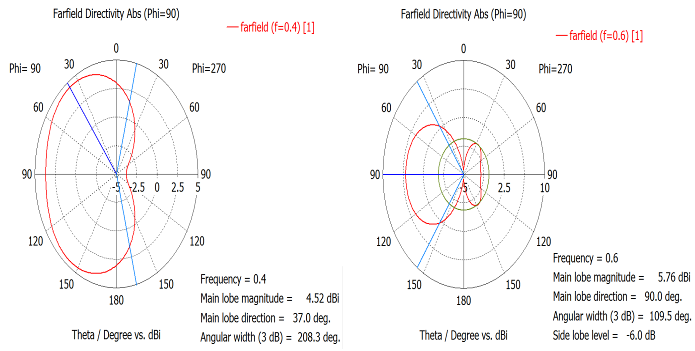

Figure 4.6: CST simulations of radiation patterns at 0.4 GHZ and 0.6 GHz successively.

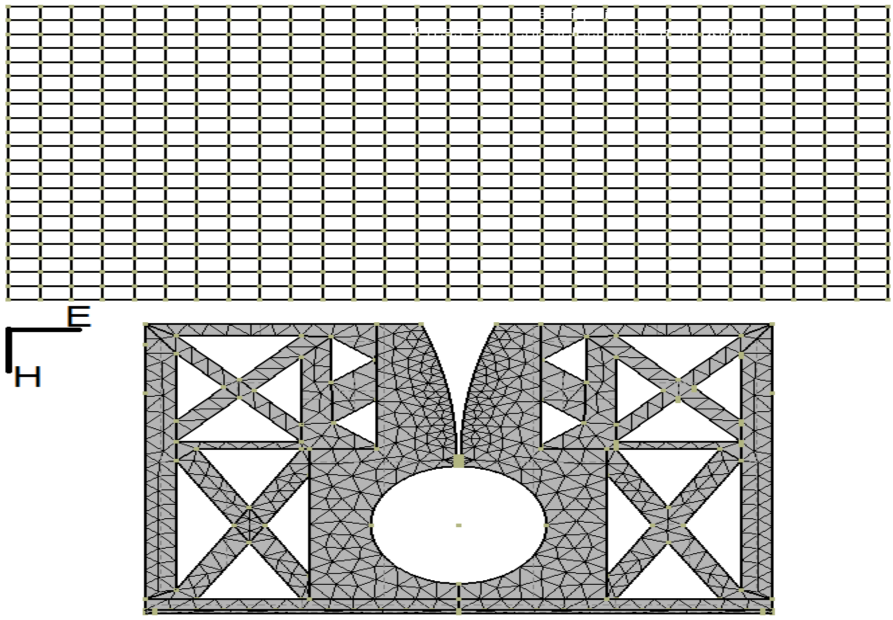

Figure 4.7: The geometric position of the antenna and the 2D screen.

Fig. 4.11. The antenna weight is about 5 kg. A good agreement between measurement and simulations is achieved in terms of the reflection coefficient, where a bandwidth from 250 MHz to 2 GHz is obtained (Fig. 4.12). The CST software simulation appears to be slightly better than the MoM simulation due to using a coarse mesh in MoM simulation to be able to simulate the structure in brute-force solution.

Lambot et al. [64] proposed a radar model valid in far-field conditions. The model takes antenna effects as well as the antenna-medium coupling into ac-

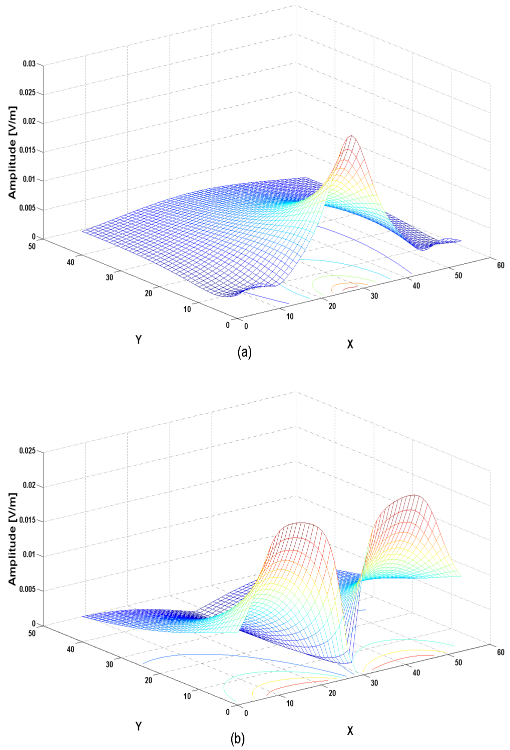

Figure 4.8: Amplitude (V/m) of the equivalent field distribution in the (a) E and (b) H-directions at 200 MHz, respectively.

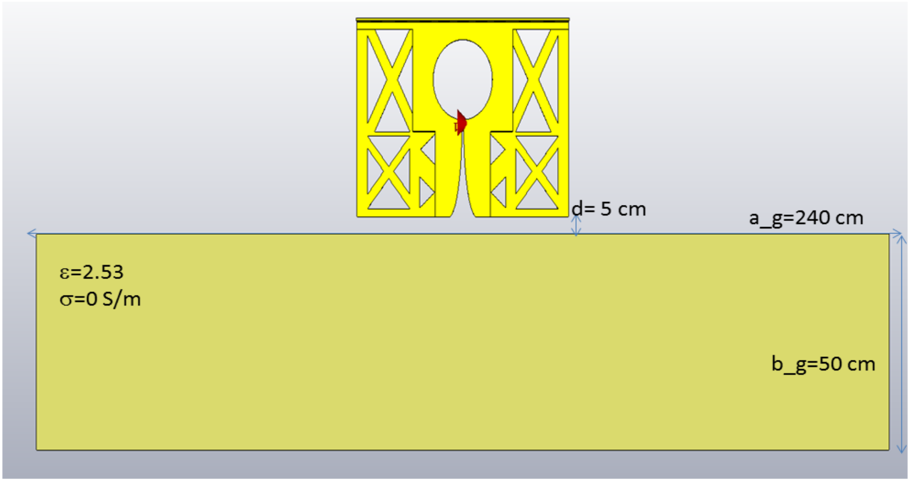

Figure 4.9: The geometric position of the antenna and semi-infinite ground.

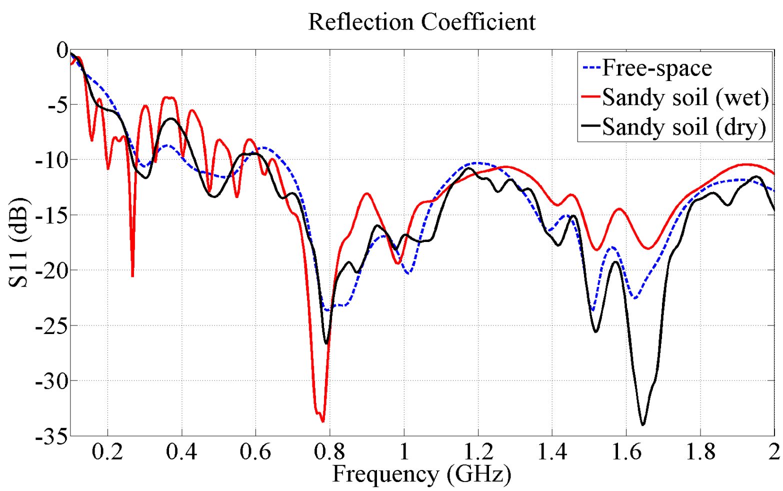

Figure 4.10: The impact of ground on the measurement.

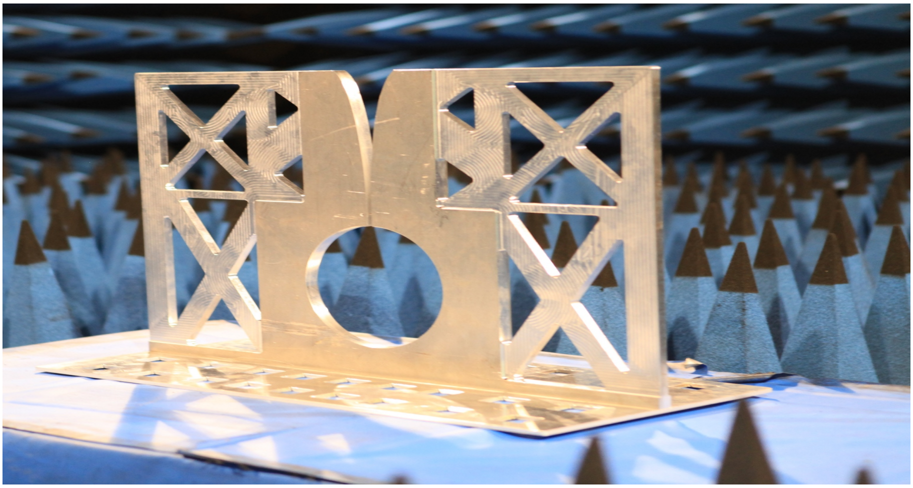

Figure 4.11: The 3-D Vivaldi antenna prototype.

count through an intrinsic representation based on characteristic global reflection and transmission coefficients of the antenna. More recently, the model was generalized to near-field conditions to quantify the medium electrical properties using full-wave inverse modeling [65]. Preliminary tests were conducted in the Hydrogeophysics Laboratory to test the prototype. Frequency-domain measurements were performed with the Vivaldi antenna placed at 77.5, 87, 96.7 and 106.8 cm from a large copper sheet. The antenna effects removal which is based on the far-field model developed by Lambot et al. is applied. The results after the filtering of the antenna effects show clear reflec-

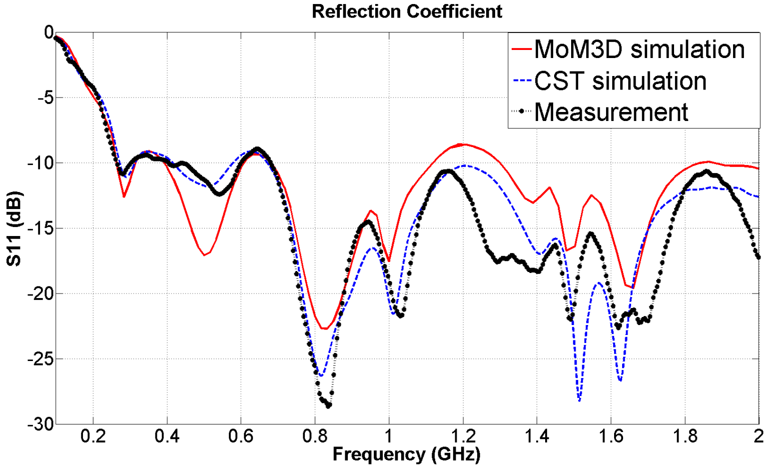

Figure 4.12: The comparison between measurement and simulation for the 3-D Vivaldi antenna.

tions coming from the PEC, whatever is the distance between the antenna and the copper sheet (PEC). The prototype seems to be efficient from 0.25 GHz to 2.5 GHz to apply for water leak detection. The frequencies higher than 2.5 GHz seem to have an issue in image reconstruction, where high frequencies do not couple perfectly with the ground as they are emitted from the antenna at a larger distance (closer from the feed point).

4.6 3-D linear Vivaldi antennas array

In most applications, the single element suffers from a lack of collected data for multiple layers cases. The design of antenna array systems enhances the simultaneously recording of a large amount of data in a single measurement. Numerical experiments showed that four antennas were sufficient to obtain enough information, given the larger propogation distance through the ground, so four Vivaldi antennas are arranged in a linear array as shown in Fig. 4.13. CST Microwave Studio [59] simulation results point out the mutual coupling effect around the half wavelength resonance frequency (250 MHz). Although the four antenna elements are similar, the reflection coefficients S_11, S_44 differ from those S_22, S_33 due to the fact that antennas 2 and 3 are exposed to radiation from both sides. For example, antenna 2 is exposed to radiation mainly from antennas 1 and 3, and 4 to a smaller extent, whereas antenna 1 is exposed to scattering from just antenna 2. It is clear that mutual coupling

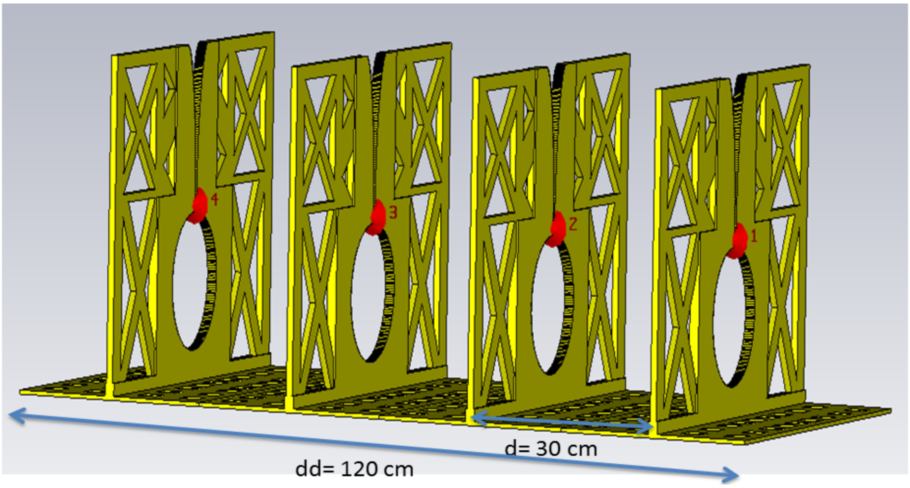

Figure 4.13: 3-D linear Vivaldi antenna array layout.

strongly affects the radiation properties of the array through a variation in the input impedance (see Fig. 4.14).

4.7 Conclusion

We presented the design and simulation of a UWB Vivaldi antenna for water leak detection. The antenna dimensions are 60×41×1.5 cm. The antenna achieves satisfactory radiation performance over the bandwidth from 0.25 GHz to 3.5 GHz with respect to a -10 dB criterion. A relatively homogeneous (< 25 dB variation) response has been obtained over the whole field of view. The simulation results obtained with the commercial software CST show that the effect of ground on the reflection coefficient of the ground-antenna system appears mainly at low frequencies. A remarkable effect is noticed on the antenna impedance at low frequencies through rapid oscillations. A UWB Vivaldi antenna prototype is fabricated and measured in the UCL facilities. The comparison between measurement and simulations is very satisfactory in terms of reflection coefficient. A more efficient way to account for the effects of the ground will be presented in Chapter 6. The results obtained from testing the Vivaldi prototype by Prof. Lambot's team do not encourage using the Vivaldi antennas for water leak detection where high resolution is needed, due to mismatching between the antenna and the ground at high frequency waves. It is recommended either to lower the antenna profile or using bowtie antennas to better match the high frequencies with the ground. The fabricated

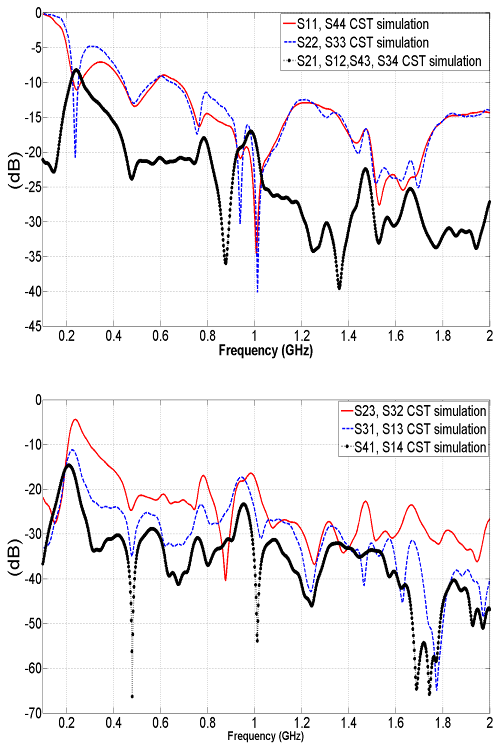

Figure 4.14: Reflection and transmission coefficients of antenna array elements.

prototype could be used to analyze the quality of road pavement.

Acknowledgment

This work is funded by the Région Wallonne through the SENSPORT project.

Efficient MoM Simulation of 3D Antennas in the Vicinity of the Ground *

5

* Adapted from "K. Alkhalifeh, G. Hislope, N. A. Ozdemir, C. Craeye, Efficient MoM Simulation of 3-D Antennas in the vicinity of the Ground, IEEE Trans. Antennas Propag. vol. 64, no. 12, pp. 5335-5344, Dec. 2016."

5.1 Introduction

Ground penetrating radar (GPR) is currently the subject of intensive research for various applications such as investigation of soil, e.g. for agriculture [82]-[83]-[84], road pavement verification [85][86], water leak detection [87][88] and ground dielectric permittivity estimation [89]-[91]. For such applications, the antenna is very close to an object, such as the lossy ground, which will strongly modify the antenna input impedance [42] and radiated near-fields. Such applications require the antenna(s) to be intensively simulated for a wide range of ground types (permittivity, conductivity, permeability, multilayered medium, etc.). Such simulations may help identifying the best antenna type for given average ground properties. When the layered medium corresponds to an acceptable approximation below the antenna footprint, such simulations may also assist the estimation of the layers properties. Indeed, the active antenna will be expected to collect data from a large number of prospective ground types with various parameters. Structures composed of a radiator and a layered medium can be analyzed via full-wave frequency-domain integral equation techniques discretized and solved using the Method of Moments (MoM) [16]. Pantoja et al. [20] extended the MoM for the transient analysis of thin-wire antennas located over a lossy half-space, directly in the time domain. When the antennas was not too close to a half-space medium, good results were achieved. The Surface Integral Equation (SIE) approach has been used for the analysis of antennas [93]-[94], where the Dyadic Green's function for Layered Media (DGLM) is employed to take into account the effect of the dielectric material [95]-[98]. In [99], the authors used a method based on the hybrid Volume-Surface Integral Equation (VSIE). The modeling of antennas and medium together has been investigated by different authors. Cui and Chew [100], developed an accurate model for wire antennas, above or inside the ground using Galerkin testing. A 3-D model based on the finite-difference time-domain (FDTD) method has been developed by Giannopoulos (GPRMax [13]) to simulate GPR antennas in the presence of dielectric material. Lambot et al. [64] developed a far-field antenna model to characterize planar layered media. The model accounts for the antenna effects through global transmission/reflection coefficients. The 3-D Green's function is used to simulate propagation over the layered medium. Lambot and André [65] generalized the far-field model so that it also applies to near-field conditions, and the model was successfully validated in laboratory conditions.

A new method, named Fast Ground Coupling Matrix (FGCM) is proposed here to account for the interaction between antennas and a ground composed of arbitrary layers. In this work, 3-D metallic antennas are chosen as examples. The FGCM method relies on the MoM solution of surface integral equations to solve the electromagnetic problem that involves metallic antennas radiating above a planar, possibly layered, ground. The proposed method starts by separating the MoM matrix into two terms: a free-space matrix Z^f and a matrix Z^g that accounts for the presence of the ground. Such separation can be found in [100] in the case of flat substrates, and in [101] for cylindrical substrates. The free-space matrix is calculated using the brute-force MoM approach; it can be efficiently interpolated versus frequency using the FMIR-MoM [102]. The ground reflection matrix Z^g is calculated as a product of radiation patterns of the basis/testing functions with the ground's reflection coefficient, integrated following a specific path along the complex spectral coordinates (k_x, k_y). Here, the steepest-descent path (SDP) [103] is considered. The radiation patterns of the basis/testing functions depend on the (k_x, k_y) coordinates. A grid with a minimal number of points is achieved by explicitly compensating aliasing and truncation errors, as done in [104] in the 2D case. The independence of the ground physical and electromagnetic parameters when generating the radiation patterns allows the efficient calculation of the MoM impedance matrix that describes the coupling between antenna and ground. The operations needed to update the MoM impedance matrix after changing the ground parameters consists of uploading the off-line free-space matrix Z^f and off-line basis/testing functions radiation patterns, and performing the efficient calculation of the reflection coefficient versus (k_x, k_y). The latter two operations allow the fast calculation of the ground coupling impedance matrix Z^g. Following [104], the number of points in the (k_x, k_y) plane is strongly reduced based on a systematic compensation between aliasing and truncation errors. The significant advantage of this technique is that it only needs once the calculation of Z^f and of the radiation patterns of the basis/testing functions once, and then a very efficient calculation of the MoM impedance matrix is achieved for given ground parameters. The FGCM method is able to simulate the antenna response for any soil parameters (permittivity, conductivity, permeability, etc.), including multi-layered media. The MoM impedance matrix is also efficiently updated when changing the vertical distance between the antenna and the ground by multiplying the reflection coefficient with a factor. A limitation of this method is that it requires the antenna to be entirely above the ground. Also, the FGCM method does not speed up the matrix solution step, which could be done using the Macro Basis Functions (MBF) approach [105] [106]. Preliminary simulation results of the proposed method are reported in [107], while this chapter presents full details of the method, as well as validations using FDTD simulation and measurements.

The remainder of this chapter is organized as follows: Section 5.2 presents the detailed mathematical formulation of the FGCM method. In Section 5.3, numerical results obtained employing the FGCM method are validated with respect to the brute-force MoM approach, IE3D and SEMCAD commercial software. The computation times for the proposed method are also reported in this section. In Section 5.4, the obtained numerical results are validated with respect to measurements and the performance of the method is discussed. Finally, conclusions are drawn in Section 5.5.

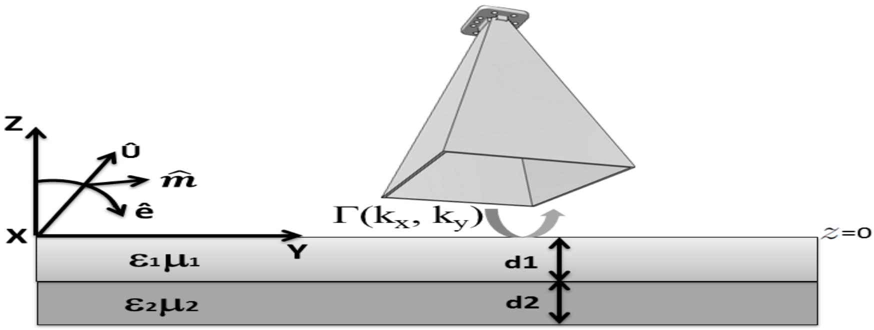

Figure 5.1: Coordinates of a radiator above a multilayered medium.

5.2 MATHEMATICAL FORMULATION

5.2.1 TE and TM waves

Consider sources above a mutilayered medium, excited by known electric and magnetic currents, as illustrated in Fig. 5.1. The fields above $z = 0$ can be decomposed into TE and TM plane waves associated with spectral coordinates (k_x, k_y). Those plane waves are expressed as follows:

$$\vec{E} = (-\hat{m}\, A_{TE} + \hat{e}\, A_{TM})\; e^{-jk_x x}\, e^{-jk_y y}\, e^{\pm jk_z z} \tag{5.1}$$

$$\vec{H} = \frac{1}{\eta}\; (\hat{e}\, A_{TE} + \hat{m}\, A_{TM})\, e^{-jk_x x}\, e^{-jk_y y}\, e^{\pm jk_z z} \tag{5.2}$$

where, in the exponent along z, the $\mp$ sign corresponds to electromagnetic waves propagating in the $\pm z$ direction, and A is the complex amplitude of the plane wave. The free-space impedance is denoted by η. For a given spectral component (k_x, k_y), with magnitude $\beta = \sqrt{k_x^2 + k_y^2}$, propagation takes place in direction $\vec{k} = (k_x, k_y, \mp k_z)$ with

$$k_x^2 + k_y^2 + k_z^2 = k^2 = \omega^2 \epsilon_i \mu_i \tag{5.3}$$

where ϵ_i and μ_i are the permittivity and permeability of the i^{th} layer in the medium [108]. The sign of k_z is chosen such that $\mathrm{Im} k_z < 0$. The normalized direction of propagation is $\hat{u} = \vec{k}/k$. In each medium, horizontal and vertical polarization vectors are defined by vectors perpendicular to the direction of propagation for waves propagating in $+z$ direction:

$$\hat{m} = \frac{1}{\beta}\begin{bmatrix} -k_y \\ k_x \\ 0 \end{bmatrix} \qquad \text{and} \qquad \hat{e}^u = \frac{1}{\beta\, k}\begin{bmatrix} k_x\, k_z \\ k_y\, k_z \\ -\beta^2 \end{bmatrix} \tag{5.4}$$

For waves propagating in $-z$ direction:

$$\hat{m} = \frac{1}{\beta}\begin{bmatrix} -k_y \\ k_x \\ 0 \end{bmatrix} \qquad \text{and} \qquad \hat{e}^d = \frac{1}{\beta\, k}\begin{bmatrix} -k_x\, k_z \\ -k_y\, k_z \\ -\beta^2 \end{bmatrix} \tag{5.5}$$

In the TM case, $\hat{e}_p$ is $\hat{e}^u$ or $\hat{e}^d$ (upwards and downwards, respectively); and in the TE case, $\hat{e}_p$ is $-\hat{m}$.

5.2.2 Electromagnetic fields reflected from ground

Consider the case of a three-dimensional antenna discretized with Basis Functions (BFs), and Testing Functions (TFs). In the following, Galerkin testing will be applied; i.e. the set of testing functions corresponds to the set of basis functions. We split the interaction matrix Z between these BFs and TFs into a free-space part Z^f and a ground-reflected part Z^g. A plane-wave spectrum approach with regular (k_x, k_y) spacing [109]-[111] is used to accelerate the calculation of the ground-reflected part. The Green's function reads as the Weyl integral [112]:

$$\begin{aligned} G(R) &= \frac{e^{-jkR}}{4\,\pi R} \\ &= \frac{1}{(2\,\pi)^2} \iint_{-\infty}^{+\infty} \frac{e^{-j\,(k_x\,(x-x')+k_y\,(y-y')+k_z\,|z-z'|)}}{2\,j\,k_z} dk_x\, dk_y \end{aligned} \tag{5.6}$$

where $\vec{r}\,' = (x', y', z')$ represents the source point coordinates, $\vec{r} = (x, y, z)$ represents the observation point coordinates, and $R = \| \vec{r} - \vec{r}\,' \|$.

The vector potential in free space due to electric current density $\vec{J}_b$ associated to a BF can be expressed as:

$$\vec{A}(x,\, y,\, z) = \iiint_V G(R)\, \vec{J}_b(x',\, y',\, z')\, dV \tag{5.7}$$

In (5.6), the integral over (k_x, k_y) coordinates corresponds to the spectral representation of the Green's function. For waves propagating in $-z$ direction, $|z - z'|$ can be rewritten as $z' - z$, such that $e^{-jk|z-z'|} = e^{jkz'}e^{-jkz}$ becomes separable. This chapter assumes that the antenna is entirely above the ground and calculates the ground's reflection component by simply multiplying each plane wave propagating in $-z$ direction by the ground's reflection coefficient. The relation between the electric field intensity with p polarization (either TE or TM) and the radiated vector potential is defined as:

$$\vec{E}_p = -jk\eta \ (\vec{A} + \frac{\nabla \nabla \cdot \vec{A}}{k^2})_p$$

$$= \frac{-j\,k\,\eta}{(2\,\pi)^2} \iint_{k_x,k_y} \hat{e}_p \frac{e^{-j\,(k_x\,x+k_y\,y-k_z\,z)}}{2\,jk_z} \ \hat{e}_p \cdot \tag{5.8}$$

$$\left\{\mathcal{I} - \frac{\bar{k}\bar{k}.}{k^2}\right\} \iiint \vec{J}_b \ e^{-j\,(k_x\,x'+k_y\,y'+k_z\,z')} \ dV \ \ dk_x\,dk_y$$

where integrations over spectral and spatial coordinates appearing in (5.6) and (5.7) have been swapped, and $\mathcal{I}$ is the identity operator. The electric field propagating in $-z$ direction $(z < z')$ with p polarization then becomes:

$$\vec{E}_p(x,y,z) = \frac{-j\,k\,\eta}{(2\,\pi)^2} \iint \hat{e}_p \ F_{b,p}(k_x,k_y) \ \frac{e^{-j\,(k_x\,x+k_y\,y-k_z\,z)}}{2\,j\,k_z} \ dk_x\,dk_y \tag{5.9}$$

where $F_{b,p}$ is the pattern of the corresponding basis function with p polarization; it is given by

$$F_{b,p}(k_x,k_y) = \iiint_V \vec{J}_b(x',y',z') \cdot \hat{e}_p \ e^{j\,(k_x\,x'+k_y\,y'-k_z\,z')} \ dV \tag{5.10}$$

The field reflected by the ground in the same polarization then becomes:

$$\vec{E}_p(x,\ y,\ z) = \frac{-j\,k\,\eta}{(2\,\pi)^2} \iint \hat{e}_p \ \Gamma_p(k_x,\ k_y)F_{b,p}(k_x,\ k_y)$$

$$\frac{e^{-j\,(k_x\,x+k_y\,y-k_z\,z)}}{2\,j\,k_z} \ dk_x\,dk_y \tag{5.11}$$

where Γ_p is the reflection coefficient for p polarization.

The electric field tested by function $\vec{J}_t$ reads

$$I = \iiint \vec{E}_p \ \cdot \vec{J}_t \ dV \tag{5.12}$$

Following a procedure similar to that used in (5.9), I can be detailed as:

$$I = \frac{-j\,k\,\eta}{(2\,\pi)^2} \iint F_{b,p}(k_x,\ k_y)F_{t,p}(k_x,\ k_y) \ \frac{1}{2\,j\,k_z}$$

$$\Gamma_p(k_x,\ k_y) \ dk_x\,dk_y \tag{5.13}$$

where the radiation pattern of the testing function has a slightly different form compared to that of the radiation pattern of the basis function in (5.10)

$$F_{t,p}(k_x,\ k_y) = \iiint_V \vec{J}_t(x',y',z') \ \cdot\ \hat{e}_p\, e^{-j\,(k_x\,x'+k_y\,y'+k_z\,z')}\, dV \tag{5.14}$$

where it is important to note the changes of sign in the exponent, as compared with the expression (5.9) of $F_{b,p}$. Regarding propagation in $+z$ versus $-z$ directions, one has to pay attention to the change in definitions of the polarization vector: x and y components of vector $\hat{e}$ change sign in the TM case (see equations (5.4) and (5.5)). Hence, four different radiation patterns will be needed for this method as follows: for each basis function, the radiation patterns will be calculated for TE and TM modes, and for both propagation directions ($-z$ and $+z$). We also calculate the reflection coefficients Γ_{TE} and Γ_{TM} to account for the reflection from the ground.

For the results below, the SDP(Steepest-descent Path) contour deformation is used in the complex β plane. Other types of contours, such as the parabolic contour, have been used in [113] where the impedance matrix is filled similar to Z^g. The imaginary part of β in the SDP contour deformation is defined in terms of the real part of β (β_R) as follows [104]:

$$\beta_I = \frac{\beta_R}{S} \tag{5.15}$$

with $S = \sqrt{1 + \left(\frac{\beta_R}{k}\right)^2}$,
and

$$\frac{d\beta_I}{d\beta_R} = \frac{1}{S^3} \tag{5.16}$$

also,

$$\frac{k_{xI}}{k_{xR}} = \frac{k_{yI}}{k_{yR}} = \frac{\beta_I}{\beta_R} \tag{5.17}$$

with $k_x = k_{xR} + jk_{xI}$ and $k_y = k_{yR} + jk_{yI}$

For details on how (5.15) to (5.17) are obtained, one may refer to [104] and [114].

To avoid a singular integrand, we adopt a contour deformation in complex β plane with

$$\beta = \beta_R + j\beta_I = \sqrt{k_x^2 + k_y^2} \tag{5.18}$$

As proven in [114], the contour deformation can be applied while still integrating over real (k_x, k_y) coordinates. To do this, it is necessary to include the following Q factor [114] in the integrand

$$Q(k_x, k_y) = \left(1 + j\frac{d\beta_I}{d\beta_R}\right)\left(1 + j\frac{\beta_I}{\beta_R}\right) \tag{5.19}$$

where $\beta_I(\beta_R)$ is the function that defines the integration path.

Finally, from (5.13) and (5.19), the total tested field for a given pair (t, b) of testing and basis functions is obtained as

$$\begin{aligned} Z^g_{t,b} = \frac{-j\,k\,\eta}{(2\,\pi)^2} \iint (F_{b,TE}\,F_{t,TE}\,\Gamma_{TE} + F_{b,TM}\,F_{t,TM}\,\Gamma_{TM}) \\ \frac{1}{2\,j\,k_z}\,Q(k_{xR}, k_{yR})\,dk_{xR}\,dk_{yR} \end{aligned} \tag{5.20}$$

5.2.3 Spectral sampling of (k_x, k_y) grid points

The spectral-domain MoM approach is employed to compute the interactions between elementary basis and testing functions. The interactions between elementary basis functions can be expressed as an extension of what is found in (5.20).

A square grid in (k_{xR}, k_{yR}) coordinates is used with $N = N_x = N_y$ points. It is important to wisely choose the density and extent of the k_{xR}, k_{yR} grid.

As explained in [104] and [115], a proper choice of integration domain range and number of points $N = N_x = N_y$ can lead to a compensation between aliasing and truncation errors. Let us define the range of integration as from $-k_{max}$ to $+k_{max}$. Based on an intermediate-to-far field approximation, the integral can be proven to resemble the Fourier transform of a Gaussian function with standard deviation close to $\sigma = (k/(2z))^{1/2}$ [115], where k is the wavenumber and z is the distance between the bottom of the antenna and the ground. Therefore, a link can be established between the number of points N and the normalized half width of the integration domain k_{max}/σ.

It is known that the number of required plane waves decreases with increasing distance between the antenna and the ground [116]. It should be noted that the actual errors can differ a bit based on the distance between the antenna and the ground. For each chosen N, an appropriate range of distances is selected in order to attain the threshold of relative error in the order of 10^{-2} with respect to the exact solution of the Green's function in the case of very close distances between the antenna and the ground (less than 0.05λ). The error in this case causes a variation in antenna impedance at the second decimal.

A relative error in the order of 10^{-4} is set for distances between the antenna and the ground larger than 0.05λ. The relative error is defined as:

$$e_r = \frac{GF_{ex} - GF_{FGCM}}{GF_{ex}} \tag{5.21}$$

where GF_{ex} is the exact solution of Green's function, and GF_{FGCM} is the Green's function obtained using the FGCM method. A perfect electrical conductor (PEC) ground is taken into consideration for this case. The lateral deviation $(\Delta x, \Delta y)$ is chosen as $(0.5, 0.5)\lambda$ to approximately account for the width of the antenna. Table 5.1 provides for each chosen $N = N_x = N_y$, the corresponding half width of the integration domain k_{max}/σ, with the associated range of distances.

Table 5.1: Number of integration points and associated domain of integration.

Range	nb. integ. points	The normalized integration domain k_{max}/σ
$0.91 < z/\lambda < 2.8$	13	1.4889
$0.5 < z/\lambda < 0.91$	15	1.3116
$0.2 < z/\lambda < 0.5$	17	1.1698
$0.1 < z/\lambda < 0.2$	21	1.0599
$0.05 < z/\lambda < 0.1$	25	0.8685
$z/\lambda < 0.05$	35	0.7574

Suitable N_x, N_y values can be obtained by determining the minimum antenna height and referring to the corresponding N_x, N_y values in Table 5.1. If the antenna lateral dimensions are significantly larger, Table 5.1 will need to be recalculated.

5.2.4 Numerical implementation

To implement this approach, the values of Γ, Q, F_b and F_t for each basis and testing functions can be arranged in matrix forms. One may define $\cdot*$ as the matrix element-by-element product, $*$ as a matrix product and $\bar{1}$ as a matrix of length equal to the number of BFs or TFs and width equal to one. The same mesh will be used for excitation, and we define M as the number of BFs. The integration in (5.20) can be written as a matrix multiplication as follows:

$$\bar{\bar{Z}}^{g}_{t,b} = \bar{\bar{F}}_{t,TE} * (\bar{\bar{F}}_{b,TE} \cdot *(\bar{\Gamma}_{TE1} * \bar{1}))+ \\ \bar{\bar{F}}_{t,TM} * (\bar{\bar{F}}_{b,TM} \cdot *(\bar{\Gamma}_{TM1} * \bar{1})) \tag{5.22}$$

where

$$\begin{aligned} \Gamma_{TE1} &= \Gamma_{TE} \frac{-Q(k_x, k_y)}{(2\,\pi)^2} \frac{k\eta}{2k_z} \Delta k_x \Delta k_y \\ \Gamma_{TM1} &= \Gamma_{TM} \frac{-Q(k_x, k_y)}{(2\,\pi)^2} \frac{k\eta}{2k_z} \Delta k_x \Delta k_y \end{aligned} \tag{5.23}$$

where $\bar{\bar{F}}_{t,TE}$ is a matrix with dimensions of M by $N_x \times N_y$, $\bar{\bar{F}}_{b,TE}$ is a matrix with dimensions of $N_x \times N_y$ by M, $\bar{\Gamma}_{TE1}$, $\bar{\Gamma}_{TM1}$ are matrices with dimensions of $N_x \times N_y$ by one, and $\bar{\bar{Z}}^{g}_{t,b}$ is a matrix with dimensions of N_x by N_y. Δk_x and Δk_y are the wave number steps along k_x and k_y, respectively. When changing the ground parameters, only Γ_{TE} and Γ_{TM} need to be recomputed, and a new matrix $\bar{\bar{Z}}^{g}$ is efficiently calculated. This sort of formulation allows for significant improvement in computational speed in certain computational languages, as Matlab®. More information about the required time to obtain the radiation patterns, reflection coefficients and to fill the matrix Z^g will be provided in Section 5.3.A.

Then, for all pairs of basis and testing functions, the MoM impedance matrix is given by

$$Z = Z^g + Z^f \tag{5.24}$$

where Z^g includes all effects of interaction with the ground. Z^f is the free-space impedance matrix obtained using the brute-force MoM solution or interpolated versus frequency using FMIR-MoM [102], considering that the antenna is in free space.

5.3 SIMULATION RESULTS AND DISCUSSION

5.3.1 Validation against brute-force MoM for a Vivaldi antenna above PEC ground

The antenna under consideration is a 3D Vivaldi antenna above a ground plane operating from 1.5 GHz to 6 GHz. The antenna is represented by the surface mesh in Fig. 5.2 with 1360 RWG [117] basis functions. The antenna dimensions are 7.5×10×0.5 cm, and it is placed at d=10.75 mm above a PEC ground, as shown in Fig. 5.2. The Vivaldi antenna mesh was produced using GMSH [41].

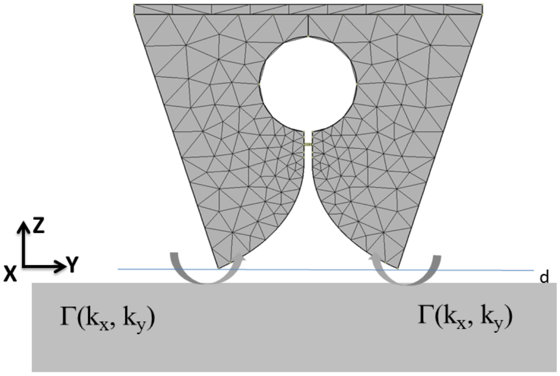

Figure 5.2: Vivaldi antenna at d=10.75 mm above ground.

An electromagnetic simulation solver developed at UCL, based on the conventional Method of Moments [16], was used to calculate the free-space impedance matrix Z^f. This software can solve the problem of an antenna in the presence of a PEC ground using image theory. It is not possible to include a dielectric ground in this example. Validations for real and imaginary parts of the input impedance can be seen in Fig. 5.3. The results show an excellent agreement between the FGCM technique and the brute-force MoM for this type of 3D antennas above a PEC ground.

The simulations were carried out using a PC with 24 GB RAM and a 2.4 GHz Intel Xeon Core Processor. For a single frequency, the FGCM method requires 89.9 seconds of preparation time, which includes the calculation of the four radiation patterns per basis function, as well as the free-space brute-force MoM matrix. All matrix filling times are provided in Table 5.2. The dimensions of the (k_x, k_y) grid are set to $N_x = N_y = 35$.

For a given set of soil parameters, it is only necessary to recalculate the reflection coefficients Γ_{TE} and Γ_{TM}, as well as the matrix multiplications in (5.22) after uploading the off-line patterns of basis functions and the free-space MoM matrix. This procedure only takes 1.5 seconds, to be compared with 33.5 seconds (the difference between 97.8 and 64.3 seconds) in the case of brute-force MoM. It was feasible to keep the radiation pattern matrices in RAM, so we could save their uploading time. For each frequency, it is necessary to upload the radiation patterns once. The FGCM method speeds up the brute-

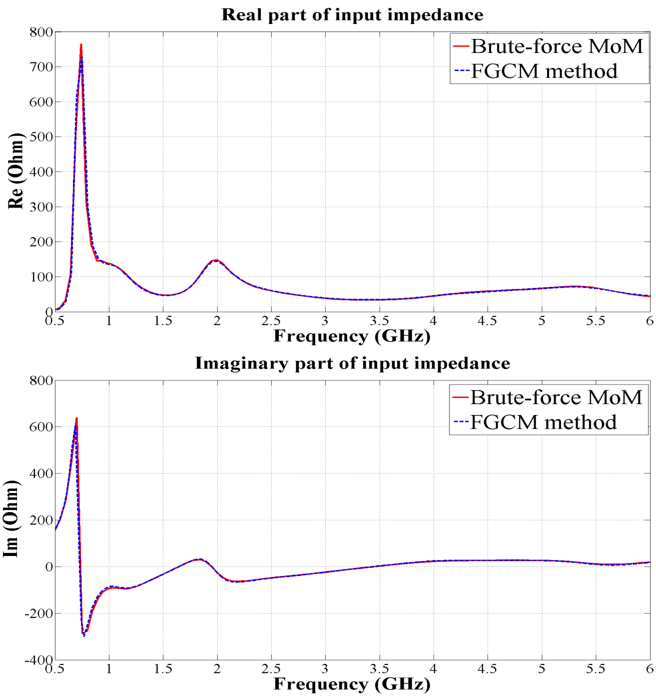

Figure 5.3: Real and imaginary parts of the antenna input impedance.

Table 5.2: FGCM DETAILED COMPUTATION TIMES

Operation	Time (s)
Free-space brute-force MoM matrix Z^f	64.3
Brute-force MoM with a PEC ground	97.8
All radiation patterns	25.5
Γ_{TE} and Γ_{TM}	0.094
Matrix multiplication and filling of Z^g	0.67
Uploading offline patterns and free-space MoM matrix	0.73

force MoM by a factor of 22, and hence allows for efficient loops over soil parameters. The time needed to obtain the ground coupling matrix Z^g has a direct relation with the number of points in the (k_x, k_y) grid. More details on this parameter are provided in Section B.

5.3.2 Influence of (k_x, k_y) grid resolution

As explained in Section 5.2.3, the number of points in (k_x, k_y) grid is carefully chosen based on a compensation between aliasing and truncation errors. The influence of using a coarse (k_x, k_y) grid is observed in Fig. 5.4, which shows the effect of different values of N_x and N_y parameters for the case of the Vivaldi antenna placed above a PEC ground. Increasing the number of points N_x, N_y from $N_x = N_y = 35$ to $N_x = N_y = 75$ will increase the time needed to create the radiation patterns from 25.5 to 115.9 seconds, without significant effect on accuracy.

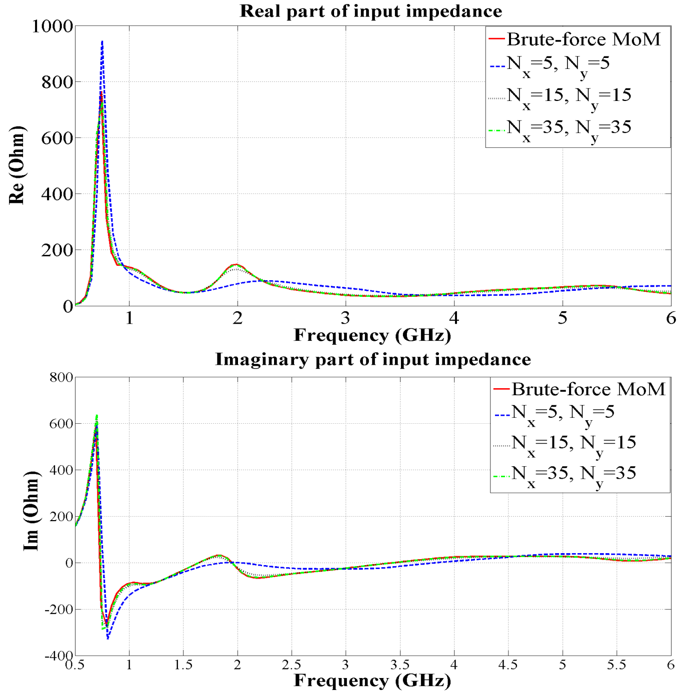

Figure 5.4: The influence of (kx,ky) grid resolution.

5.3.3 Dependence on antenna-ground distance

From (5.14) and (5.20), it is found that it is possible to very efficiently account for the effect of changing the vertical distance between the antenna and the ground by introducing an air layer just above the layered medium. It is worth noting that the antenna coordinates and radiation patterns do not change.

Thus, only Γ needs to change as follows

$$\Gamma_{TE,TM(z+\Delta z)} = \Gamma_{TE,TM(z)}\ e^{-2jk_z\Delta z} \tag{5.25}$$

where Δz is the difference between the two vertical distances. A simulation has been carried out applying the FGCM method for a distance of 10.75 mm between the Vivaldi antenna and a PEC ground. The reflection coefficient obtained from this simulation is multiplied by the factor $e^{-2jk_z\Delta z}$, where Δz is set to 10.5 mm. The obtained results have been compared with the brute-force solution in the case of a PEC ground for a distance of 21.25 mm between the antenna and the ground. The results are in excellent accordance, as shown in Fig. 5.5. For comparison, the computational time needed to create the radiation patterns for a height of 21.25 mm at a single frequency is 25.5 seconds, while only 1.28 seconds are needed to update the MoM matrix by phase shifting Γ.

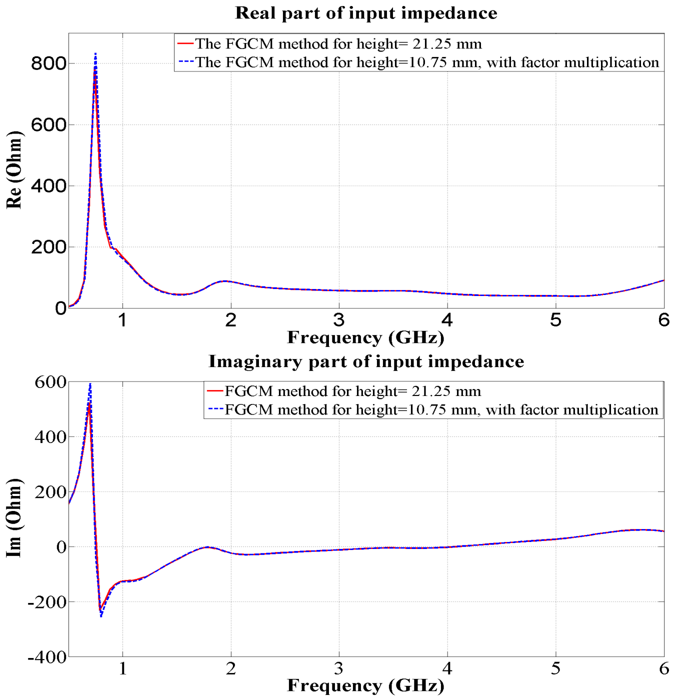

Figure 5.5: Validation of antenna input impedance while modifying the vertical distance between the antenna and the ground.

5.3.4 Validation against IE3D for a dipole antenna above a multilayered medium

The FGCM method is validated below with results obtained with the commercial software IE3D [118], while considering a dielectric ground. A horizontal dipole in the form of a 5×0.25 cm rectangular strip is placed 1 cm above a lossless multi-layered medium (see Fig. 5.6 for medium details). For the FGCM results, the dipole is discretized using the GMSH software into 37 RWG basis functions. The number of (k_x, k_y) grid points is taken as $N_x = N_y = 19$. Table 5.3 gives the computation times for both cases.

Table 5.3: IE3D AND FGCM COMPUTATION TIMES

Operation	Time (s)
IE3D software	0.4
FGCM method	0.156
Update of Z^g when changing ground parameters while having patterns precalculated	0.078

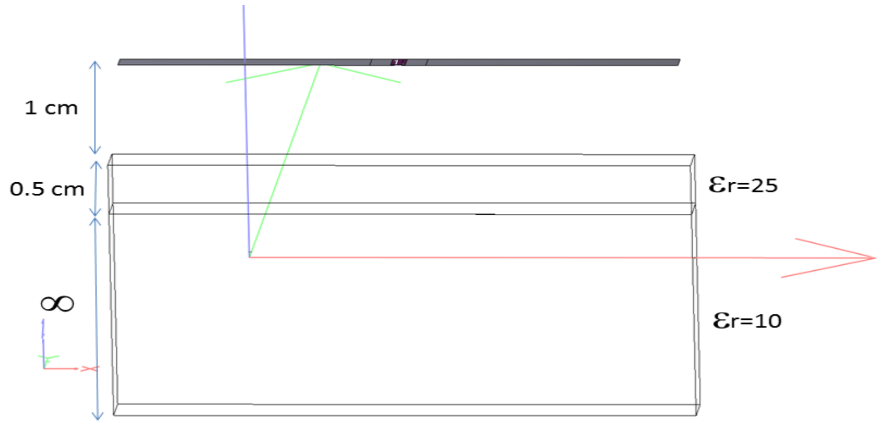

Figure 5.6: Horizontal dipole in the presence of a lossless multi-layered infinite ground; plot generated with IE3D.

Fig. 5.7 shows a very good agreement between the FGCM results and IE3D simulations. The free-space results added on the plots illustrate the very sig-

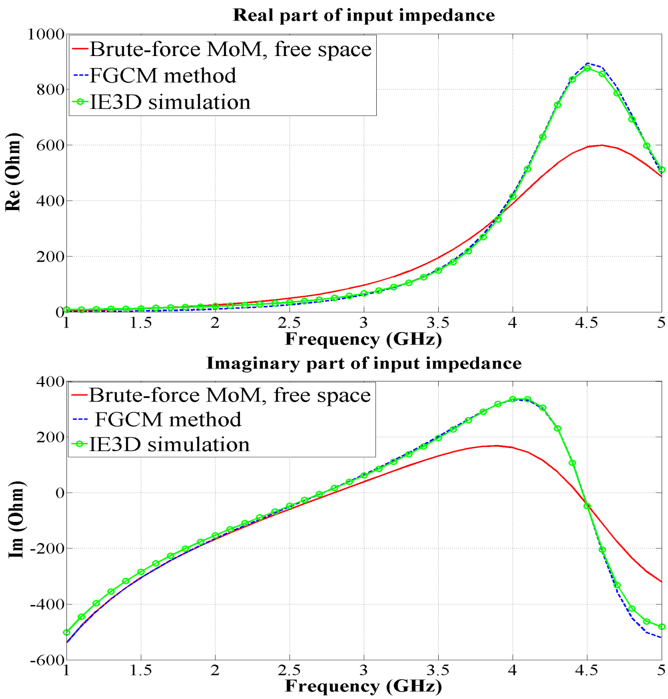

Figure 5.7: The antenna real and imaginary parts of input impedance as a function of frequency for three different simulations: free-space, FGCM method and IE3D simulation (the latter two in presence of layered medium).

nificant effect of the multilayered medium on the input impedance of the antenna.

5.3.5 Validation against the FDTD method for a dipole antenna

The finite difference time domain (FDTD) [119] method has been widely used to model lossy and dispersive materials, as well as antennas [120]. The FGCM method is validated against the FDTD method obtained with the commercial software SEMCAD X Matterhorn SOLUTIONS [121], while considering PEC and dielectric media. A dipole in the form of a 50×1.11 cm cylinder is placed 5 cm above a huge cube ($300 \times 300 \times 28$ cm) of PEC and lossy medium, as shown in Fig. 5.8. The medium has a relative permittivity of 5.54 and a conductivity of 0.0327 S/m. For the FGCM results, the dipole is discretized using the GMSH software into 1158 RWG basis functions. The number of (k_x, k_y) grid points is set to $N_x = N_y = 35$. Fig. 5.9 shows a very good agreement between the

FGCM method and SEMCAD simulation for both cases, i.e. PEC and lossy media, which validates the FGCM method over the FDTD technique. Table 5.4 compares the time needed for both methods for a single frequency.

Table 5.4: SEMCAD AND FGCM COMPUTATION TIMES

Operation	Time (s)
SEMCAD software	6.91
All radiation patterns	21.257
Γ_{TE} and Γ_{TM}	0.137
Update of Z^g when changing ground parameters while having patterns precalculated	1.67

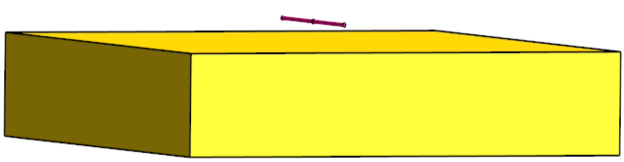

Figure 5.8: A dipole in the presence of a layered medium; plot generated with SEMCAD.

5.4 EXPERIMENTAL MEASUREMENT VALIDATION AND DISCUSSION

We show here the measured results for a single 3D Vivaldi antenna prototype (Fig. 5.10). This antenna was initially designed as part of an antenna array for imaging applications [122]. The prototype operates from 1.5 GHz to 6 GHz as shown in Fig. 5.11. Two cases of layered medium will be taken into consideration: PEC and lossy grounds. The measurements are recorded at different vertical distances between the antenna and the ground.

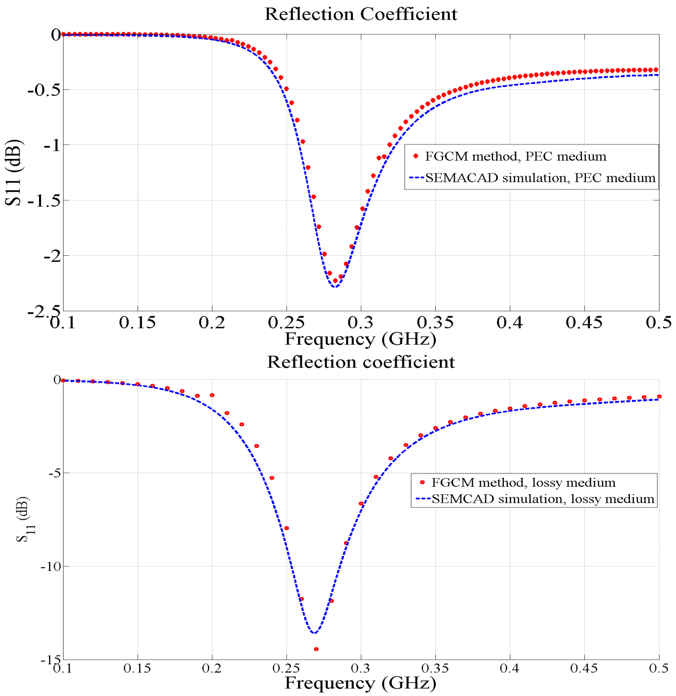

Figure 5.9: The reflection coefficient comparison between FGCM method and SEMCAD simulation in the case of PEC and lossy media.

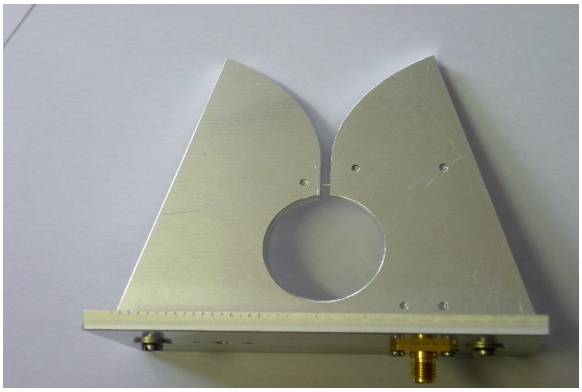

Figure 5.10: The 3D Vivaldi antenna prototype.

5.4.1 Experimental validation in the case of a lossy ground

Fig. 5.12 shows the measurement setup in the case of a lossy ground. The lossy medium consists of a stack of 7 clay pavers; 280 mm thick with a metal plate underneath. The pavers have a relative permittivity of 4.8 ± 0.5 and a

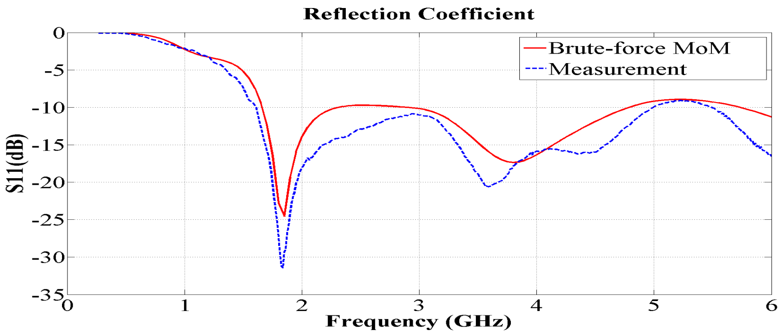

Figure 5.11: Comparison of free-space reflection coefficient between the brute-force MoM and measurement for the 3D single Vivaldi prototype.

conductivity of 0.05 ± 0.015 S/m [123]. The Vivaldi antenna is placed at a distance of 0 mm (touching the pavers) and 23.5 mm above the lossy ground. As can be seen in Fig. 5.13, a relatively good agreement between the measured and FGCM results is achieved.

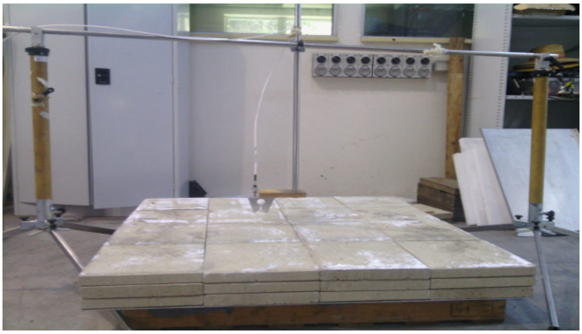

Figure 5.12: Experimental setup in the case of a lossy ground, shown with a stack of 3 clay pavers (the results presented in this chapter use a thickness of 7 pavers).

5.4.2 Experimental validation in the case of a PEC ground

The pavers were replaced by a large metal plate (PEC) which is placed 10.75 mm and 21.25 mm below the 3D Vivaldi prototype. Fig. 5.14 shows a good level of agreement between the measurement and the FGCM results.

GPR data can be presented in time domain. The frequency domain signal obtained from the reflection coefficient is inverse Fourier transformed to

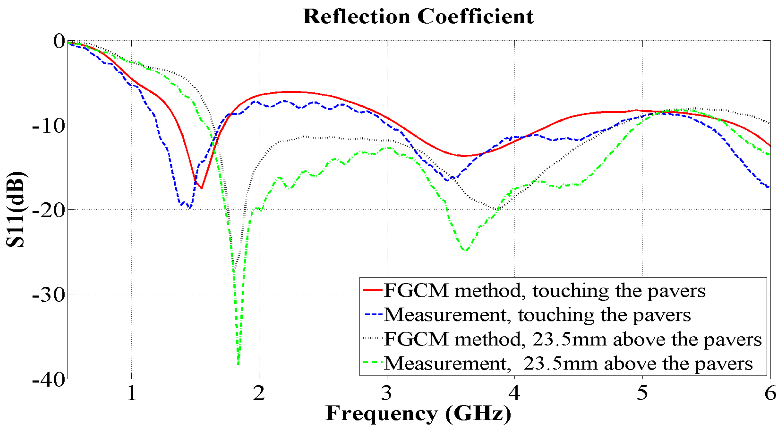

Figure 5.13: Comparison of reflection coefficient between the FGCM method and measurement in the case of a lossy ground.

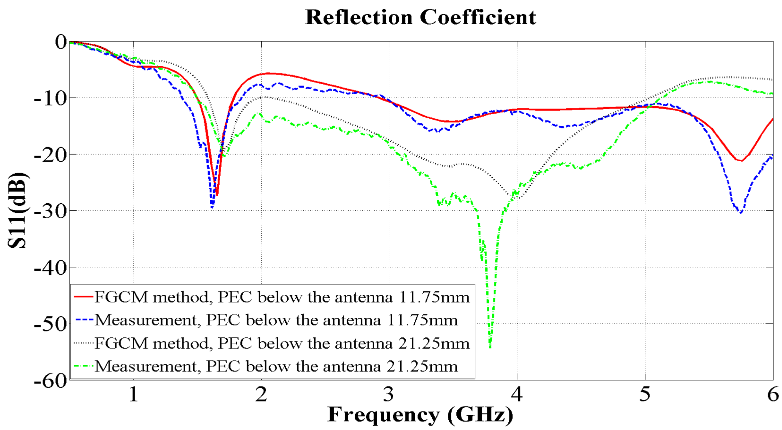

Figure 5.14: Comparison of reflection coefficients between the FGCM method and measurement in the case of a PEC ground.

obtain the time domain response. Fig. 5.15 shows the time domain response comparison for two cases: (1) the simulated difference between the free-space and a lossy medium of 7 clay pavers placed 23.5 mm below the Vivaldi antenna with relative permittivity of 4.8 ± 0.5 and conductivity of 0.05 ± 0.015 S/m; 280 mm thick with a metal plate underneath, (2) the measured difference for the same case as in (1). The antenna is fed with a unit voltage. The phase shift between the simulated and measured results has been corrected. This phase shift is due to the feed length difference between the GMSH model and the fabricated antenna. The cable length calculation is obtained from the free-space data. For simplicity, it is assumed that the coaxial cable in the Vivaldi antenna is lossless and leads to a phase factor of e^{jak_z}. A linear least squares method is used to find the value of a which minimizes the error between measurements and simulations. This allows to cater for the coaxial cable length. Fig. 5.15 shows a good matching between the simulated and measured results, where the first layer and the metal plate are well detected at the same time-domain peaks. The data obtained from Fig. 5.15 can be used to approximately calculate the layer thickness using the following equation:

$$d_n = \frac{(t_2 - t_1)\sqrt{\epsilon_r}}{2c} \tag{5.26}$$

where t_1 and t_2 are the timing of maxima corresponding to the first layer and the metal plate, respectively, and c is the speed of light.

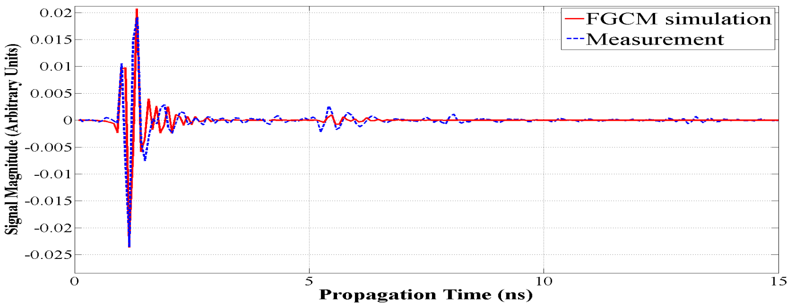

Figure 5.15: Comparison of time domain response between the FGCM method and measurement in the case of a lossy medium.

Table 5.5 shows the layer thickness calculated from the data obtained from the plot above, with the percent error in layer thickness Δn. The precision of the simulation method may be evaluated by taking the maximum value of the absolute error between simulation and measurement at returns of particular interest and dividing by the maximum of the measured return with the antenna in free-space. For the return from the air/paver interface (large return at approximately 1.5 ns) this is -74dB, while it is -49 dB for the paver/metal interface (small return at approximately 6 ns). The loss in accuracy for the later return is probably due to difficulties in obtaining an accurate ground truth measurement of the paver's loss tangent. It should be noted that the free-space return has been removed from Fig. 5.15 to enable the later returns to be viewed clearly.

Table 5.5: LAYER THICKNESS IN SIMULATED AND MEASURED DATA

Operation	$d_n(mm)$	$\Delta n(\%)$
Simulated	295.2	5.1
Measured	290.7	3.6

5.5 CONCLUSION

A novel fast method based on the MoM solution of integral equation is proposed to add the contribution of ground on antennas. We named the method Fast Ground Coupling Matrix (FGCM). The MoM impedance matrix is divided into two parts: the free-space matrix and the ground contribution matrix. The free-space matrix is obtained by conventional brute-force MoM solution. The ground contribution matrix is obtained by efficient multiplication of radiation patterns of the basis/testing functions and the reflection coefficient in the spectral domain. The spectral integration is carried out in 2D spectral coordinates using the steepest-descent path. A minimum number of samples is achieved through compensation between aliasing and truncation errors. The physical parameters of the ground only appear through the reflection coefficient. This property allows for very fast update of the ground contribution matrix, while looping through soil parameters. The proposed method has been validated against the exact MoM solution in the case of a PEC ground. The FGCM method has also been validated against the commercial software IE3D in the case of a lossy multilayered ground, and SEMCAD (FDTD method) in the case of PEC and lossy media. Considering a 3D wideband antenna, it has been shown that the FGCM method is 22 times faster than the MoM brute-force solution (1.5 seconds compared to 33.5 seconds per frequency) when changing the ground permittivity, conductivity, permeability, number of layers, layer thickness, and/or antenna height. Accurate experimental validation has been provided for antennas at a range of distances above both PEC and lossy dielectric grounds.

Acknowledgment

This project has been partly funded by the SENSPORT project of Region Wallone.

6

On the Use of Contour-FFT for the MBF-based Analysis of Arrays of Antennas Placed Vertically Above a Multi-layered Substrate

This work has been done in collaboration with Sumit Karki (MBF approach) and Dr. Shambhu N. Jha (C-FFT method). A method is proposed for the fast Macro Basis Functions (MBFs) characterization of antenna arrays placed vertically above a multi-layered substrate by using the Contour-Fast Fourier Transform (Contour-FFT) method. The presented work aims at accelerating the evaluation of interactions between the MBFs defined on the elements corresponding to antennas extending vertically above the ground. We first write a complex-plane extension of the interaction between antennas via reflection by the ground. The calculation is then accelerated using the Contour-FFT. We exploit the Contour-FFT available for planar arrays to efficiently obtain the solution of the currents on the vertical antennas with the consideration of reflections from the semi-infinite ground. Results are presented and future perspectives are highlighted. In recent years, various numerical methods have been proposed for the fast analysis of antenna arrays. The Method-of-Moments (MoM) [16] technique has been widely used to solve problems involving currents on metallic and multilayered dielectric structures [124]. The computational complexity of MoM based on brute-force technique rapidly becomes prohibitive. To solve this issue, the Macro Basis Functions (MBFs) method [125] [126] [45] is used. The MBF method is a decomposition technique, which reduces the computational complexity in solving time by a factor $(N/M)^3$, where N is the number of elementary basis functions, and M (M $<<$N) is the number of MBFs per antenna.

Although the traditional MBF method solves the issue of solution time, the complexity of finding the MBF interactions remains the same. The Contour-FFT (C-FFT) technique [114], among many other available fast methods [127] [128], presents a new formulation of accelerating the computations of MBF interactions. It consists of expanding the kernel obtained by a parabolic contour deformation to make it suitable for FFT acceleration of spectral-domain interactions, including proper treatment of poles. In this work, we exploit the C-FFT method to analyze the large arrays of vertical antennas placed over a semi-infinite ground. The preliminary results confirm that C-FFT can be readily applied to that configuration. We use the C-FFT method to accelerate the evaluation of MBF integrals with $N \log_2 N$ complexity for the interactions involving reflection by the ground. The free-space part of the interactions has been accelerated with the multipole approach [129] [130] [131]. Interactions among array elements farther than a wavelength have been computed using the multipole approach while the near- and self-interactions have been computed using the brute-force method.

The remainder of this chapter is organized as follows. Section 6.1 presents a brief explanation on the proposed mathematical approach. Validation results of the proposed method are reported in Section 6.2. Finally, conclusions and future prospects are drawn in Section 6.3.

6.1 Mathematical formulation

The proposed approach starts from the spectral formulation presented in Chapter 5 for the computation of the MoM impedance matrix of an antenna located above the ground. The reader is reffered to Section 5.2 for the details.

6.1.1 MBF Approach

For all pairs of basis and testing functions, the MoM impedance matrix is given by:

$$Z = Z_l^c + Z_h \tag{6.1}$$

where Z_l^c includes the effect of the multi-layered medium Green's function and will be treated with the C-FFT method. Z_h is the homogeneous impedance matrix obtained in free-space and will be treated with the MBF-multipole approach. For a basis antenna element n and a testing antenna element m, the homogeneous impedance matrix can be directly reduced using this approach and is given as [131][134]:

$$Z_h^{mn}(i,j) = -\frac{k^2\eta}{(4\pi)^2} \iint \vec{F}_i(\hat{u}) \cdot \vec{F}_j^*(\hat{u}) T(k, \vec{p}_{mn}, \hat{u}) dU \tag{6.2}$$

The integration is done over a unit sphere U spanning different directions in $\hat{u}$. The far field patterns of the basis functions are given by $\vec{F}_i$, and the translation function between element m and n for a wavenumber k and for a radial distance $\vec{p}_{mn}$ is given by T.

The reduced impedance matrix, Z', can be computed using the MBF approach. It reduces the size of the matrix Z by grouping the elementary basis functions into a set of aggregate functions called the macro basis functions, which are generated by the 'primary-and-secondary' approach [135]. The reduced MoM interaction matrix and the excitation vector are the given as:

$$Z' = Q^H Z Q \tag{6.3}$$

$$v' = Q^H v \tag{6.4}$$

where the superscript $(^H)$ is the Hermitian transpose. The reduced system of equations now reads as $Z'i' = v'$.

With the MBF approach, the size of the MoM matrix is reduced from $NA \times NA$ to $MA \times MA$, where A is the number of antenna elements in the array. Since $M << N$, the size of the MoM matrix is considerably reduced.

6.1.2 Field reflected by a multi-layered medium

The interaction between Macro Basis Functions (MBFs) is given as

$$
\begin{aligned}
Z_l = \frac{-j\,k\,\eta}{(2\,\pi)^2} \iint (F_{b,TE}\,F_{t,TE}\,\Gamma_{TE} + F_{b,TM}\,F_{t,TM}\,\Gamma_{TM}) \\
\frac{1}{2\,j\,k_z}\,Q(k_x,k_y)\,dk_x\,dk_y
\end{aligned}
\tag{6.5}
$$

where F_b and F_t are "basis" and "testing" radiation patterns for the MBFs, as defined in (5.10) and (5.14) for elementray basis functions. Q, detailed in (6.19), is a factor including the effect of contour deformation in complex wavenumber plane. The patterns of all MBFs are supposed to be computed with a common reference point regarding the phase. It is convenient to shift the reference point toward each antenna on which the MBF is defined. This introduces a phase factor in which Δx and Δy, the vector distance between antennas, appears:

$$
\begin{aligned}
Z_l^c = \frac{-j\,k\,\eta}{(2\,\pi)^2} \iint \Big({F^0}_{b,TE}\,{F^0}_{t,TE}\,\Gamma_{TE} + {F^0}_{b,TM} \\
{F^0}_{t,TM}\,\Gamma_{TM}\Big) \frac{1}{2\,j\,k_z}\,Q(k_x,k_y)^{-j(k_x\Delta x + k_y \Delta y)}\,dk_x\,dk_y
\end{aligned}
\tag{6.6}
$$

where F^0 refers to the radiation pattern obtained from the central element. The phase factor transforms this expression into a Fourier Transorm. As will be explained in Section 6.1.3, (6.6) will be estimated efficiently on a regular grid in (Δx,Δy) plane with the help of a FFT.

6.1.3 C-FFT acceleration method

The C-FFT [114] is a method to accelerate the evaluation of space-domain substrate-related interactions, which provides a $N \log_2 N$ complexity. This method will be used to accelerate the computation of (6.6) as it has a Fourier transform structure. However, to obtain an efficient result, one has to treat the surface wave poles in spectral domain. This has been done with the use of steepest descent path (SDP) contour [103]. Actually, when one considers the contour-deformation, the integral kernel no longer corresponds to a purely imaginary exponential (i.e. the Fourier transform kernel); hence the FFT acceleration cannot be applied directly to it. This problem has been solved through a Taylor's series expansion of the real exponential that results from contour deformation [114]. In that work, the C-FFT method has been demonstrated for large arrays of printed horizontal antennas using parabolic contour deformation. We exploit here the benefits of the C-FFT method to analyse large arrays of vertical antennas placed over the multilayered substrate or the semi-infinite ground (Earth) using the SDP contour. As shown in Section 6.2, the C-FFT can be extended to the vertical antenna case when the elements are entirely located on one side of the air-ground interface. Equation (6.6) can be written in the DFT summation form suitable for acceleration with the C-FFT approach [114] as follows:

$$\begin{aligned} Z_l^c &\cong \sum_p \sum_q \widetilde{I}_M e^{-i(k_x \Delta x_p + k_y \Delta y_q)} \Delta k_x \Delta k_y \\ &+\Delta x \sum_p \sum_q \gamma k_x \widetilde{I}_M e^{-i(k_x \Delta x_p + k_y \Delta y_q)} \Delta k_x \Delta k_y \\ &+\Delta y \sum_p \sum_q \gamma k_y \widetilde{I}_M e^{-i(k_x \Delta x_p + k_y \Delta y_q)} \Delta k_x \Delta k_y \\ &+ ... \end{aligned} \tag{6.7}$$

where we get the following formulation from (7.2)

$$\widetilde{I}_M = \frac{-j\,k\,\eta}{(2\,\pi)^2} \left(F^0{}_{b,TE}\, F^0{}_{t,TE}\, \Gamma_{TE} + F^0{}_{b,TM}\, F^0{}_{t,TM} \right. \tag{6.8}$$

$$\left. \Gamma_{TM} \right) \frac{1}{2\,j\,k_z}\, Q(k_x, k_y);\ \gamma = \frac{\beta_I}{\beta_R}$$

$\beta_R = \sqrt{k_x^2 + k_y^2}$, $\beta_I = f(\beta_R)$ corresponds to contour deformation. As can be seen from (6.7), the space domain parameters Δx and Δy are factored out, which allows one to exactly identify the double sums with the Discrete Fourier Transform. The FFT operation directly provides all the interactions over a fine grid with spacings Δx and Δy.

6.2 Results and discussion

6.2.1 IE3D Validation of adding the ground contribution effect over the antenna

A vertical single diople of length 5 cm and width 0.25 cm has been chosen to validate the formulation (6.5), it will be further used as a reference solution based on the MBF method. A layered medium has been chosen as an infinite ground, with relative permittivity ($\epsilon_r = 25$), placed 1 cm under the vertical dipole. A dipole model provided by IE3D [118] in the case of vertical localized ports has been used in the comparison.

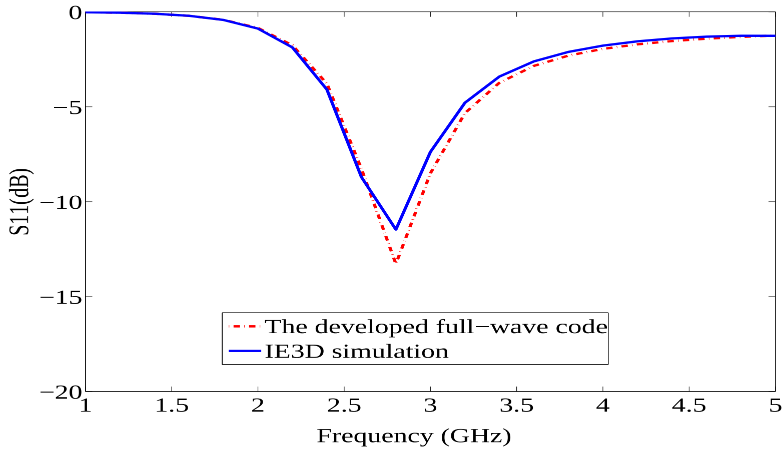

Figure 6.1: Reflection coefficient comparison between the developed full-wave code and IE3D simulations

The comparison between IE3D simulation and the developed full-wave code (Fig. 6.1) shows a very good correspondance.

6.2.2 The case of large arrays of vertical dipoles

Simulations have been carried out for a regular grid of dipoles (10×10) of length 5 cm and width 0.25 cm at the central frequency of 2.8 GHz. The same layered medium used previously has been chosen in the simulation. The dipoles are designed and meshed using the GMSH [41] software. Each dipole is meshed with 37 basis functions. The planar regular array configuration is shown in Fig. 6.2, where it is placed 1 cm above the semi-infinite layered medium. The inter-element spacings Δx and Δy in the array are taken as $0.6\lambda_0$, where λ_0 is the free-space wavelength. We consider the case of exciting the center element, while the remaining dipoles are passively terminated with a 50 Ω load. The port currents obtained using the brute-force method are compared with the MBF method applied to interactions computed as in (6.1). The errors shown will be given in dB and are defined as $10log10|I_f - I_m|^2$ where, I_f and I_m are the port currents obtained using the brute-force method and MBF method, respectively. The results are normalized w.r.t. the maximum value of $|I_f|$. The comparison is of excellent accuracy with an error level well below -70 dB over the frequency band of interest using 25 MBFs, as shown in Fig. 6.3. The mutual coupling between elements in the array has been shown with currents on all elements in the array when the central element is excited, as shown in Fig. 6.4. As can be expected, the elements close to the center have higher port currents than those at the corners. The central element is denoted by number 1 while the farthest corner elements are denoted by numbers 89, 90, 99 and 100.

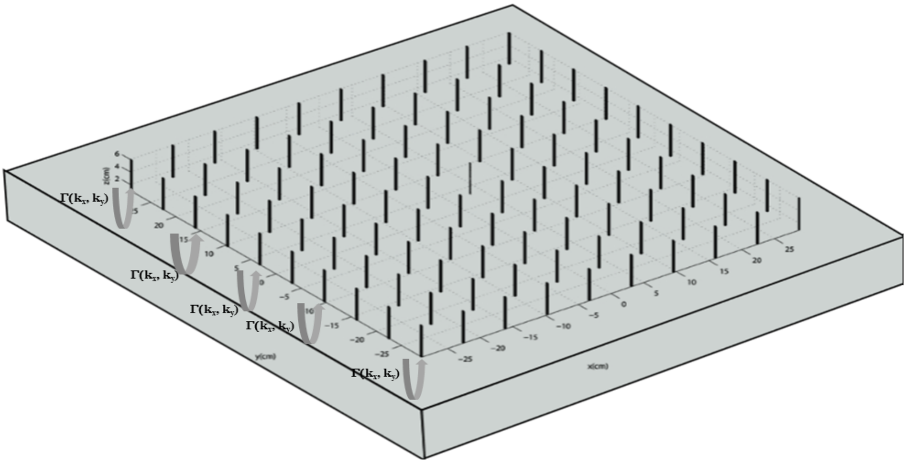

Figure 6.2: Regular planar array with 100 vertical dipole elements in the presence of a semi-infinite ground.

6.2.3 Analysis of a 3×3 regular array by C-FFT method

A regular array of 3×3 dipole antennas is placed vertically 1 cm above the lossy ground medium with permittivity $\epsilon_r = 25$. The array spacing in X and Y directions are taken equal to $0.6\lambda_0$, where the central frequency is equal to 2.8 GHz. The port currents obtained from the C-FFT method are compared with those obtained from the solution of the MBF method, as shown in Fig. 6.5.

For the analysis of large arrays, using a large number of k_x and k_y values is very important. At first, the patterns of macro basis and macro testing functions are evaluated for 59×59 $k_x - k_y$ grid. To achieve good accuracy and also save evaluation time of the radiation pattern, the corresponding values for larger spectral grid of size 1024×1024 is obtained by interpolation. The

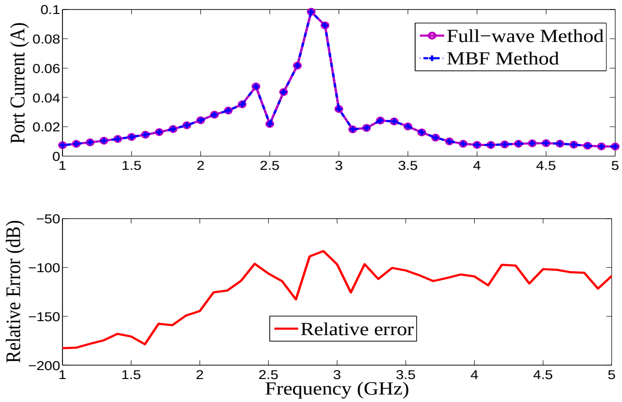

Figure 6.3: Comparison of port currents over the frequency band $(1 - 5)$ GHz.

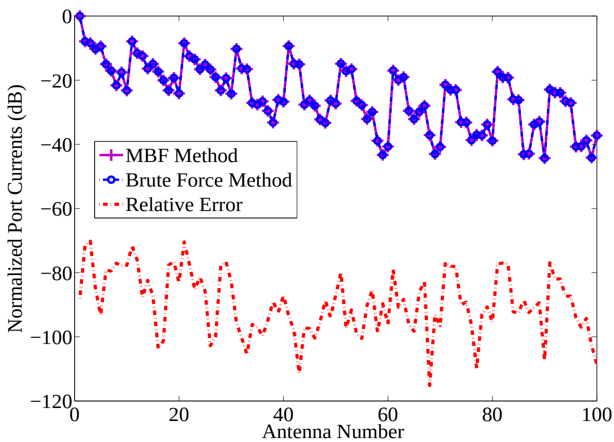

Figure 6.4: Port currents at the resonant frequency when the central element in the array is excited.

C-FFT expansion up to 5^{th} order has been used for this calculation and preliminary results suggest that to continue working with SDP contour, the number of terms in the FFT expansion have to be increased. The required order in C-FFT development increases with the product between contour height and array size [136]. Further works are needed to improve the accuracy and to benchmark the required number of FFT terms by lowering the contour.

The MBFs generation requires 515.74 seconds of preparation time. The MBF-based reduced matrix filling to obtain Z_l^c requires 229 seconds. Moreover, the time required to obtain Z_l^c by using C-FFT method is 158.25 sec-

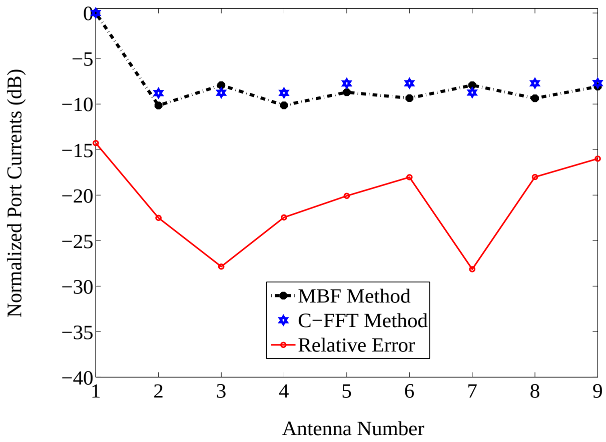

Figure 6.5: Port currents for MBF method and C-FFT at the resonant frequency when the central element in the array is excited.

onds. It should be noted here that the preparation time corresponds to a fixed amount of time, which will be the same irrespective of the size of the array. Furthermore, the time required to obtain the MBF-based interaction using the C-FFT method does not increase a lot, when we opt for the analysis of large arrays. That means, as the interactions are obtained in quasi-instant way using the C-FFT method, the aforementioned timing of 158.25 seconds would be just increased by few 10's of seconds when analyzing the bigger arrays.

6.3 Conclusion and future prospects

This work presents the possible use of Contour-FFT (C-FFT) approach to analyze large arrays of vertical and 3-D antennas placed over a semi-infinite ground or, possibly also, a layered medium. We presented some results in terms of validation of the basic form of the spectral evaluation. The first use of the SDP contour deformation combined with the C-FFT method available for planar arrays indicates that this can be extended to analyze large arrays of vertical antennas. However, we noticed that the number of FFT would increase a lot, if we continue working with SDP contour opting for better accuracy. Therefore, further work will be focused on lowering the contour and benchmarking the required number of FFT terms.

Conclusions and Future Works

7

7.1 Conclusions

In this work the complete design of various wideband three-dimensional antenna types mainly for imaging systems has been presented. In addition a fast numerical method has been developed to account for the effect of the ground on the antennas. We reviewed the state-of-the art from the literature for various metallic antenna designs, especially Vivaldi and monopole types, and studied the principle of radiation to produce compact and miniaturized antenna prototypes. At the beginning, we started with the design of a single 3-D traditional Vivaldi antenna. To improve the bandwidth of interest of the traditional Vivaldi antenna, an additional degree of freedom is added by modifying the major and minor radii of the ellipse curve, as well as the position of the center with respect to the feeding point. Ten Vivaldi elements have been assembled in a circular shape to configure of a 3-D UWB circular imaging array. A fast calculation method has been applied based on the Array Scanning Method applied to the MoM to simulate the circular array thereby accounting for all the effects of mutual coupling. Both single-element and array designs have been manufactured, and very good agreement has been obtained between measurement and simulation. We named the prototype as the ”Wheel-of-Time”. This prototype has been used for imaging and localizing targets in the next steps.

Proceeding with the fabricated WoT prototype, various image reconstruction algorithms are proposed to image and localize targets. Two metallic tubes have been used as targets to be localized, and a dielectric cylinder has been used to be imaged. Time-domain responses have been processed in order to provide an initial image of the metallic tube. The metallic tube is successfully depicted in the area of radiation exposure, and the target is localized. The

WoT prototype has also been used to distinguish between metallic cylinders in the area of radiation exposure. The Array Scanning Method applied to the Method of Moments is used to account for the connection between sectors of the whole structure. Good comparisons are obtained between ASM-MoMs simulations and measurements in the presence of metallic targets. The resolution between metallic cylinders is investigated experimentally and numerically. Regarding reconstruction of a dielectric cylinder of relative permittivity $\epsilon_r = 4$ positioned in the area of radiation exposure, preliminary imaging results have been obtained and the cylinder position and dimension are successfully revealed. After all these trails, the WoT has been proven as well designed and fabricated prototype, which gives us another confirmation about our techniques of simulation and fabrication.

An important component in the development of water leak detection is the design of a UWB antenna; i.e., to detect leaking pipe underground. The low frequencies are very important in this application to be able to penetrate deeper into the ground, as well as high frequencies to reconstruct images with high resolution. Low frequency antenna design is challenging due to the expected large dimensions of the radiator. The bandwidth of interest is set from 0.25 GHz to 2.5 GHz. A UWB Vivaldi antenna design has been proposed with $60 \times 41 \times 1.5$ cm dimensions. We took as an objective to minimize the antenna weight by introducing holes at specific positions related to the current distributions. Further alternative solution could be achieved by making the antenna hollow from inside (as provided in the thesis of Dr. Remi Sarkis). This solution will increase the fabrication cost, due to the high technology used. The proposed antenna has been fabricated and measured at UCL. The comparison between measurements and simulations is very satisfactory, with a bandwidth from 250 MHz up to 3.5 GHz under a -10 dB criterion in terms of reflection coefficient. Preliminarily tests have been carried out to examine the effect of nearby ground on the antenna. The trails have been carried out using the CST commercial software with two different permittivities, and it shows a remarkable effect on the antenna impedance at low frequencies through rapid oscillations. The team of Prof. Lambot, at UCL Earth and Life Institute, has tested the Vivaldi prototype. They do not encourage using the Vivaldi antennas for water leak detection where high resolution is needed, due to mismatching between the antenna and the ground at high frequencies. It is recommended to lower the antenna profile to better match the high frequencies with the ground. The prototype fabricated could be used to analyze the quality of road pavement.

The same antenna requires to be simulated many times with a large number of prospective soil properties. Applying the explicit use (or even precomputation) of the Green's function to account for the contribution of the ground on antennas costs much time, especially in large antennas, such as those presented in the Vivaldi prototype for water leak detection. A novel fast method based on the MoM solution of integral equations is proposed to add the contribution of the ground on the antenna response. We named the method Fast Ground Coupling Matrix (FGCM). The novelty of the method consists of obtaining a specific contribution of the ground to the MoM impedance matrix through an efficient multiplication of radiation patterns of the basis/testing functions and the reflection coefficients in spectral domain. A minimum number of samples is obtained through compensation between aliasing and truncation errors in spectral integration. The physical parameters of the ground only appear through the reflection coefficient. The spectral integration is carried out in 2D spectral coordinates using the steepest-descent path. This property allows for a very fast update of the ground contribution matrix, while looping through soil parameters. The proposed method has been validated against the exact MoM solution in the case of a PEC ground. The FGCM method has also been validated against the commercial software IE3D in the case of a lossy multi-layered ground, and SEMCAD (FDTD method) in the case of PEC and lossy media. Considering a 3D wideband antenna, it has been shown that the FGCM method is 22 times faster than the MoM brute-force solution (1.5 seconds compared to 33.5 seconds) when changing the ground permittivity, conductivity, permeability, number of layers, layer thickness, and/or antenna height. Accurate experimental validation has been provided for antennas at a range of distances above both PEC and lossy dielectric grounds. We hope this novel technique will be of significant use to those interested in characterizing grounds.

Finally, we target to analyze large planar antenna arrays placed above multi-layered substrate, taking the benefit of the FGCM method and accelerating the MBFs interactions using the C-FFT method. First, we validate the MBF and the FGCM methods against the MoM brute-force solution. SDP contour deformation is again used, and an excellent accuracy with an error level well below -70 dB over the frequency band of interest is obtained. Then, C-FFT method is used to accelerate the MBFs interactions for 3×3 regular array. The C-FFT expansion until 5th order has been used. However, we noticed that the number of FFTs would increase a lot, if we continue working with the SDP contour. Therefore, further work will focus on lowering the contour and benchmarking the required number of FFT terms.

7.2 Future prospects

One of the goals of this work is to design a wideband antenna array for imaging applications. The WoT has been successfully used to localize and image metallic tubes. Also, a dielectric cylinder of relative permittivity $\epsilon_r = 4$ was successfully imaged. Further steps will be to image animal tissues or human phantoms, such as breast phantom for breast cancer detection application.

In the presence of a target in the area of radiation exposure, multiple-scattering paths have to be taken in consideration for accurate image reconstructions. This problem has been explained in Chapter 5, where the time domain response of the reference target is exploited. A calibration algorithm is needed to account for the back-scattering radiation from the target on the WoT, and it will help to provide more accurate simulation results. The WoT allowed us to distinguish between two metallic cylinders with different diameters. Developing an algorithm allowing to distinguish between canonical targets will be an advancement on the way toward arbitrary target imaging. Also, future research is proposed regarding the effects of scattering by the antennas themselves inside the area of WoT radiation exposure. The experience acquired in the field of 3-D metallic antennas (design, fabrication, measurement, antenna simulation in the presence of a target...ect.) could be employed in any area of industrial quality control application.

The other achievement regarding the efficient inclusion of the effect of the ground on the antennas could be transformed into a commercial software, since this feature does not exist in known antenna solvers. Future work will consist of either creating a project to develop a commercial software to simulate antennas with the ground or contacting the R&D departments of existing software companies to add this feature to their software.

In lossy media with high relative permittivity and conductivity values, the skin depth is very small yielding high scattered planwaves. It is recommended to keep the distance between the radiator and the medium at a twentieth of the wavelength. Smaller distances a priori require a too large number of inhomogeneous plane waves; i.e., a too large number of spectral samples. Other field decompositions may prove more appropriate here. Future work will focus on analyzing this special case.

Finally, regarding the way to simulate large planar antenna arrays, we used the SDP contour, which considers as a high contour height, to account for the contribution of the substrate on antennas. The required order in the C-FFT development increases with the product between contour height and array size. So, to simulate large antenna arrays, it is recommended to use a low contour to avoid increasing the number of FFTs. Future work will consist of repeating the work for a low parabolic contour, for example, to simulate large planar antenna arrays.

List of Publications

A

Journal Papers

J. ***K. Alkhalifeh***, *G. Hislope, N. A. Ozdemir, C. Craeye*, "**Efficient MoM Simulation of 3-D Antennas in the vicinity of the Ground**", IEEE Trans. Antennas Propag. vol. 64, no. 12, pp. 5335-5344, Dec. 2016.

Conference Papers

1. ***K. Alkhalifeh***, *Shambhu Nath Jha, Sumit Karki, Christophe Craeye*, "**On the Use of Contour-FFT for the MBF-based Analysis of Arrays of Antennas Placed Vertically Above a Multi-layered Substrate**", Proc. 9th Eur. Conf. Antennas Propag. (EUCAP), pp. 1-5, Apr. 2015.

2. ***K. Alkhalifeh***, *N. Ozdemir, C. Craeye*, "**Efficient simulation of coupled ground antennas**", Proc. 9th Eur. Conf. Antennas Propag. (EUCAP), pp. 1-4, Apr. 2015.

3. ***K. Alkhalifeh***, *C. Craeye, S. Lambot*, "**Design of a 3D UWB Linear Array of Vivaldi antennas devoted to Water Leaks Detection**", 15th International Conf. on Ground Penetrating Radar, Brussels, July 2014, pp. 783-786.

4. ***K. Alkhalifeh***, *A. Cosse, C. Craeye , B. Macq*, "**Microwave Imaging From Wheel-of-Time Data**", Proc. 8th Eur. Conf. Antennas Propag. (EUCAP), pp. 609-613, Apr. 2014.

5. *S. Hubert*, ***K. Alkhalifeh***, *N. ozdemir and C. Craeye*, "**Compact Mathematical Description of Sectorially Symmetrical Arrays**", International Conference on Electromagnetics in Advanced Applications (ICEAA), Torino, 2013, pp. 1178-1181.

6. ***K. Alkhalifeh***, *R. Sarkis and C. Craeye*, "**Wheel-of-Time array devoted to near-field imaging**", International Conf. on Electromagnetics in Advanced Applications (ICEAA), Torino, Sept. 2013, pp. 1164-1167.

7. ***K. Alkhalifeh***, *R. Sarkis and C. Craeye*, "**Design of a Novel 3D Circular Vivaldi Antennas Array for Ultra-Wideband Near-Field Radar Imaging**", Proc. 6th Eur. Conf. Antennas Propag. (EUCAP), pp. 898-901, Mar. 2012.

Bibliography

[1] S. K. Davis, H. Tandradinata, S. C. Hagness and B.D. Van Veen, "Ultrawideband Microwave Breast Cancer Detection: A Detection-Theoretic Approach Using the Generalized Likelihood Ratio Test," IEEE Trans. on Biomedical Engineering, vol. 52, no. 7, pp. 1237-1250, July 2005.

[2] S. Kidera and T. Kirimoto, "Fast and shadow region 3-dimensional imaging algorithm with range derivative of doubly scattered signals for UWB radars", IEEE Trans. Antennas Propag., vol. 60, no. 2, pp. 984-996, 2012.

[3] Ben Allen, M. Dohler, E. Okon, W. Q. Malik, A. K. Brown, D. J. Edwards, "Ultra-Wideband: Antennas and Propagation for Communications, Radar and Imaging", John Wiley&Sons Ltd, 2007.

[4] E. Anniballi, D. Petri, A. Yarovoy and O. Krasnov, "Active radar networks for terminal security airport", 15th International Radar Symposium (IRS), Gdansk, Poland, Aug. 2014, pp. 1-4.

[5] T. Sakamoto, T. Sato, P. Aubry and A. Yarovoy, "Fast imaging method for security systems using ultrawideband radar", IEEE Trans. on Aerospace and Electronic Systems, vol. 52, no. 2, pp. 658-670, Apr. 2016.

[6] X. Zhuge, A. G. Yarovoy, "Sparse multiple-input multiple-output arrays for high-resolution near-field ultra-wideband imaging", IET Microw. Antennas Propag., vol. 5, no. 1, pp. 1552-1562, Mar. 2011.

[7] A. Shlivinski ,E. Heyman ,and R. Kastner, "Antenna characterization in the time domain," IEEE Trans. Antennas Propag., vol. AP-45, no. 7, pp. 1140-1149, July 1997.

[8] P. J. Gibson, "The Vivaldi aerial", Proc. 9th European Microwave Conference, pp. 101-105, 1979.

[9] M. Dessouky, H. Sharshar, and Y. Albagory, “Efficient sidelobe reduction technique for small-sized concentric circular arrays,” Progress In Electromagnetics Research, PIER 65, 187-200, 2006.

[10] Bo Wei , Ambuj Varshney , Neal Patwari , Wen Hu , Thiemo Voigt , Chun Tung Chou, “dRTI: directional radio tomographic imaging,” Proceedings of the 14th International Conference on Information Processing in Sensor Networks, April 13-16, 2015, Seattle, Washington.

[11] H. Nakano, T. Unno, K. Nakayama, and J. Yamauchi, “FDTD analysis and measurement of aperture antennas based on the triplate transmission-line structure,” IEEE Trans. Antennas Propag., vol. 47, no. 6, pp. 986-992, June 1999.

[12] W. Yu and R. Mittra, *CFDTD: Conformal finite difference time domain Maxwell's equations solver, software and user's guide*. Artech House, 2003.

[13] A. Giannopoulos, “Modelling ground penetrating radar by GPRMax,” Construction and Building Materials, vol. 19, no. 10, pp. 755-762, 2005.

[14] S. S. Rao, *The finite Element Method in Engineering*. Butherworth Heinemann, 2010.

[15] C. Lu and B. Shanker, “Generalized Finite Element Mathod for vector electromagnetic problems,” IEEE Trans. Antennas Propag., vol. 55, no. 5, pp. 1369-1381, May 2007.

[16] R. F. Harrington, *Field Computation by Moment Methods.* Piscataway, NJ, USA: Wiley-IEEE Press, 1993.

[17] F. Capolino, D. Jackson, and D. Wilton, “Fundamental properties of the field at the interface between the air and a periodic artificial material excited by a line source,” IEEE Trans. Antennas Propag., vol. 27, no. 3, pp. 331-343, May 1979.

[18] S. Lambot and F. Andre, “Full-wave modeling of near-field radar data for planar layered media reconstruction,” IEEE Trans. on Geoscience and Remote Sensing, vol. 52, no. 5, pp. 2295-2303, May 2014.

[19] E. Slob, M. Sato, and G. Olhoeft, “Surface and borehole ground-penetrating-radar developments,” Geophysics, vol. 75, no. 5, pp. A103-A120, 2010.

[20] M. F. Pantoja, A. G. Yarovoy, A. R. Bretones, and S. G. Garcia, “Time domain analysis of thin-wire antennas over lossy ground using the reflection-coefficient approximation,” Radio Sci., vol. 44, no. 6, p. 14, 2009.

[21] A. Skrivervic and J. Mosig, “Analysis of printed array antennas,” IEEE Trans. Antennas Propag., vol. 45, no. 9, pp. 1411-1418, Sept. 1997.

[22] S. I. Al-Mously and M. M. Abousetta, “A Novel Multi-Wideband Antenna Using a 3-D Multi-Branch Monopole Structure for GSM-Family and Other Cellular Applications”, 8th International Conference on Telecommunication in Modern Satellite, Cable and Broadcasting Services, Serbia, 2007, pp. 577-580.

[23] H. L. Thal, “New Radiation Q Limits for Spherical Wire Anten- nas”, IEEE Trans. Antennas Propag., vol. 54, no. 10, pp. 2757-2763, Oct. 2006.

[24] J. J. Adams et al., “Conformal printing of electrically small antennas on three-dimensional surfaces”, Adv. Mater., vol. 23, no. 11, pp. 1335-1340, 2011.

[25] S. Mufti, A. Tennant and L. Seed, “3D electrically small dome antenna”, Loughborough Antennas Propag. Conference (LAPC), Loughborough, 2014, pp. 653-656.

[26] R. Haupt, “Adaptive Low Sidelobe Thinning,” International Conference on Electromagnetics in Advanced Applications (ICEAA), Torino, 2013, pp. 167-168.

[27] M. Klemm, J. Leendertz, D. Gibbins, I. Craddock, A. Preece, and R. Benjamin, “Microwave radar-based differential breast cancer imaging: imaging in homogeneous breast phantoms and low contrast scenarios,” IEEE Trans. Antennas Propag., vol. 58, pp. 2337-2344, July 2010.

[28] M.A. Al-Joumayly, S.M. Aguilar, N. Behdad, S.C. Hagness, “Dual-band miniaturized patch antennas for microwave breast imaging,” IEEE Trans. Antennas and Wireless Propaga. Letters, vol. 9, pp. 268-271, Mar. 2010.

[29] X. Zhuge, A. Yarovoy “Design of Low Profile Antipodal Vivaldi Antenna for Ultra-Wideband Near-Field Imaging,” 4th European Conference on Antennas and Propagation (EUCAP), pp. 12-16 Apr. 2010.

[30] Maaskant, R., Ivashina, M., Iupikov, O., Redkina, A., Kasturi, S., Shaubert, D.H. “Analysis of Large Microstrip-Fed Tapered Slot Antenna Arrays by Combining Electrodynamic and Quasi-Static Field Models,” IEEE Trans. Antennas Propag., vol. 59, no. 6, June 2011.

[31] Gijo Augustin and Tayeb A. Denidni, “Ultrawideband Antennas for Microwave Imaging Systems,” ISBN 13: 9781608077151, ARTECH HOUSE 2014.

[32] T.Wu and R. King, “The cylindrical antenna with nonreflective resistive loading,” IEEE Trans. Antennas Propagat., vol. AP-13, pp. 369-373, 1965.

[33] K. Kim, W. R. Scott Jr., “Design of a resistively loaded Vee dipole for ultrawide-band ground-penetrating radar applications,” IEEE Trans. Antennas Propagat., vol. 53, no. 8, pp. 2525-2532, Aug. 2005.

[34] S. Prasad and S. Mahapatra, “A new mic slot-line aerial,” IEEE Trans. Antennas and Propagat., vol. 31, no. 3, pp. 525-527, May 1983.

[35] B. Veidt, G. Hovey, T. Burgess, R. Smegal, R.Messing, A.Willis, A. Gray, and P. Dewdney, “Demonstration of a dual-polarized phased-array feed,” IEEE Trans. Antennas Propagat., vol. 59, no. 6, pp. 2047-2057, June 2011.

[36] R. Lee and R. Simons, “Effect of curvature on tapered slot antennas,” Society International Symposium in Antennas and Propagation, AP-S. Digest, vol. 1, pp. 188-191, Jul 1996.

[37] P.H. van der Merwe, J.W. Odendaal and J. Joubert, “An optimized quad-ridged horn antenna with pyramidal sidewalls,” Journal of Electromagnetic Waves and Applications, vol. 27, no. 17, pp. 2263-2273, 2013.

[38] C. M. Tan, P. Fletcher, M. A. Beach, A. R. Nix, M. Landmann, and R. S. Thomä, “On the application of circular arrays in direction finding part I: investigation into the estimation algorithms,” 1st Annual COST 273 Workshop, Finland, May 2002.

[39] E.A. Attardo, A. Borsic, G. Vecchi, P.M. Meaney, “Whole-System Electromagnetic Modeling for Microwave Tomopraphy,” IEEE Antennas Wireless Propag. Lett., vol. 11, 2012.

[40] M.S. Jessup, S. Simpson, "Circular Dual-Polarised Wideband Arrays for Direction Finding," Seminar on Wideband Multiband Antennas and Arrays for Defence or Civil Applications, Institution of Engineering and Technology, London, pp. 61-80, March 2008.

[41] GMSH: A Three-Dimensional Finite Element Mesh Generator With Built-In Pre- and Post-Processing Facilities. [Online]. Available: "http://gmsh.info/".The accessed date is 02. Oct. 2016.

[42] Constantine A. Balanis, *Antenna Theory, Analysis and Design* John Wiley and Sons, Inc, ch. 1.3.2, pp. 11-16.

[43] J. Shin, D.H. Schaubert, "A parameter study of stripline-fed Vivaldi notch-antenna arrays," IEEE Trans. Antennas Propag., vol. 47, no. 5, pp. 879-886, 1999.

[44] B.A. Munk and G.A. Burrell, "Plane-wave expansion for arrays of arbitrarily oriented piecewise linear elements and its application in determining the impedance of a single linear antenna in a lossy halfspace," IEEE Trans. Antennas Propag., vol. 27, no. 5, pp. 331-343, May 1979.

[45] C. Craeye and R. Sarkis, "Finite array analysis through combination of macro basis functions and array scanning methods," Journal of the Applied Computational Electromagnetics Society, vol. 23, no. 3, pp. 256-261, Sept. 2008.

[46] C. P. Matthews and M. D. Zoltowski, "Eigenstructure techniques for 2-D angle estimation with uniform circular arrays," IEEE Trans. on Signal Processing 42, pp. 2395-2407, 1994.

[47] D. C. Ross, J. L. Volakis, H. T. Anastassiu, "Three-dimensional edge-based finite-element analysis for discrete bodies of revolution," IEEE Trans. Antennas Propagat., vol. 45, pp. 1160-1165, July 1997.

[48] R. Sarkis, and C. Craeye, "Circular array of wideband 3D Vivaldi antennas," Electromagnetic Theory (EMTS), 2010 URSI International Symposium on, Aug. 2010, pp. 792-794.

[49] T. Dworak, M. Berglund, C. Laaser , P. Strosser, J. Roussard, B. Grandmougin, M. Kossida, I. Kyriazopoulou, J. Berbel, S. Kolberg, J. A. Rodríguez-Díaz and P. Montesinos, "EU Water saving potential (Part 1-Report)", ENV.D.2/ETU/2007/0001r, 19. July 2007.

[50] A. Cataldo, G. Cannazza, E. De Benedetto, N. Giaquinto, "Performance evaluation of a TDR-based system for detection of leaks in buried pipes", IEEE International Instrumentation and Measurement Technology Conference Proceedings, Graz, May 2012, pp. 792-795.

[51] F. Soldovieri, L. Crocco, A. Brancaccio, R. Solimene and R. Persico, "Applications of ground penetrating radar and microwave tomography in water monitoring and management," International Water Technology Journal, IWTJ, vol. I, no. 01, pp. 73-82, June 2011.

[52] S. Demirci, E. Yigit and Caner Ozdemir, "Detection of Movement and Impedance Changes behind Surfaces Using Ground Penetrating Radar," PIERS Proceedings, vol. 7, no. 1, 2011.

[53] M. Nakhkash, and M. Mahmood-Zadeh, "Water leak detection using ground penetrating radar," 10th International Conference on GPR, pp. 525-528, 2004.

[54] G. Ruvio , D. Gaetano , M. J. Ammann , and P. McEvoy , "Antipodal Vivaldi antenna for water pipe sensor and telemetry," Int. J. Geophysics, vol. 2012, May 2012.

[55] E. Gazit,"Improved design of the Vivaldi antenna", IEE Proc. H - Microwaves, Antennas Propag., vol. 135, no. 2, pp 89-92, April 1988.

[56] A. P. Tran, S. Lambot, "Intrinsic modeling of antenna array in near-field conditions," 15th International Conference on GPR, pp. 519-524, Jun-Jul 2014.

[57] Ye. Maksimovitch, V. Mikhnev, P. Vainikainen, "Characterization of tapered-slot antenna design for subsurface radar applications," Proc. 3th Eur. Conf. Antennas Propag. (EUCAP), pp. 2811-2813, Apr. 2009.

[58] R. Sarkis, B. Veidt, C. Craeye, "Fast numerical method for focal plane array simulation of 3D Vivaldi antennas," Proc. Int. Conf. Electromagn. Adv. Appl., pp. 772-775, Sept. 2012.

[59] Computer Simulation Technology GmbH, www.cst.com.

[60] D. Gabor, "A new microscopic principle", Nature, vol. 161, no. 4098, pp. 777-778, May 1948.

[61] K.P. Gaikovich, P.K. Gaikovich, Ye. S. Maksimovitch, V.A. Badeev, “Subsurface near-field microwave holography”, IEEE Journal of Selected Topics in Applied Earth Observations and Remote Sensing, vol. 9, no. 01, pp. 74-82, 2016.

[62] M. Ravan, R. K. Amineh, N. K. Nikolova, “Near-Field Microwave Holographic Imaging: Target Localization and Resolution Study”, URSI Int. Symp. on Electromagnetic Theory, pp.396-399, Aug. 2010.

[63] K. Alkhalifeh, R. Sarkis and C. Craeye, “Design of a Novel 3D Circular Vivaldi Antennas Array for Ultra-Wideband Near-Field Radar Imaging”, Proc. 6th Eur. Conf. Antennas Propag. (EUCAP), pp. 898-901, Mar. 2012.

[64] S. Lambot, E. C. Slob, I. van den Bosch, B. Stockbroeckx, and M. Vanclooster, “Modeling of ground-penetrating Radar for accurate characterization of subsurface electric properties,” IEEE Transactions on Geoscience and Remote Sensing, vol. 42, no. 11, pp. 2555-2568, 2004.

[65] S. Lambot and F. André, “Full-wave modeling of near-field radar data for planar layered media reconstruction,” IEEE Transactions on Geoscience and Remote Sensing, vol. 52, no. 5, pp. 2295-2303, May 2014.

[66] M. Guardiola, S. Capdevila and L. Jofre, “Robust Differential Multifrequency Microwave Imaging for Breast Cancer Detection,” Proc. 7th Eur. Conf. Antennas Propag. (EUCAP), pp. 622-623, Apr. 2013.

[67] X. Zeng, X. Fhager, and M. Persson, “Accuracy Evaluation of Ultrawideband Time Domain Systems for Microwave Imaging,” IEEE Trans. Antennas Propag., vol. 59, no. 11, pp. 4279-4285, 2011.

[68] M. Klemm, J.A. Leendertz, D. Gibbins, I.J. Craddock, A. Preece, and R. Benjamin, “Microwave radar-based breast cancer detection: Imaging in inhomogeneous breast phantoms”, IEEE Antennas Wireless Propag. Lett., vol.8, pp.1349-1352, 2009.

[69] X. Zhuge, A. G. Yarovoy, “Study on two-dimensional sparse MIMO UWB arrays for high resolution near-field imaging,” IEEE Trans. Antennas Propag., vol. 60, no. 09, pp. 4173-4182, Sept. 2012.

[70] L. Lo Monte, D. Erricolo, F. Soldovieri, and M. C. Wicks, “RF tomography for belowground imaging of extended areas and close-in sensing,” IEEE Geoscience and Remote Sensing Letters, vol. 7, no. 3, pp. 496-500, Jul 2010.

[71] G. Gennarelli, I. Catapano, F. Soldovieri, "RF/microwave imaging of sparse targets in urban areas," IEEE Antennas Wireless Propag. Lett., vol. 12, pp. 643-646, 2013.

[72] A. B. Suksmono, E. Bharata, A. A. Lestari, A. G. Yarovoy, L. P. Ligthart, "Compressive stepped-frequency continuous-wave ground-penetrating radar," IEEE Geosci. Remote Sens. Lett., vol. 7, no. 4, pp. 665-669, Oct. 2010.

[73] C. Craeye and D. González-Ovejero, "A review on array mutual coupling analysis," Radio. Sci., vol. 46, no. 02, pp. 1-25, Apr. 2011.

[74] H. T. Hui, "Decoupling methods for the mutual coupling effect in antenna arrays: a review," Recent Patents on Engineering, vol. 1, pp. 187-193, 2007.

[75] R. S. Fakhr, "Compact size and dual band semicircle shaped antenna for MIMO applications," Progress In Electromagnetics Research C, vol. 11, pp. 147-154, 2009.

[76] Li, H.J. Xiong, S. He, "A compact planar MIMO antenna system of four elements with similar radiation characteristics and isolation structure," IEEE Antennas and Wireless Propagation Letters, vol. 8, pp.1107-1110, 2009.

[77] J.Thaysen, K.B. Jakobsen, "Mutual coupling between identical planar inverted-F antennas," International Journal of Electronic and Communication, vol. 61, pp.540-545, 2007.

[78] C. Craeye and A.O. Boryssenko, "Direct radar positioning using strongly coupled Ultra-Wideband (UWB) antennas," Proc. of IEEE Symp. Antennas and Propag., San Diego, July, 2008.

[79] A. Bhattacharya, R. Sarkis, G. Hislop, S. Lambot, C. Craeye, "Modeling of an ultra-wideband antenna array devoted to near-field imaging," Proc. Loughborough Antennas Propag. Conf., Loughborough, UK, pp. 545-548, Nov. 2010.

[80] M.E. Bialkowski, "Ultra wideband microwave system with novel image reconstruction strategies for breast cancer detection," European Microwave Conference (EuMC), pp. 537-540, 2010.

[81] M.E. Bialkowski, Y. Wang ; A. Abu Bakar and Wee Chang Khor, "Novel image reconstruction algorithm for a UWB cylindrical microwave imaging system," 2010 IEEE MTT-S International Microwave Symposium Digest (MTT), pp. 477-480, 2010.

[82] E. Pettinelli, A. D. Matteo, S. E. Beaubien, E. Mattei, S. E. Lauro, A. Galli, and G. Vannaroni, "A controlled experiment to investigate the correlation between early-time signal attributes of ground-coupled radar and soil dielectric properties," J. Appl. Geophys., vol. 101, pp. 68-76, 2014.

[83] R. Solimene, A. DAlterio, G. Gennarelli, and F. Soldovieri, "Estimation of soil permittivity in presence of antenna-soil interactions," IEEE J. Sel. Topics Appl. Earth Observ. Remote Sens., vol. 7, no. 3, pp. 805-812, Mar. 2014.

[84] J. Minet, A. Wahyudi, P. Bogaert, M. Vanclooster, S. Lambot, "Mapping shallow soil moisture profiles at the field scale using full-waveform inversion of ground penetrating radar data," Geoderma, 161 (34), pp. 225-237, 2011.

[85] N. Diamanti, D. Redman, and A. Giannopoulos, "A study of GPR vertical crack responses in pavement using field data and numerical modelling," Proc. 13th Int. Conf. GPR, pp. 1-6, June 2010.

[86] Tosti, F., A. Benedetto, L. Bianchini Ciampoli, S. Lambot, C. Patriarca and E.C. Slob., "GPR analysis of clayey soil behaviour in unsaturated conditions for pavement engineering and geoscience applications," Near Surface Geophysics, vol. 14, no. 2, pp. 127-144, 2016.

[87] L. Crocco, F. Soldovieri, N. Cassidy, and G. Prisco, "Early-stage leaking pipes GPR monitoring via microwave tomographic inversion," J. Appl. Geophys., vol. 67, no. 4, pp. 270-277, Apr. 2009.

[88] A. Stampolidis, P. Soupios, F. Vallianatos, and G. Tsokas, "Detection of leaks in buried plastic water distribution pipes in urban places - a case study," Proc. of the 2nd Int. Workshop on Advanced Ground Penetrating Radar, Delft, The Netherlands, pp. 120-124, May 2003.

[89] S. Busch, J. van der Kruk, J. Bikowski, and H. Vereecke, "Quantitative conductivity and permittivity estimation using full-waveform inversion of on-ground GPR data," Geophys., vol. 77, no. 6, pp. H79-H91, Oct., 2012.

[90] G. Hislop, "Permittivity estimation using coupling of commercial ground penetrating radars," IEEE Trans. Geosci. Remote Sens., vol. 53, no. 8, pp. 4157-4164, Aug. 2015.

[91] D. Comite, A. Galli, S.E. Lauro, E. Mattei, E. Pettinelli, "Analysis of GPR early-time signal features for the evaluation of soil permittivity through numerical and experimental surveys," IEEE Trans. Geosc. Remote Sensing, vol. 9, no. 1, pp. 178-187, Jan. 2016.

[92] C. A. Balanis, "Antenna Theory: Analysis and Design," 3rd Edition, pp 205-207, USA: Wiley, May 2005.

[93] X. Millard and Q. H. Liu, "A fast volume integral equation solver for electromagnetic scattering from large inhomogeneous objects in planarly layered media," IEEE Trans. Antennas Propag., vol. 51, no. 9, pp. 2393-2401, Sept. 2003.

[94] J. Yeo and R. Mittra, "An algorithm for interpolating the frequency variations of method-of-moments matrices arising in the analysis of planar microstrip structures," IEEE Trans. Microwave Theory Tech., vol. 51, no. 3, pp. 1018-1025, Mar. 2003.

[95] J. K. Lee and J. A. Kong, "Dyadic Green's functions for layered anisotropic medium," Electromagn., vol. 3, no. 2, pp. 111-130, 1983.

[96] K. A. Michalski and D. Zheng, "Electromagnetic scattering and radiation by surface of arbitrary shape in layered media-Part I: Theory," IEEE Trans. Antennas Propag., vol. 38, no. 3, pp. 335-344, Mar. 1990.

[97] A. Dreher, "A new approach to dyadic Green's function in spectral domain," IEEE Trans. Antennas Propag., vol. 43, no. 11, pp. 1297-1302, Nov. 1995.

[98] W. C. Chew, J. S. Zhao, and T. J. Cui, "The layered medium Green's functionA new look," Microw. Opt. Technol. Lett., vol. 31, no. 4, pp. 252-255, May 2001.

[99] Y. Chen, S. Yang, S. He, and Z.-P. Nie, "Fast analysis of microstrip antennas over a frequency band using an accurate MoM matrix interpolation technique," Progress in Electromagn. Res., vol. 109, pp. 301-324, 2010.

[100] T. J. Cui and W. C. Chew, "Accurate Model of arbitrary wire antennas in free space, above or inside ground," IEEE Trans. Antennas Propag., vol. 48, no. 4, pp. 482-493, Apr. 2000.

[101] F. Keshmiri and C. Craeye, “Moment-method analysis of normal-to-body antennas using a Green’s function approach,” IEEE Trans. Antennas Propag., vol. 60, no. 9, pp. 4259-4270, Sept. 2012.

[102] G. Hislop, N. A. Ozdemir, C. Craeye, and D. Gonzalez-Ovejero, “MoM matrix generation based on frequency and material independent reactions (FMIR-MoM),” IEEE Trans. Antennas Propag., vol. 60, no. 12, pp. 5777-5786, Dec. 2012.

[103] K. A. Michalski, “On the efficient evaluation of integrals arising in the Sommerfeld halfspace problem,” Proc. Inst. Elect. Eng., vol. 132, pt. H, pp. 312-318, 1985.

[104] E. Martini, C. Craeye, N. Ozdemir and S. Maci, “Harmonics-based inhomogeneous plane-wave method (HIPW),” IEEE Trans. Antennas Propag., vol. 63, no. 5, pp. 2331-2336, May 2015.

[105] G. Hislop, S. Lambot, C. Craeye, D. Gonzalez-Ovejero and R. Sarkis, “Antenna calibration for near-field problems with the Method of Moments,” Proc. 5th Eur. Conf. Antennas Propaga. (EUCAP), pp. 2004-2008, Apr. 2011.

[106] G. Hislop, C. Craeye and D. Gonzalez-Ovejero, “Antenna Calibration for Near-Field Material Characterization,” IEEE Trans. Antennas Propagat., vol. 64, no. 4, pp. 1364-1372, Apr. 2016.

[107] K. Alkhalifeh, N. Ozdemir, C. Craeye, “Efficient simulation of coupled ground antennas,” Proc. 9th Eur. Conf. Antennas Propag. (EUCAP), pp. 1-4, Apr. 2015, .

[108] D. Pozar and D.H. Schaubert, “Microstrip antennas: the analysis and design of microstrip antennas and arrays,” New York: IEEE Press, 1995.

[109] K. Michalski and J. Mosig, “Multilayered media Green’s functions in integral equation formulations,” IEEE Trans. Antennas Propag., vol. 45, no. 3, pp. 508-519, Mar. 1997.

[110] B. L. Wei, T. J. Cui, Y. Xiao-Xing, Q. Zhi-Guo, and H. Wei, “Fast algorithms for large-scale periodic structures using subentire domain basis functions,” IEEE Trans. Antennas Propag., vol. 53, no. 3, pp. 1154-1162, Mar. 2005.

[111] N. Yuan, T.S. Yeo, X.C. Nie and L.W. Li, “A fast analysis of scattering and radiation of large microstrip antenna arrays,” IEEE Trans. Antennas Propag., vol. 51, no. 9, pp. 2218-2226, Sept. 2003.

[112] Weyl, H. “Ausbreitung elektromagnetische Wellen über einem ebenen Leiter.” Annalen der Physik 365: pp. 481-500, 1919.

[113] A. Fort, F. Keshmiri, G. Crusats, C. Craeye, and C. Oestges, “A body area propagation model derived from fundamental principles: Analytical analysis and comparison with measurements,” IEEE Trans. Antennas Propag., vol. 58, no. 2, pp. 503-514, Feb. 2010.

[114] S.N Jha, C. Craeye, “Contour-FFT based spectral domain MBF analysis of large printed antenna arrays,” IEEE Trans. Antennas Propag., vol. 62, no. 11, pp. 5752-5764, Nov. 2014.

[115] E. Martini, S. Karki, C. Craeye and S. Maci, “Error analysis of the harmonics-based plane wave method,” Proc. (ICEAA) conference, Torino, Italy, Sept. 2015, pp. 1493-1495.

[116] A. P. Tran, F. Andre, C. Craeye, and S. Lambot, “Near-field or far-field full-wave ground penetrating radar modeling as a function of the antenna height above a planar layered medium,” Progress in Electromagnetics Research B, vol. 141, pp. 415-430, 2013.

[117] S. Rao, D.Wilton, and A. Glisson, “Electromagnetic scattering by surfaces of arbitrary shape,” IEEE Trans. Antennas Propag., vol. 30, no. 3, pp. 409-418, May 1982.

[118] Zeland Software Inc., “IE3D Electromagnetic Simulation and Optimization Package,Version 9.35,” Zeland Software Inc., Fremont, CA, 2003.

[119] K. S. Yee, “Numerical solution of initial boundary value problems involving Maxwells equations in isotropic media,” IEEE Trans. Antennas Propag., vol. AP-14, 302-307, May 1966.

[120] Y. El Hajibi and A. El Hamichi, “Simulation and Numerical Modeling of a Rectangular Patch Antenna Using Finite Difference Time Domain (FDTD) Method,” Journal of Computer Science and Information Technology, vol. 2, no. 2, pp. 01-08, 2014.

[121] SEMCAD X: EM/T Simulation Platform. [Online]. Available: “https://www.speag.com/.” The acceded date is 02. Oct. 2016.

[122] K. Alkhalifeh, R. Sarkis and C. Craeye, "Wheel-of-Time array devoted to near-field imaging," Proc. (ICEAA) conference, Torino, Sept. 2013, pp. 1164-1167.

[123] G. Hislop, "Limitations of characterizing layered earth with off-ground GPR," Journal of Geophysics and Eng., vol. 13, no. 2, 30 Mar. 2016.

[124] P. Mahachoklertwattana, P. H. Pathak, and R. J. Burkholder, "A fast MoM approach for analyzing large arrays in a grounded multilayered medium," Radio Sci., vol. 43, no. 06, pp. 1-11, Dec. 2008.

[125] E. Suter and J. R. Mosig, "A subdomain multilevel appraoch for the efficient MoM analysis of large planar antennas," Microwave and optical Tech, Letters, vol. 26, no. 4, pp. 270-277, Aug. 2000.

[126] I. Stevanovic and J. R. Mosig, "Efficient evaluation of Macro-Basis-Function reaction terms in the subdomain multilevel approach," Microwave and optical Tech, Letters, vol. 42, no. 2, pp. 138-143, Jul. 2004.

[127] A. Freni, P. De Vita, P. Pirinoli, L. Matekovits, and G. Vechii, "Fast-Factorization acceleration of MoM compressive domain-decomposition," IEEE Trans. Antennas Propag., vol. 59, no. 12, pp. 4588-4599, Dec. 2011.

[128] P. Janpugdee, P. Pathak, P. Mahachoklertwattana, and R. Burkholder, "An accelerated DFT-MoM for the analysis of large finite periodic antenna arrays," IEEE Trans. Antennas Propag., vol. 54, no. 1, pp. 279-283, Jan. 2006.

[129] C. Craeye and Thierry Gilles, "Combination of multipole and macro basis function approaches for the analysis of finite arrays with dielectric elements," Proc. 1st Eur. Conf. Antennas Propag. (EUCAP), pp. 1-5, Nov. 2006.

[130] D. Gonzalez-Ovejero, F. Mesa, and C. Craeye, "Accelerated Macro Basis Functions analysis of finite printed antenna arrays through 2D and 3D multipole expansions," IEEE Trans. Antennas Propag., vol. 61, no. 2, pp. 707-717, Feb. 2013.

[131] C. Craeye, "A Fast impedance and pattern computation scheme for finite antenna arrays," IEEE Trans. Antennas Propag., vol. 54, no. 10, pp. 3030-3034, Oct. 2006.

[132] K. Michalski and J. Mosig, "Multilayered media Green's functions in integral equation formulations," IEEE Trans. Antennas Propag., vol. 45, no. 3, pp. 508-519, Mar. 1997.

[133] K. Alkhalifeh, N. Ozdemir, C. Craeye, "Efficient simulation of coupled ground antennas," Proc. 9th Eur. Conf. Antennas Propag. (EUCAP), pp. 1-4, 12-17 Apr. 2015.

[134] C. Craeye, T. Gilles, and X. Dardenne, "Efficient full-wave characterization of arrays of antennas embedded in finite dielectric volumes," Radio. Sci., vol. 44, no. 01, pp. 1-12, Feb. 2009.

[135] J. Yeo, V. Prakash, and R. Mittra, "Efficient analysis of a class of microstrip antennas using the Characteristic Basis Function Method CBFM," Micro. and Optical Tech. Lett., vol. 39, pp. 456-464, Jul. 2003.

[136] S. Hubert, S.N. Jha, C. Craeye, "Error Analysis for the Contour-FFT based Green's function," Electromagn. Advanced Appl. (ICEAA) Int. Conf., Sept. 2015, pp. 922-925.

[137] P. Haapaia, P. Vainikainen, and P. Eratuuli, "Dual frequency helical antennas for handsets," IEEE VTS 46th Vehicular Technology Conference Proceedings vol. 01, pp. 336-338, April 28-May 1, 1996, Atlanta, GA.

[138] D. Liu, "A multi-branch monopole antenna for dual-band antenna cellular applications," Proc. IEEE Int. Symp. Antennas Propaga. & URSI Nat. Radio Sci. Meeting, vol. 3, pp. 1578-1581, Orlando, 1999.

[139] J. D. Jang, S. W. Lee, and N. Kim, "Design of the Dual-band Planner Monopole Antenna for Coupled Rectangular-loop Structure and T-shape Rectangular Patch," PIERS Proceedings, Moscow, Russia, August 19-23, 2012.

[140] H. Chen, Y. Lin, C. Kuo, K. Huang, "A Compact Dual-Band Microstrip-Fed Monopole Antenna," Antennas and Propag. Society 2001 IEEE International Sym, vol. 2, pp. 124-127, 2001.

[141] Y. Chen, J. Cai, M. Liu, G. Zeng, Q. Feng, Z. Chen, "Research on double-probe double- and triple-tip effects during atomic force microscopy scanning", Scanning, vol. 26, no. 4, pp. 155-161, 2004.